UPC CTTC

Flow topology and small-scale dynamics in turbulent Rayleigh-Bénard convection

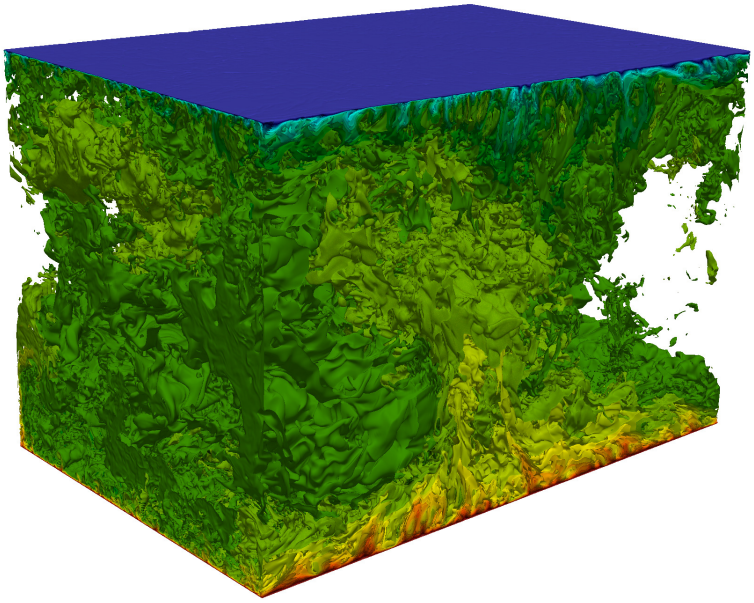

Centre Tecnològic de Transferència de Calor
Departament de Màquines i Motors Tèrmics
Universitat Politècnica de Catalunya

Firas Dabbagh

Doctoral Thesis

Flow topology and small-scale dynamics in turbulent Rayleigh-Bénard convection

Firas Dabbagh

TESI DOCTORAL

presentada al

Departament de Màquines i Motors Tèrmics
E.S.E.I.A.A.T.
Universitat Politècnica de Catalunya

per a l'obtenció del grau de

Doctor per la Universitat Politècnica de Catalunya

Terrassa, July 2017

Flow topology and small-scale dynamics in turbulent Rayleigh-Bénard convection

Firas Dabbagh

Directors de la Tesi

Dr. Francesc Xavier Trias Miquel

Dr. Andrey V. Gorobets

Dr. Assensi Oliva Llena

Tribunal Qualificador

This thesis is dedicated to

my parents, Aida and Fakhri,

my brothers Rami and Mohamed, and my sister Karam

Acknowledgements

I want to use these lines to thank all the people that has contributed, in either way, in the development of this thesis.

At the first place, Prof. Assensi Oliva, head of the *Heat and Mass Transfer Technological Center* (CTTC), for his inspiration and trust in me as a PhD candidate, and for helping me along these years in guiding my research in the topic I like most.

Dr. Xavi Trias, as the thesis director at first and as the brother and partner here in Spain, who supported and assisted me significantly in his purposeful guidance and fruitful ideas.

Dr. Andrey Gorobets, for resolving all queries of the DNS code and being the best humorist friend, and director to push this thesis straight ahead.

Prof. Habib Mahmoud, my supervisor at Tishreen University in Syria, for his useful advices and pursuing my thesis advance with the big support from there in Syria.

All lecturers and professors: Carlos D. Pérez-Segarra, Jesus Castro, Joaquim Rigola, Carles Oliet, Jorge Chiva, Ivette Rodríguez, who enriched my scientific knowledge and experience with the latest and up-to-date research methods.

Ramiro Alba, Octavi Pavon and Guillem Colomer for resolving the uncountable number of problems regarding the Linux system, the usage of the JFF, the utilization of writing and analyzing tools of Gnuplot, Tecplot, Paraview, LaTeX language,..etc.

All people and colleagues who shared me all the moments during my Ph.D and have evolved from mates to friends: Oussama Souaihi, Hamdi Kessentini, Mohamed Settati, Tayeb Feriani, Aleix Báez, Guillermo Oyarzún, Deniz Kızıldağ, Santiago Torras, Nicolás Ablanque, Hao Zhang, Xiaofei Hou and Pedro Galione. A special mention for Nacho González and Óscar Antepara who were more than brothers.

The Grant of *Tishreen University* for Ph.D students by the *Ministry of high education* in Syria, for the financial support although of the critical situation of war.

MareNostrum supercomputer at the Barcelona Supercomputing Center (BSC), for the technological support of computational resources needed for calculations.

Abstract

Without fluid turbulence, life might have rather different look. The atmosphere and oceans could nearly maintain a much larger temperature differences resulting in ultimate heating or cooling to the earth surface. The water and air flow could rather run much faster at rates of the speed of sound. Turbulence is a highly active nature of chaotic, random and three-dimensionality of swirling fluid. Its nonlinear convective property transports the momentum and energy in a helical mechanism leading eventually to an enriched fluid mixing and generating of small scale motions. These scales chiefly rule the hairpin vorticity dynamics, the turbulence non-Gaussianity, the strain/dissipation production and the cascade of kinetic energy mechanisms. Therefore, the key feature in turbulence is around disclosing the small scale motions. Studying the fine-scale dynamics gives us fundamental perspectives of flow topology and thus, improves our knowledge of turbulence physics. The turbulence dynamo becomes more complex when the active thermal gradient constitutes into the pure generator of turbulence. This particularly happens in the so-called buoyancy-driven Rayleigh-Bénard convection (RBC), when an infinite/bounded lying fluid is heated from below and cooled from above in the field of gravity. The main goal of this thesis is investigating the flow topology and small-scale dynamics in turbulent RBC, in order to better understanding its thermal turbulence mechanism and improve/validate the turbulence modeling for the foreseeable CFD[†] future.

To do so, a complete three-dimensional direct numerical simulation (DNS) of turbulent RBC in a rectangular air-filled cavity of aspect ratio $\Gamma = 1$ and π spanwise open-ended distance, has been presented at Rayleigh numbers $Ra = \{10^8, 10^{10}\}$, in chapter 1. The chapter highlights only the new features relevant to the DNS studies without repeating similar observations and facts extensively outlined in literature [F. Chillà & J. Schumacher, Euro. Physics J. E 35 (2012) 58]. A global kinetic energy conservation is inherited using a 4^{th}-order symmetry-preserving scheme [R. W. C. P. Verstappen & A. E. P. Veldman, J. Comput. Physics 187 (2003) 343] for the spatial discretization, and the flow dynamics is explored by analysis of kinetic and thermal energy power spectra, probability density function (PDF) of viscous and thermal dissipation rates, and identification of the wind in RBC.

In chapter 2, the DNS dataset is used to investigate several universal small-scale features observed in various turbulent flows and recaptured here in turbulent RBC through the bulk. For instance, the inclined "teardrop" shape of joint PDF velocity gradient tensor invariants (Q_G, R_G), the preferential alignment of vorticity $\boldsymbol{\omega}$

[†]Computational Fluid Dynamics

with $\boldsymbol{\lambda}_2$ the intermediate eigenstrain vector, the asymmetric $\boldsymbol{\omega}$ alignment with the vortex-stretching vector, and the spiralling degenerated behaviour of the average rates invariants $(\langle DQ_{\mathsf{G}}/Dt\rangle, \langle DR_{\mathsf{G}}/Dt\rangle)$ in $(Q_{\mathsf{G}}, R_{\mathsf{G}})$ space. This last has indicated the typical varying of topology surrounding a fluid particle, from unstable focus/stretching, unstable node saddle/saddle, stable node saddle/saddle to stable focus/compressing structures. It is found that a self-amplification of viscous straining $-Q_{\mathsf{S}}$ results at $Ra = 10^{10}$, helps in contracting the vorticity worms and enhances slightly the linear contributions of the vortex stretching mechanism. On the other hand, the evolution of relevant small-scale thermals has been addressed by investigating the average rate of invariants pertained to the traceless part of velocity-times-temperature gradient tensor, *i.e.* $(\langle DQ_{\tilde{\mathsf{G}}_\theta}/Dt\rangle, \langle DR_{\tilde{\mathsf{G}}_\theta}/Dt\rangle)$ in $(Q_{\tilde{\mathsf{G}}_\theta}, R_{\tilde{\mathsf{G}}_\theta})$ space. The new invariants are shown to follow correctly the evolution and lifetime of thermal plumes in RBC and hence disclose the deep interactions of bouyant production and viscous disspation.

In chapter 3, the DNS dataset is employed to understand the underlying physics of the subgrid-scale (SGS) motions in turbulent RBC in the spirit of Large-eddy simulation (LES) turbulence modeling. Firstly, the data is used to assess the performance of well-known LES eddy-viscosity models such as, WALE, QR and the recent S3PQR-models proposed by Trias *et al.*[PoF, 27, 065103 (2015)]. The outcomes have implied a limitation and incapability of theses models to reproduce well the SGS heat flux and the further dominant rotational enstrophy pertaining to the buoyant production. On the other hand, the key ingredients of eddy-viscosity, ν_t, eddy-diffusivity, κ_t and turbulent Prandtl number, Pr_t, are calculated *a priori* and investigated in a topological point-of-view. As a result, it has been suggested the restricted application of turbulent diffusion paradigm and the hypothesis of a constant Pr_t only in the large-scale strain-dominated areas in the bulk. More arguments have been attained through *a priori* investigation of the alignment trends imposed by existing parameterizations for the SGS heat flux. It is shown that the models based linearly on the resolved thermal gradient are invalid in RBC, and the tensorial-diffusivity approach is necessary. Finally, a new tensorial approach of modeling the SGS of thermal turbulence is sought that opens new research trends in the future.

The thesis is a collection of two international journal papers (chapters 2 and 3), either published or submitted. Therefore, all chapters are self-contained, which makes a certain degree of redundancy inevitable. Also, the meaning of symbols may differ per chapter. To my best perception, only the symbols α, β and γ differ between chapters 1 and 3. In chapter 1, α represents the thermal expansion coefficient while β and γ represent the scaling power laws of Nusselt Nu and Reynolds Re numbers in function of Ra, respectively. However in chapter 3, (α, β, γ) are the resultant angles in the space of the so-called mixed model span.

Contents

List of Figures

List of Tables

1

Direct numerical simulation of turbulent Rayleigh-Bénard convection

Main contents of this chapter have been published in:

F. Dabbagh, F. X. Trias A. Gorobets and A. Oliva, Spectrally-consistent regularization of turbulent Rayleigh-Bénard convection, 6^{th} *European Conference on Computational Fluid Dynamics*, 7144-7155, 2014.

Abstract. A set of completed three-dimensional direct numerical simulation (DNS) of turbulent Rayleigh-Bénard convection (RBC) in a rectangular air-filled cavity of aspect ratio $\Gamma = 1$ and π spanwise open-ended distance, are presented. Two Rayleigh numbers, $Ra = \{10^8, 10^{10}\}$, are outlined and an appropriate selection of the DNS grids size that refines analytical relations of the mean dissipative scales, is used. An overview of the numerical algorithms and discretization schemes used is given where a 4^{th}-order symmetry-preserving scheme, which ensures a global kinetic energy conservation, is employed. The principal flow dynamics is explored within analysis of kinetic and thermal energy power spectra, probability density function (PDF) of viscous and thermal dissipation rates, thermal/kinetic correlation coefficient and identification of the wind in RBC. The main results manifest on that the kinetic and thermal energy dissipation

rates are tightly correlated and fluctuated at the pattern evolution of thermal plumes, both in the bulk and boundary layers (BLs). The wind is identified as two helical coherent rolls that imply a falling cold flow at the middle and a rising hot one at the open-ends, while the fluctuated heat flux is sidewalls dominated.

1.1 Introduction

A fruitful knowledge that unravels the dynamics of Rayleigh-Bénard convection (RBC), have been accomplished in the last years. This phenomenon identified as a buoyancy-driven convection in a fluid layer heated from below and cooled from above [1], has engrossed many researchers in its complex momentum/heat transport mechanism. Despite its simple setup, it is a useful tool to understand many flows occurring in environment and technology. It is an idealised description of the flow in the outer layer of the sun, the coherent structures in the earth 's atmosphere and oceans, a main ingredient for the dynamo model in the earth 's core and plate tectonics via mantle convection, for the thermal comfort in aircraft cabins, the passive energy storage, for the cooling mechanism of electronic components and even everyday life, when cooking. Understanding this fundamental problem is, thus, not only utterly important for geo- and astrophysics, but also in industry (see Figure 1.1).

It is useful to give a brief description about the historical mechanism of the problem. I.e. under a continued conditions of large enough vertical temperature gradient applied in a horizontal fluid layer, an arbitrary fluctuation takes place and a small parcel of the hotter fluid than the neighboring fluid, experiencing a buoyancy force in a gravitational field begins to rise. The parcel rises when buoyancy force overcomes the viscous drag and thermal diffusion, and hotter fluid ascends from the underneath to fill the void left by the rising part inducing an amplification of temperature fluctuation. By drawing up more fluid from the hot region, higher thermal fluctuations occur and formulate a rising plume that becomes stronger with time. The competition between destabilizing effect of the buoyancy force and stabilizing effect of the viscous force leads to an instability in the flow. In this frame, any initial variation of temperature conditions or any trivial change of system aspect such as surface roughness, yields to an essential difference in the developed system. Bénard [2], was the first observer to the phenomenon in his experiments, where he found out that above a critical temperature gradient, the convection sets in, and a regular pattern of hexagons forms, when looking on the fluid layer from above. Rayleigh [3] laid the foundations of the problem by identifying the ratio of buoyancy force to viscous and thermal dissipation as the crucial control parameter for the onset of thermal instability. This quantity was named afterwards by Rayleigh number Ra, and the phenomenon by Rayleigh-Bénard convection, in honour of both scientists. By augmenting the strength of thermal forcing, spoke patterns evolve at around $Ra = 10^4$. These spokes tends to be stable for lower Ra and appear chaotically when Ra passes 10^5. Further increase of Ra tears off these spokes to form more independent large-scale flow structures which are the plumes. Thermal plumes are defined as fragments of the boundary layer that detach permanently and move into the bulk. Their stems have relatively high amplitude contributions of local heat flux, vertical velocity field and thermal

dissipation rate.

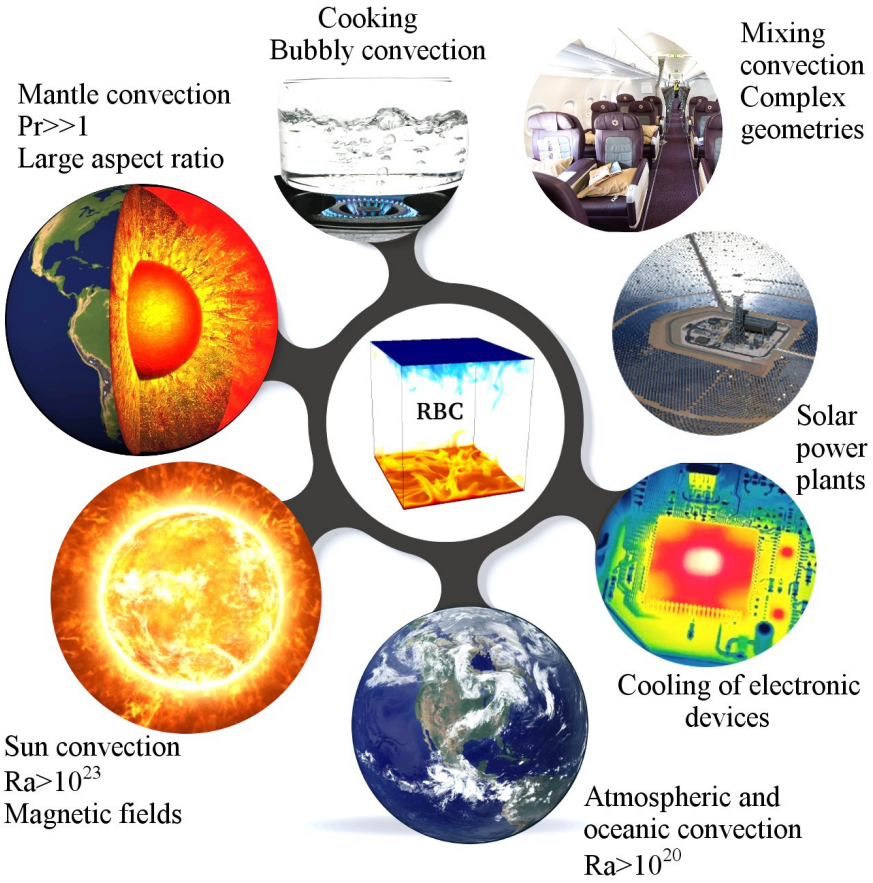

Figure 1.1: Diagram to visualise few examples, said to be describable by Rayleigh-Bénard convection.

- Earth 's atmosphere [http://geografijazasvakoga.weebly.com/]
- Sun [https://www.emaze.com/@AWOZCOIW/Plasma-Research]
- Earth 's core [http://www.sciencemag.org/news/2010/08/earths-moving-melting-core]
- Solar power plant [http://www.elakiri.com/forum/showthread.php?t=1601718]
- Cooking [https://www.shutterstock.com/search/boiling+water]
- Aircraft cabins [https://forum.lowyat.net/topic/4263919/all]
- Convection in electronic device [https://www.x20.org/scientific-analysis-flir-thermal-infrared-imaging-cameras/]

Classically, RBC has been studied with either infinite lateral extension or confined within simple geometries, like rectangular or cylindrical samples with different diameter-to-height (or width-to-height) aspect ratios (Γ). The parameters range in terms of the Rayleigh (Ra) and Prandtl (Pr) numbers, limited to, $Ra \leq 10^{17}$ and $Pr \approx \mathcal{O}(10)$ (Recent reviews, *e.g.*, Ahlers *et al.* [4]; Chillà & Schumacher [5]). The Rayleigh number is the ratio of buoyancy to dissipation, hence, being a measure for the thermal forcing and the grade of turbulence. The Prandtl number is the ratio of the viscous to the thermal time scale and is characteristic for every fluid. Indeed, extensive experimental, numerical and theoretical studies [5] are given in the scope of RBC. The experimental researches provided to some extent, valuable references for the numerical simulations and theories [6]. However, they have sustained uncertainties and clashes, particularly in heat transfer scaling law of Nusselt-Rayleigh relation, *i.e.*, $Nu \sim Ra^{\beta}$. For example, measurements in cylindrical cells of Castiang *et al.* [7] and Chavanne *et al.* [8], showed a scaling law $\beta = 0.287$ within a significant portion of $10^6 < Ra < 10^{17}$ (hard turbulence regime), however they started to contradict at $Ra > 10^{12}$ with multi-stability and non-Boussinesq effects. Chavanne *et al.* [8] and Roche *et al.* [9], observed a scaling law of $\beta = 0.38$ in the transition over $Ra = 7 \times 10^{11}$ that matches the Kraichnans asymptotic law with logarithmic corrections included [10] and the Grossmann-Lohse model for turbulent boundary layer (BL) [11]. However, Niemela & Sreenivasan [12], questioned that result by $\beta = 0.323$ for $Ra > 10^{12}$ and noticed a hysteresis scaling law in larger aspect ratio samples. In these Helium experiments, the Pr number was found to be a function to the increasing Ra. He *et al.* [13], using $SF6$ (Sulfur hexafluoride), showed a good agreement with Niemela & Sreenivasan [12] in cases up to $Ra = 10^{13}$, and a transition to the ultimate region ($Ra > 10^{14}$ [13]) with a scaling law $\beta = 0.38$ that consists very well with Chavanne *et al.* [8], was declared. In summary, the experimental results provided a complicated picture with high dependence upon the confined nature, the non-Oberbeck-Boussinesq effects and the uncontrollable real conditions such as, the finite conductivity and roughness of the walls.

In order to elude the qualm of experiments, direct numerical simulation (DNS) [14] is by far the most reliable tool. It allows a fully controlled picture that unravels in details the dynamical and statistical aspects of the turbulent problem. It can resolve many queries of turbulence physics by studying its characteristic structures, and enables investigations at the ultimate regime maintaining the Oberbeck-Boussinesq approximation (constant fluid properties including thermal expansion coefficient). Nowadays, DNS of turbulent RBC is covering a noteworthy portion of turbulence dynamics in a vast variety of parameters. For instance, in the frame of a rectangular convective cell, one can find the DNSs of Kaczorowski & Wagner [15] $(3.5 \times 10^5 \leq Ra \leq 3.5 \times 10^7, Pr = 0.7, \Gamma = 5)$ in a longitudinally open-ended cav-

ity, and within a confined cell in Kaczorowski & Xia [16] ($3 \times 10^5 \leq Ra \leq 3 \times 10^9$, $Pr = \{0.7, 4.38\}$, $\Gamma = 1$). They provided thereby, a useful analysis of thermal plumes and small-scale properties concerning to the Obukhof-Bolgiano scale [17]. Moreover, they showed that the geometrical confinement of the cell has an important influence on the flow properties [18]. On the other hand, the cylindrical samples were a very common choice in performing DNS of RBC, due to its easy comparison with the experimental studies. In that setting, many works have been executed to investigate the scaling behaviour and the robustness of grid resolution, such as Amati *et al.* [19] and Stevens *et al.* [20, 21]. They outlined a DNS analysis in a cell of aspect ratio $\Gamma = 1/2$ covering a wide range, ($2 \times 10^6 \leq Ra \leq 2 \times 10^{14}$, $Pr = 0.7$), where the finest DNS ever performed, belongs to Stevens *et al.* [21] at $Ra = 2 \times 10^{12}$. Other studies cared about heat transport mechanisms, sheet-like thermal plumes and thermal dissipation rate at large aspect ratio of cylindrical containers, as in Shishkina & Wagner [22–24], under the varieties ($\Gamma \to 10$, $Ra \to 10^7$, $Pr = 0.7$), and ($Ra \to 2 \times 10^{10}$, $\Gamma = 1, Pr = 5.4$). Deep scrutinies on the high-order statistics of thermal turbulence RBC were addressed by Emran & Schumacher [25, 26], which accessed one of the biggest fine DNS at ($Ra = 3 \times 10^{10}$, $Pr = 0.7$ and $\Gamma = 1$). The same authors have recently tackled with the evolution of LSC at very large cylindrical slender at $\Gamma = 50$ [27].

Few lines of study have handled with the deep coupling between the kinetic and thermal energy dissipation rates in turbulent RBC. The central understanding of the underlying physics of thermal turbulence and heat transport mechanism is strongly related to the interacted role of velocity/temperature gradient fields. Following rigorous analytical relations for the heat flux in RBC, the global averaging of kinetic and thermal dissipation rates are directly dependent on the Nu number [1]. In this case, DNS should resolve very well both dissipations not only on the average large scales but also on the fluctuated local scales. Upon the fluid properties and the strength of thermal-buoyancy forces, the fluctuated thermal/kinetic motion scales distribute differentially and vary in size between the BL and the rest of the flow in the bulk [20]. The dissipative quantities are coupled tightly with the small-scale flow intermittency, and they make the proper characterization of dynamics highly sensitive to the numerical methods used in the DNS. This topic has been firstly outlined by Scheel *et al.* [28], where a statistical analysis of viscous and thermal dissipation rates at different grids, ($10^6 \leq Ra \leq 10^9$, $\Gamma = 1$, $Pr = 0.7$), was presented. Nonetheless, the analysis outlined was limited to give an individual description on each dissipation within the different regions. In the present study, we focus on the crucial coupling between the kinetic and thermal dissipation rates in turbulent RBC. In this case, we handle a DNS study at bigger domain, than in [28], of an air ($Pr = 0.7$) filled rectangular cavity of aspect ratio unity ($\Gamma = 1$) and an open-ended (of periodic boundary conditions) spanwise ($= \pi$). These configurations reduce to significant extent the impact of the

confinement geometries which pockets the turbulent wind and modifies the dynamics in the bulk and BL. Two Rayleigh numbers $Ra = \{10^8, 10^{10}\}$ that indicate different structural turbulent regimes, are considered. The obtained Nu results were in very good agreement with heat transfer theories, such as [29]. Moreover, the viscous and thermal dissipations were found to be highly fluctuated and interacted at the patterns of thermal plumes, both in the BL and the bulk.

The present chapter is organized as follows. In the next section the governing equations and the numerical methods are described in details. Therein, the DNS resolution requirements towards the proper lowest amount of computational demands are outlined. In § 1.3, results of statistical analysis for viscous and thermal dissipations rates, are presented. We explore the main flow dynamics by studying the kinetic and thermal energy power spectra and the wind at this setting of turbulent RBC. Finally, relevant results are summarized and conclusions are given in § 1.4.

1.2 Governing equations and numerical method

1.2.1 Governing equations

We restrict ourselves to a rectangular geometry of aspect ratio unity–squared cross section–($\Gamma = W/H$) and longitudinal spanwise open-ended distance $L/H = \pi$ (see sketch in Figure 1.2). L, W and H correspond to the physical real dimensions of the cavity, identified as, the length, width and the height, respectively. The cavity is filled with a Newtonian fluid of constant thermophysical properties, as the kinematic viscosity ν and thermal diffusivity κ. The fluid is transparent to the radiation with a density variations and compressibility effects are neglected. The only exception is the density variation in the buoyancy forces where the so-called Oberbeck-Boussinesq (OB) approximation, is used. Following theses assumptions, and in case of negligible thermal radiation, the governing equations of continuity (mass conservation), Navier-Stokes (NS) (momentum conservation), and thermal energy (energy conservation), are given in non-dimensional form as

$$\nabla \cdot \boldsymbol{u} = \mathbf{0}\,, \tag{1.1}$$

$$\frac{\partial \boldsymbol{u}}{\partial t} + (\boldsymbol{u}\cdot\nabla)\boldsymbol{u} = -\nabla p + \sqrt{\frac{Pr}{Ra}}\nabla^2\boldsymbol{u} + \boldsymbol{f}\,, \tag{1.2}$$

$$\frac{\partial T}{\partial t} + (\boldsymbol{u}\cdot\nabla)T = \frac{1}{\sqrt{RaPr}}\nabla^2 T\,, \tag{1.3}$$

where $\boldsymbol{u} = (u, v, w)$ is the velocity vector in Cartesian coordinates $\boldsymbol{x} = (x, y, z)$, p is the pressure field, $\boldsymbol{f} = (0, 0, T)$ is the body force vector and T is the temperature. These

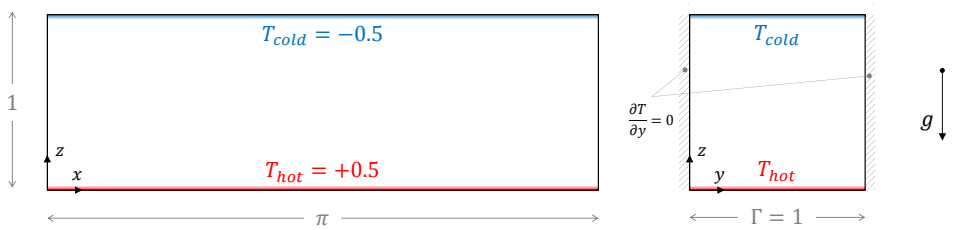

Figure 1.2: Schematic representation of the studied Rayleigh-Bénard convective cell.

equations formulate the mathematical model that describes the flow dynamics in RBC. All quantities therein (in Eqs. 1.1, 1.2 and 1.3) are written in dimensionless form using the height of the fluid layer H, the temperature difference between the upper and the lower surfaces $\Delta\Theta$ and the free-fall velocity $U_{ref} = (\alpha g \Delta\Theta H)^{1/2}$. Namely, U_{ref}, ρU_{ref}^2, $\Delta\Theta$ and H/U_{ref} are used as the characteristic scales for $\boldsymbol{u}$, p, T and the time t, respectively, where α is the volumetric thermal expansion coefficient and g stands for the gravitational acceleration. The cavity is subjected to horizontal bottom and top constant dimensionless temperatures, $T_{hot} = 0.5$ and $T_{cold} = -0.5$, respectively, while the vertical walls are thermally insulated ($\partial T/\partial y = 0$). No-slip boundary conditions for the fluid ($\boldsymbol{u} = \boldsymbol{0}$) are imposed at all the four solid walls, and periodic boundary conditions are applied for all quantities in the longitudinal x-direction. The characteristic parameters of the system are introduced within the numbers of Prandtl $Pr = \nu/\kappa$ (here $Pr = 0.7$) and Rayleigh $Ra = g\alpha\Delta\Theta H^3/(\nu\kappa)$, ($10^8$ and 10^{10}), and in responding to that physics, the average Nusselt number Nu is given by

$$Nu = \sqrt{RaPr}\langle wT\rangle_A - \frac{\partial\langle T\rangle_A}{\partial z}, \tag{1.4}$$

where the angular brackets operator $\langle\cdot\rangle$ indicates the temporal average (likewise it denotes the ensemble average in the statistical analysis), and the subscript symbol A refers to the average over (x-y) plane at position z.

1.2.2 Numerical method

Spatial discretization The governing equations (1.1, 1.2 and 1.3) are numerically discretized in space on a Cartesian staggered grid using a finite-volume 4^{th}-order symmetry-preserving scheme [30]. The main idea of these schemes is making the discretization in such a manner that the discrete difference operators mimic the crucial symmetry properties of the underlying differential operators. In this way, certain

fundamental properties such as the inviscid invariants-kinetic energy, enstrophy (in 2D) and helicity (in 3D), are exactly preserved [30]. Following an operator-based formulation, the discretized NS and continuity equations (Eq.1.1 and 1.2) are given by

$$\mathbf{M}\boldsymbol{u}_h = \mathbf{0}_h \tag{1.5}$$

$$\boldsymbol{\Omega}\frac{d\boldsymbol{u}_h}{dt} = -\mathbf{C}(\boldsymbol{u}_h)\boldsymbol{u}_h + \mathbf{D}\boldsymbol{u}_h + \boldsymbol{f}_h - \boldsymbol{\Omega}\mathbf{G}\boldsymbol{p}_h \tag{1.6}$$

where $\boldsymbol{u}_h$ is the discrete velocity vector and $\boldsymbol{\Omega}$ is a positive-definite diagonal matrix which contains the sizes of control volumes. $\mathbf{C}(\boldsymbol{u}_h)$ is the convective coefficient matrix which is approached as a skew-symmetric matrix contributing to the mass fluxes. $\mathbf{D}$ is the discrete diffusive operator defined as a symmetric negative-definite matrix. $\boldsymbol{f}_h$ is the discrete source vector and $\mathbf{M}$,$\mathbf{G}$ are the discrete divergence and gradient operators, respectively. In the same formulation the global kinetic energy equation can be written as

$$\frac{d}{dt}\|\boldsymbol{u}_h\|^2 = -\boldsymbol{u}_h^t(\mathbf{C}(\boldsymbol{u}_h) + \mathbf{C}^t(\boldsymbol{u}_h))\boldsymbol{u}_h + \boldsymbol{u}_h^t(\mathbf{D} + \mathbf{D}^t)\boldsymbol{u}_h + 2\boldsymbol{u}_h\boldsymbol{f}_h - \boldsymbol{u}_h^t\boldsymbol{\Omega}\mathbf{G}\boldsymbol{p}_h - \boldsymbol{p}_h^t\mathbf{G}^t\boldsymbol{\Omega}^t\boldsymbol{u}_h \tag{1.7}$$

The convective operator is skew-symmetric, that means,

$$\mathbf{C}(\boldsymbol{u}_h) = -\mathbf{C}^t(\boldsymbol{u}_h), \tag{1.8}$$

and the negative conjugate transpose of the discrete gradient operator is exactly equal to the divergence operator, *i.e.*,

$$-(\boldsymbol{\Omega}\mathbf{G})^t = \mathbf{M}. \tag{1.9}$$

This leads in consequence to canceling both the convective and pressure terms and the global kinetic energy equation is given as,

$$\frac{d}{dt}\|\boldsymbol{u}_h\|^2 = \boldsymbol{u}_h^t(\mathbf{D} + \mathbf{D}^t)\boldsymbol{u}_h + 2\boldsymbol{u}_h\boldsymbol{f}_h. \tag{1.10}$$

The diffusive term is negative and works as a dissipative factor to the kinetic energy, whereas the source term is positive and works as a generator of energy. By this way the kinetic energy is not systematically damped by discrete convective operator and does not need to be damped explicitly to ensure the stability of the method. Regarding the time evolution of the cell-centered temperature T_h, it is discretized in the same way. For more details about symmetry-preserving scheme the reader is referred to [30].

Time integration method In order to simplify the notation, the equations of the momentum (1.2) and energy (1.3), can be rewritten as

$$\frac{\partial \boldsymbol{u}}{\partial t} = R(\boldsymbol{u}, \boldsymbol{f}) - \nabla p, \quad \text{where} \quad R(\boldsymbol{u}, \boldsymbol{f}) = -(\boldsymbol{u} \cdot \nabla)\boldsymbol{u} + (Pr/Ra)^{0.5}\nabla^2 \boldsymbol{u} + \boldsymbol{f}, \tag{1.11}$$

$$\frac{\partial T}{\partial t} = R(\boldsymbol{u}, T), \quad \text{where} \quad R(\boldsymbol{u}, T) = -(\boldsymbol{u} \cdot \nabla)T + (PrRa)^{-0.5}\nabla^2 T. \tag{1.12}$$

For the temporal discretization, a central difference scheme is used for the time derivative terms, a fully explicit second-order one-leg scheme is used for $R(\boldsymbol{u}, \boldsymbol{f})$, $R(\boldsymbol{u}, T)$. A first-order backward Euler scheme is used for the pressure-gradient term. Incompressibility constraint is treated implicit. Thus, we obtain the semi-discretized governing equations as

$$\nabla \cdot \boldsymbol{u}^{n+1} = \boldsymbol{0} \tag{1.13}$$

$$\frac{(k+1/2)\boldsymbol{u}^{n+1} - 2k\boldsymbol{u}^{n} + (k-1/2)\boldsymbol{u}^{n-1}}{\Delta t} = (1+k)R(\boldsymbol{u}, \boldsymbol{f})^{n} - kR(\boldsymbol{u}, \boldsymbol{f})^{n-1} - \nabla p^{n+1} \tag{1.14}$$

$$\frac{(k+1/2)T^{n+1} - 2kT^{n} + (k-1/2)T^{n-1}}{\Delta t} = (1+k)R(\boldsymbol{u}, T)^{n} - kR(\boldsymbol{u}, T)^{n-1} \tag{1.15}$$

The parameter k is computed each time step (Δt) to adapt the linear stability domain of the time-integration scheme to the instantaneous flow conditions in order to use the maximum Δt possible. The main idea is bounding the eigenvalues of the dynamical system analytically and compute k and Δt upon that better fits the linear stability domain. For further details about the time-integration method the reader is referred to [31].
It is well-known that due to stability reasons explicit temporal schemes introduce severe restrictions on Δt, while implicit discretization would improve the overall stability. However, for the use of implicit methods in DNS of turbulent flows the computational costs are rather high compared to those of explicit methods. This is because of the underlying restrictions to Δt that are required to fully resolve all temporal scales in the NS equations. Therefore, only explicit methods are considered in the view of the lower costs.

To solve the velocity-pressure coupling we use a classical **Fractional step projection method** [32], in these method solutions of the unsteady Navier-Stokes equations are obtained by first time-advancing the velocity field $\boldsymbol{u}$ without regard for its solenoidality constraint (Eq. 1.13), then recovering the proper solenoidal velocity field, $\boldsymbol{u}^{n+1}$ after applicate the continuity constraint in the Poisson equation. This projection method is derived from the well-known Helmholtz-Hodge vector decomposition theorem [32], whereby the predictor velocity $\boldsymbol{u}^{p}$ can be uniquely decomposed into a

divergence-free vector $\boldsymbol{u}^{n+1}$, and the gradient of a scalar field $\nabla\tilde{p}$, as

$$\boldsymbol{u}^{p} = \boldsymbol{u}^{n+1} + \nabla\tilde{p}, \tag{1.16}$$

where the predictor velocity $\boldsymbol{u}^{p}$ is (from Eq. 1.14)

$$\boldsymbol{u}^{p} = \frac{2k\boldsymbol{u}^{n} - (k-1/2)\boldsymbol{u}^{n-1}}{k+1/2} + \frac{\Delta t}{k+1/2}((1+k)R(\boldsymbol{u},\boldsymbol{f})^{n} - kR(\boldsymbol{u},\boldsymbol{f})^{n-1}), \tag{1.17}$$

and the pseudo-pressure is $\tilde{p} = \Delta t/(k+1/2)p^{n+1}$. The time-advancing temperature is also given from Eq. 1.15 as,

$$T^{n+1} = \frac{2kT^{n} - (k-1/2)T^{n-1}}{k+1/2} + \frac{\Delta t}{k+1/2}((1+k)R(\boldsymbol{u},T)^{n} - kR(\boldsymbol{u},T)^{n-1}) \tag{1.18}$$

Taking the divergence of Eq. 1.16, yields to Poisson equation for $\tilde{p}$

$$\nabla\cdot\boldsymbol{u}^{p} = \nabla\cdot\boldsymbol{u}^{n+1} + \nabla\cdot(\nabla\tilde{p}) \Rightarrow \nabla^{2}\tilde{p} = \nabla\cdot\boldsymbol{u}^{p} \tag{1.19}$$

Once the solution is obtained, $\boldsymbol{u}^{n+1}$ results from the correction

$$\boldsymbol{u}^{n+1} = \boldsymbol{u}^{p} - \nabla\tilde{p}. \tag{1.20}$$

Poisson equation is solved at each time step using the Fourier-based solver [33]. Briefly, it is a scalable parallel solver that uses diagonalization by means of a FFT in the periodic direction to uncouple the original 3D system into a set of independent 2D systems. These 2D systems are solved using a preconditioned conjugate gradient method except for the first lowest-frequency systems which are problematic for an iterative solver. Hence, they are solved with a parallel direct Schur complement-based method. The accuracy of the solution is automatically tuned during simulation in order to provide the requested reduction of the divergence norm $|\mathbf{M}\boldsymbol{u}_{h}^{n+1}|/|\mathbf{M}\boldsymbol{u}_{h}^{p}| \leqslant 10^{-3}$ on each time step. Finally, the absolute value of the resulting divergence norm is attained to 10^{-10}. For more details about the numerical methods, algorithms and verification of the code, the reader is referred to the work of Trias *et al.* [34].

1.2.3 Resolution requirements and validation

In turbulent Rayleigh-Bénard convection, the dissipative fine scales are essentially controlled by the Prandtl number. The smallest scales follow the Kolmogorov length η_k that is directly related to the kinetic energy dissipation when $Pr \leq 1$, while when $Pr > 1$, the Batchelor scales η_B that relatively expose the (active) scalar concentration

(thermal gradients), become the governor (smaller) lengths. Both mean scales are defined as

$$\langle \eta_K \rangle = \left(\frac{Pr}{Ra} \right)^{3/8} \langle \epsilon \rangle^{-1/4} \quad \text{and} \quad \langle \eta_B \rangle = \frac{\langle \eta_K \rangle}{\sqrt{Pr}} = \frac{1}{Pr^{1/8} Ra^{3/8}} \langle \epsilon \rangle^{-1/4} \tag{1.21}$$

where ϵ is the kinetic energy dissipation rate that is determined by

$$\epsilon(\boldsymbol{x}, t) = \sqrt{\frac{Pr}{Ra}} (\nabla \boldsymbol{u} + \nabla \boldsymbol{u}^t)^2. \tag{1.22}$$

The second substantial feature that demonstrates high sensitivity to fine scales and thus to poor insufficient resolution, is the thermal dissipation rate. Its value indicates the magnitude of thermal gradient vector through the flow, and translated as following

$$\epsilon_T(\boldsymbol{x}, t) = \frac{1}{\sqrt{RaPr}} (\nabla T)^2. \tag{1.23}$$

The global averages of the two dissipations are analytically given in function of (Ra,Pr,Nu) following an exact balance of the turbulent kinetic energy and scalar variance equations [1]. They are consequently written as

$$\langle \epsilon \rangle_{V,t} = \frac{Nu - 1}{(RaPr)^{1/2}} \quad \text{and} \quad \langle \epsilon_T \rangle_{V,t} = \frac{Nu}{(RaPr)^{1/2}}, \tag{1.24}$$

(where $\langle \cdot \rangle_{V,t}$ denotes the ensemble volume-time average). Using the relations (1.21) and (1.24), Grötbach [35] estimated the minimum mean grid spacing $\eta_{Grö.}$ required to resolve the mean dissipation in RBC, where his criteria are given by

$$\eta_{Grö} \leq \pi \left(\frac{Pr^2}{(Nu - 1) Ra} \right)^{1/4} \quad \text{for} \quad Pr \leq 1 \tag{1.25}$$

$$\eta_{Grö} \leq \pi \left(\frac{1}{(Nu - 1) Ra} \right)^{1/4} \quad \text{for} \quad Pr > 1 \tag{1.26}$$

Under these criteria, we construct Cartesian grids with a uniform grid spacing in the periodic x-direction, while the wall-normal points are distributed following a hyperbolic-tangent function with an equal number of nodes $(N_y = N_z)$, given in z-direction (identical for y-direction) by

$$z_i = \frac{1}{2} \left(1 + \frac{\tanh\{\iota_z (2(i-1)/N_z - 1)\}}{\tanh \iota_z} \right), \qquad i = 1, \ldots, N_z + 1, \tag{1.27}$$

where ι_z is the concentration factor in the z-direction. Several refinement ratios of $\eta_{Grö}$ criterion are tested first for the low Ra number. By introducing Δz_{max} as the maximum grid spacing applied in the core where $\Delta z_{max} = \Delta y_{max} = \Delta x$, the refinement approaches are defined as $\Delta z_{max}/\eta_{Grö} \in [1.1 \rightarrow 0.7]$. The numerical tests upon *a posteriori* comparisons of Nu values computed following: its BL-based*, global averaged dissipation rates (Eq. 1.24) and the global heat flux, given as

$$Nu_V = 1 + (RaPr)^{1/2}\langle wT\rangle_{V,t}, \tag{1.28}$$

are presented in Table 1.1 (top). Moreover, an investigation has been performed in order to reduce the computational cost by maximizing the equidistant spacing in the periodic x-direction (instead of setting it to $\Delta x = \Delta z_{max}$), at the same Ra number. In résumé, the results led to a refinement ratio of $\Delta z_{max}/\eta_{Grö} = 0.9$, and a coarsening tolerance for the homogeneous cell spacing in the range $\Delta x/\Delta z_{max} \in [1.25 \rightarrow 1.5]$, without losing accuracy. These results have later been used to choose the proper estimated grid at $Ra = 10^{10}$ (see Table 1.1, bottom). On the other hand, the BLs are resolved with $N_{BL} = 9$ and 12 grid points for $Ra = 10^8$ and 10^{10}, respectively. This exceeds the resolution requirements proposed by Shishkina *et al.* [36] and given, for $Pr \approx 0.7$, by

$$N_{th.BL} \approx 0.35Ra^{0.15}, \qquad 10^6 \leq Ra \leq 10^{10}, \tag{1.29}$$

$$N_{v.BL} \approx 0.31Ra^{0.15}, \qquad 10^6 \leq Ra \leq 10^{10}, \tag{1.30}$$

where $N_{th.BL}$ and $N_{v,BL}$ are the minimum required number of nodes within the thermal and viscous BLs, respectively.

Data for statistical analysis is collected after at least 500 non-dimensional time units $[TU]$ in order to be sure that the statistically steady state is reached and the flow becomes out of the initial transient effects. Temporal integrations are then started and continue during a sufficiently long time, $\xi = 500[TU]$ and $200[TU]$, for the low and high Ra numbers, respectively. They guarantee a statistically stable turbulent heat transport unchanged due to the presence of large-scale circulations, which erratically reverse their directions over many large eddy turnover times [37–39]. In this case, the large eddy turnover lasts about $\tau_{eddy} \sim 7[TU]$ ($Ra = 10^8$) and $5[TU]$ ($Ra = 10^{10}$).

*The heat transport near the isothermal plates in the BL is basically by conduction and the Nusselt number correlation (*Eq.* 1.4) is given as, $Nu = -\frac{\partial\langle T\rangle_A}{\partial z}|_{z=0}$

Table 1.1: Results of refinement tests around Grötzbach criterion at $Ra = 10^8$ and $\Delta x/\Delta z_{max} = 1$ (top table). Summary of final simulation parameters with Nu results, where $\eta_{DNS} = (\Delta x \Delta y_{max} \Delta z_{max})^{1/3}$ (bottom table).

$\frac{\Delta z_{max}}{\eta_{Grö}}$	$N_x \times N_y \times N_z$	Nu	$\frac{Nu_V}{Nu}$	$\frac{\langle\epsilon\rangle_{V,t}(RaPr)^{1/2}+1}{Nu}$	$\frac{\langle\epsilon_T\rangle_{V,t}(RaPr)^{1/2}}{Nu}$
1.1	$256 \times 150 \times 150$	31.44	0.997	0.966	0.983
1.0	$288 \times 158 \times 158$	31.10	0.997	0.971	0.985
0.9	$320 \times 174 \times 174$	31.00	0.999	0.976	0.988
0.8	$342 \times 192 \times 192$	30.93	0.999	0.982	0.991
0.7	$400 \times 208 \times 208$	30.86	1.001	0.984	0.993

Ra	$\eta_{Grö}$	$\frac{\Delta z_{max}}{\eta_{Grö}}$	$\frac{\Delta x}{\Delta z_{max}}$	η_{DNS}	$\iota_z = \iota_y$	$N_x \times N_y \times N_z$	N_{BL}	$\Delta t[TU]$	$\xi[TU]$	$\xi_{st}[\tau_{eddy}]$	Nu
10^8	1.09×10^{-2}	0.70	1.0	7.70×10^{-3}	1.4	$400 \times 208 \times 208$	9	1.45×10^{-3}	500	40	30.9
10^{10}	2.46×10^{-3}	0.92	1.36	2.50×10^{-3}	1.6	$1024 \times 768 \times 768$	12	4.14×10^{-4}	200	10	128.1

It has been defined as $\tau_{eddy} = H/\boldsymbol{u}_{rms}$, where $\boldsymbol{u}_{rms}$ [†] the root mean square of the bulk velocity. The instantaneous characteristics used in the statistical calculations are collected typically over several large eddy turnover times, ξ_{st} (see Table 1.1, bottom), which sufficiently ensure the statistics convergence.

The spanwise length in the periodic x-direction was set to π that is sufficiently long to ensure the uncorrelation of turbulence fluctuations. This has been approved in the two-point correlation analysis of the spanwise velocity component, given by

$$R_{u,u} = \frac{\langle u'(x,y,z)u'(x+r,y,z)\rangle}{\langle u'^2\rangle}, \tag{1.31}$$

at two different locations, *i.e.*, $P_1(y_1 = 0.5, z_1 = 0.5)$ and $P_2(y_2 = 0.5, z_2 = 0.015)$, in the bulk and near the wall, as showed in Figure 1.3(b). It can be noted that the correlation values fall to zero at separations lower than one-half period and the periodic distance is adequate. The bulk region considered throughout the thesis is identified

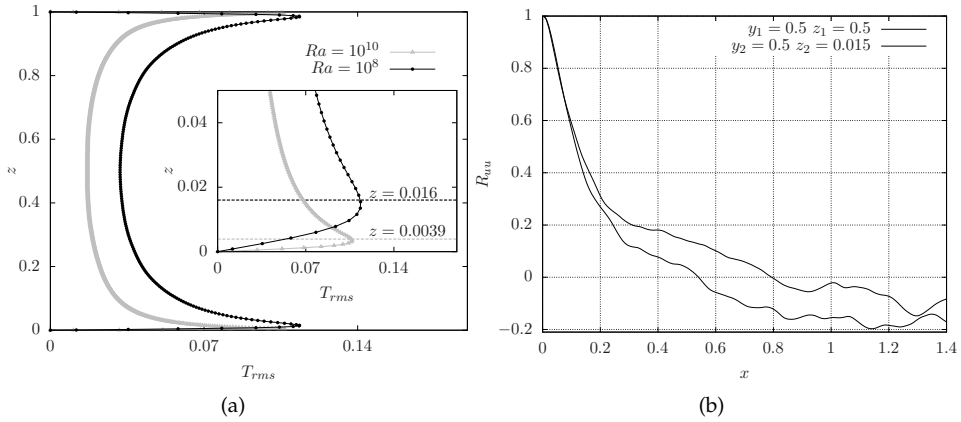

Figure 1.3: (a)*A posteriori* temporal-x averaged vertical profiles of T_{rms} extracted at the midwidth $y = 0.5$. (b) Represents the two-point correlation of the spanwise velocity u, taken at two monitoring locations (y-z) in the homogeneous x-direction at $Ra = 10^8$.

far enough from the solid boundaries and the near-wall influences. Consequently, a subvolume $V_{bulk} = \{\boldsymbol{x} = (x,y,z)|0.2 \leq y \leq 0.8; 0.2 \leq z \leq 0.8\}$, has been chosen as a representative domain of the bulk, which lays excessively out of the thermal BLs. In order to verify our selection, the vertical midwidth profiles of the x-average

[†] $\boldsymbol{u}_{rms} = \sqrt{\langle u'^2 + v'^2 + w'^2\rangle_{V,t}}$

root-mean-square temperatures are displayed in Figure 1.3(a) for both cases. The profiles show maximum values at the outlets of the thermal BLs to determine their thickness δ_T at the maximal thermal fluctuation [15]. The corresponding distances read, $z = 0.016$ in the case of $Ra = 10^8$ and $z = 0.0039$ for $Ra = 10^{10}$, which match very well with the theoretical prediction of Grossmann and Lohse [29] that reads $\delta_T = 0.5H/Nu$ ($\delta_T^{Ra=10^8} = 0.0162, \delta_T^{Ra=10^{10}} = 0.0039032$).

All simulation parameters and grid details are displayed in Table 1.1 (bottom) together with the Nu number, which propose a scaling power equal to $\beta \approx 0.309$. This value corresponds quite well to $\beta = 0.29$ proposed by Grossmann and Lohse theory [29] for $Pr \approx 1$ and Ra up to 10^{11}. Moreover, it also agrees with the DNS results of Scheel *et al.* [40] obtained at the same parameters ($Pr = 0.7$ and $Ra \in [3 \times 10^5 \rightarrow 10^{10}]$), and its suggested correlation $Nu = (0.15 \pm 0.01) \times Ra^{0.29 \pm 0.01}$.

1.3 Main results and discussion

1.3.1 Interactions between temperature and velocity fields

Snapshots of the isosurfaces temperature fields are displayed in Figure 1.4(a) at $Ra = 10^8$ and Figure 1.4(b) at $Ra = 10^{10}$. They illustrate the formation of the thermal plumes in a $(x\text{-}z)$ section, changing in regime from a fully developed turbulent flow to very hard turbulence [15]. The large-scale circulations become hardly identified in T field, and appear to be temporarily broken down and unstable, harder in the case of $Ra = 10^{10}$. The plumes emanate as fragments of the thermal BLs under an amplified coupling of kinetic/thermal turbulent fluctuations (see Figure 1.6 in advance). This amplified turbulence is mostly generated by a collusion of bulk dynamics impingement in the BL and strain rotation, to eventually excites the formation of the so-called sheet-like plumes or the roots in the BLs (see Figures 1.7(a) and 1.7(b)). At the intersection points of the roots, the plumes convolute and swirl away by buoyancy to arise into the bulk as the mushroom-like plumes (black and white fragments in Figure 1.4). Under the buoyant acceleration and thermal diffusion, these last expand away transforming their portable thermal energy into a kinetic one and feeding the momentum [15]. This operation therefore leads to a decorrelation of the thermal and kinetic behaviour between the bulk and the BL.

In order to show the previous mechanism we study the kinetic and thermal energy spectra in the homogeneous x-direction. Namely, we plot the one-dimensional energy spectra of T and the vertical velocity w along the periodic x-direction and averaged

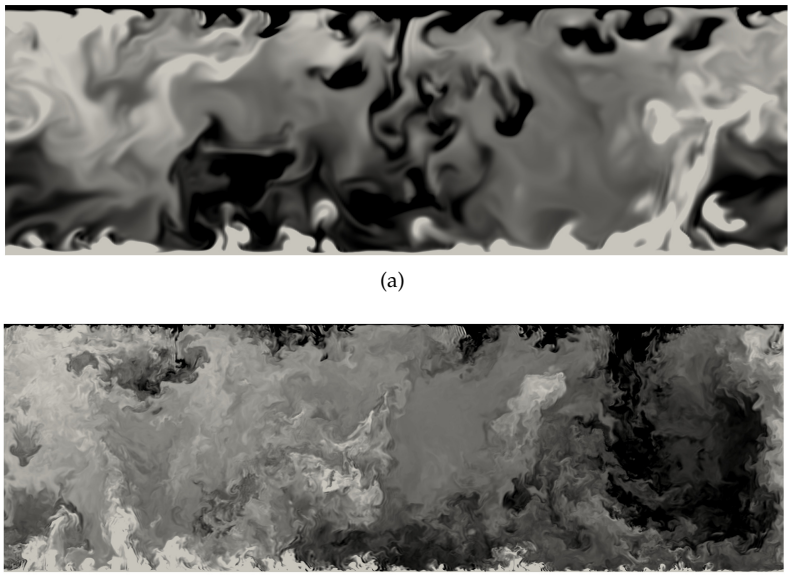

(a)

(b)

Figure 1.4: Snapshots of isosurfaces temperature fields in $(x\text{-}z)$ plane at $Ra = 10^8$ (a) and $Ra = 10^{10}$ (b).

in time, in Figure 1.5. It is defined as

$$E_{\phi\phi}(\mathrm{k}_x, y, z) = \langle \hat{\phi}_{\mathrm{k}_x}(y,z)\hat{\phi}^*_{\mathrm{k}_x}(y,z)\rangle, \tag{1.32}$$

where $(\cdot)^*$ is the complex conjugate for a variable ϕ and k_x is the wave number. The data is taken at two different regions of the domain, one within the thermal BL (insets) and the other in the core $(z = 0.5)$, midway between the lateral walls $(y = 0.5)$. Firstly, and in agreement with many studies, *e.g.*, Kaczorowski & Wagner [15], the velocity and temperature spectra in the centre of the cell correctly match the Kolmogorov $5/3$ and the Bolgiano $7/5$ exponents, respectively, across the inertial subrange. This implies that all the relevant turbulent scales are resolved by the grids used, and both the inertial subrange and the dissipation range are clearly identified for both turbulent cases in the main sets of Figures 1.5(a) and 1.5(b). The behaviour of the thermal and kinetic energy spectra in the bulk is opposite to that in the BL. The kinetic energy is placed higher than the thermal spectrum in the core, while it is lower in the BL, as displayed in the insets. On the other hand, the horizontal walls tends to damp the vertical kinetic energy in the near-wall vicinities, and makes the scaling exponents in the BL, different (smaller) than in the bulk. Analysis of the spectra at different

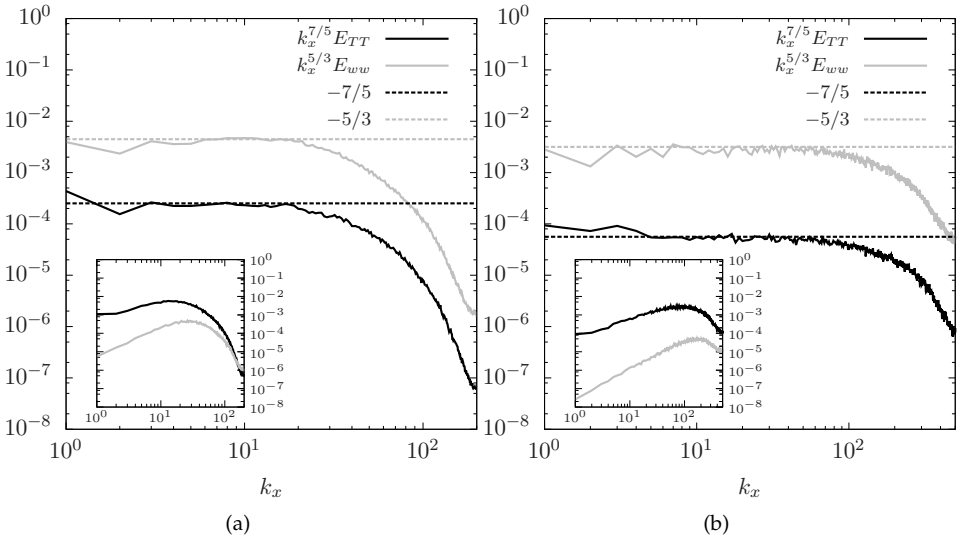

Figure 1.5: One-dimensional energy spectra in compensated formulae for the vertical velocity $k_x^{5/3}E_{ww}(k_x)$ and the temperature $k_x^{7/5}E_{TT}(k_x)$, extracted along the midwidth periodic x-direction in the core ($z = 0.5$) and inside the thermal BL (insets) at (a) $Ra = 10^8$ and (b) $Ra = 10^{10}$.

distances from the horizontal walls [15,41], shows that the level of the kinetic energy is continuously increasing towards the cell centre, while the temperature spectrum is slowly decreasing outside the BL towards the core. That mechanism is basically related to the thermal plumes evolution (its generation and shedding cycle). Taking a closer view, the thermal energy at $Ra = 10^8$ is higher than its counterpart at $Ra = 10^{10}$ for the lowest wave-number ($k_x^{7/5}E_{TT}(k_x) > 10^{-4}$). This supports the idea that less shedding (conversion into kinetic energy) on thermals takes place for $Ra = 10^8$. The plumes (mushroom-like) are developing farther into the bulk and survive longer in comparison with the case of $Ra = 10^{10}$ (see Figure 1.4).

A clearer picture of that dynamics can be taken from computing the correlation coefficient $C_{w'T'}$, and the skewness of temperature fluctuation $S_{T'}$, at various wall distances z , in Figure 1.6. They are defined as,

$$C_{w'T'} = \frac{\langle w'T' \rangle}{\sqrt{\langle w'^2 \rangle \langle T'^2 \rangle}}, \qquad S_{T'} = \frac{\langle T'^3 \rangle}{\langle T'^2 \rangle^{3/2}}, \tag{1.33}$$

and calculated at one (x, y) position ($x = 1.57, y = 0.5, z = 0 \rightarrow 1$) midways. The

resultant profiles are symmetrized over $z = 0.5$. Firstly, and as can be seen from Figure 1.6(a), the correlation between the turbulent fluctuations of the temperature and vertical velocity fields hold its maximum values near the walls inside the thermal BLs, for both turbulent cases. They manifest, in this behaviour, on the strong coupling between the thermal/kinetic turbulent fluctuations in the BL, as the origins of the thermal plumes. Both fields then, start to decorrelate in the bulk with decreasing values of $C_{w'T'}$ because of the mixing action and plumes scattering in the bulk. The correlation in the core at $Ra = 10^{10}$ becomes smaller than its counterpart at $Ra = 10^8$. This justifies the above-mentioned facts, that the mushroom-like plumes are less longer survived, smaller in size and high rapidly shedded at the harder turbulent case $Ra = 10^{10}$. On the other hand, the skewness measures the temporal deviation of T'

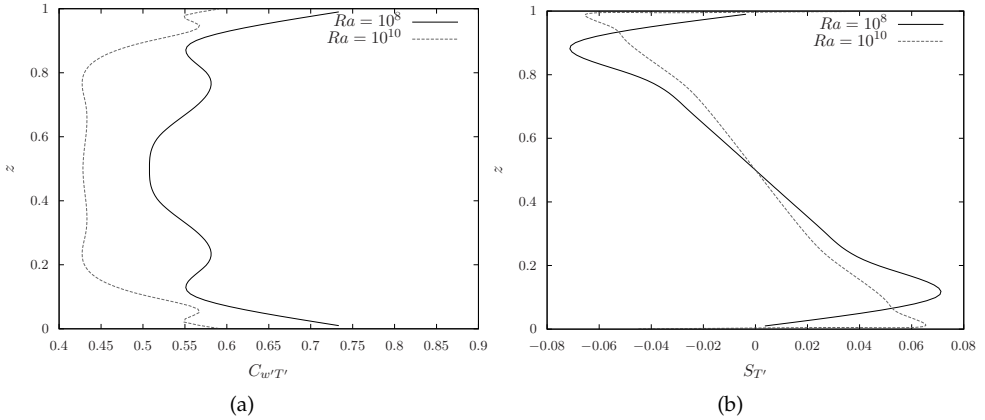

Figure 1.6: Correlation coefficient of turbulent fluctuations of the temperature T and vertical velocity w fields (a) and the skewness of temperature fluctuation (b), given in Eqs. 1.33, and computed at a single position $(x = 1.57, y = 0.5)$ and $(z = 0 \rightarrow 1)$.

from asymmetry, where zero values indicate that the distribution of T' is normal and symmetric, while negative or positive values indicate that the distribution is skewed right or left of its average. From Figure 1.6(b), the skewness shows high positive and negative values around δ_T to imply that rising and falling plumes are observed at the edge of the bottom and top thermal BLs. Simultaneously the colder and hotter pockets of temperature are generated in the vicinity of the thermal plumes that detach from the BLs, and the skewness approaches its maximal negative and positive values, which found to be higher (at further distance from the wall) at $Ra = 10^8$ in comparison with $Ra = 10^{10}$. This again certifies the bigger sizes of the mushroom-like plumes at $Ra = 10^8$, that develop longer in the bulk. Afterwards, and far from the walls, the skewness tends to vanish reading a null value at the center in the core, where the

plumes are well-mixed.

1.3.2 Thermal and kinetic energy dissipation rates

In order to disclose the underlying physics of the interacted kinetic/thermal turbulent fluctuations, the kinetic ϵ and thermal ϵ_T dissipation rates are studied in this context. Following its gradient-dependent definitions (Eqs. 1.22 and 1.23), both dissipations imply a high sensitivity to the small-scale dynamics and flow intermittency.

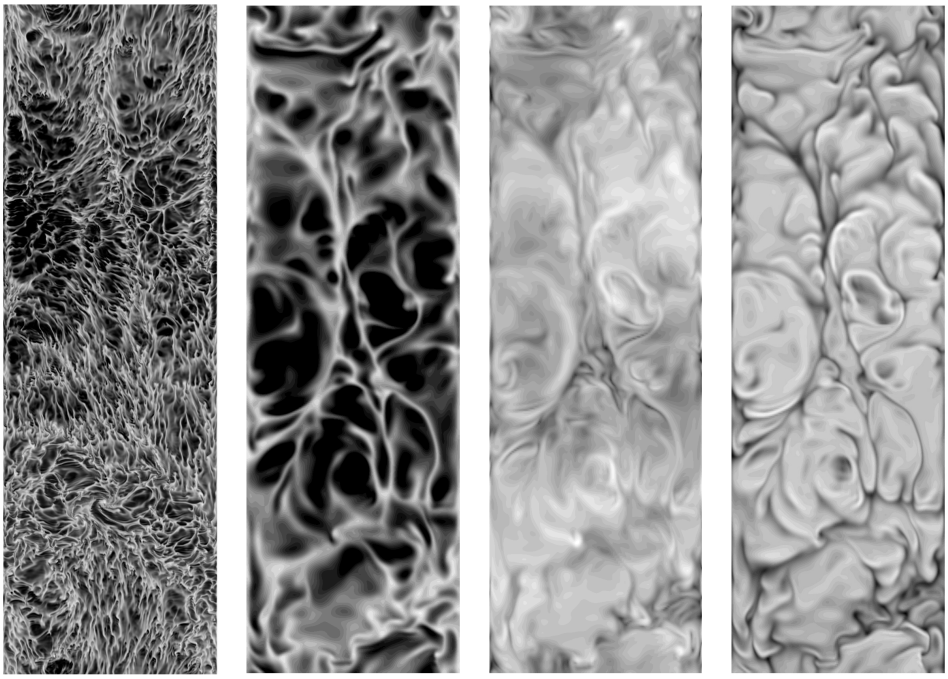

(a) (b) (c) (d)

Figure 1.7: Snapshots of temperature isosurfaces (sheet-like plumes) extracted along the horizontal plane $(x\text{-}y)$ at (a) $z_{Ra=10^{10}} = 0.002$ and (b) $z_{Ra=10^{8}} = 0.005$. (c) and (d) display the instantaneous ϵ and ϵ_T, respectively, in the same plane at $z_{Ra=10^{8}} = 0.005$. The data of dissipations is presented in logarithmic scale ranging, from black to white, as, $\log(\epsilon) \in [-4.6, -1.0]$ (c) and $\log(\epsilon_T) \in [-3.0, -0.53]$ (d).

They tightly interact with high amplitudes at the formation patterns of the sheet-like thermal plumes in the BLs, as shown in Figure 1.7. The data is given in logarithmic

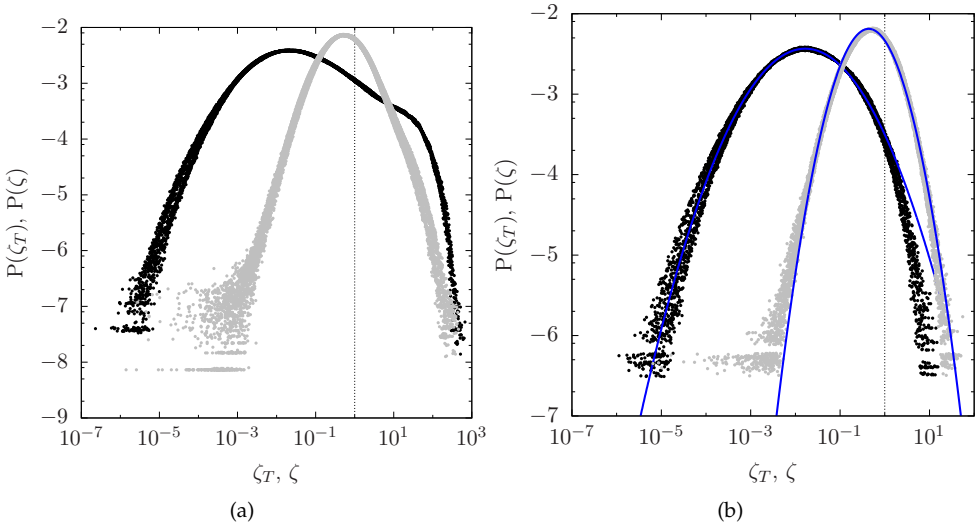

Figure 1.8: PDFs of normalized thermal and viscous dissipation rates, $\zeta_T = \epsilon_T / \langle \epsilon_T \rangle_{V,t}$ (black) and $\zeta = \epsilon / \langle \epsilon \rangle_{V,t}$ (grey), plotted within the whole cavity (a) and the bulk (V_{bulk}) (b), at $Ra = 10^8$. The solid blue lines in (b) indicate the fitted Gaussian distributions.

scales for both instantaneous dissipations at $Ra = 10^8$ (Figures 1.7(c) and 1.7(d)), in order to highlight the variation. They are displayed together with the instantaneous temperature (Figures 1.7(a) and 1.7(b)), all extracted at the horizontal plane (x-y) for ($z_{Ra=10^8} = 0.005$, $z_{Ra=10^{10}} = 0.002$), inside the BLs. We can note the fine filamentary structures of both dissipations highly correlated at the isothermal plate (BL), in corresponding to the ongoing thermal roots. A clearer picture over the spatial distributions of the viscous and thermal dissipation rates can be obtained through a statistical analysis. To do so, we plot the local probability density function (PDF) of the two terms, both across the entire volume of the cavity (Figure 1.8(a)) and the bulk, V_{bulk} (Figure 1.8(b)), at $Ra = 10^8$. The data is normalized by its temporal-volumetric averaged magnitudes using the following notations, $\zeta = \epsilon / \langle \epsilon \rangle_{V,t}$ and $\zeta_T = \epsilon_T / \langle \epsilon_T \rangle_{V,t}$, and represented in a logarithmic scale (exponential bin width divisions). In general, both dissipation rates have revealed a non-Gaussian PDF distribution with stretched-exponential tails exposing the small-scale intermittency in both the bulk and BL regions. This behaviour consists very well with the statistical dissipation behaviour reported in several previous studies such as, Scheel *et al.* [28] and Kaczorowski & Wagner [15].

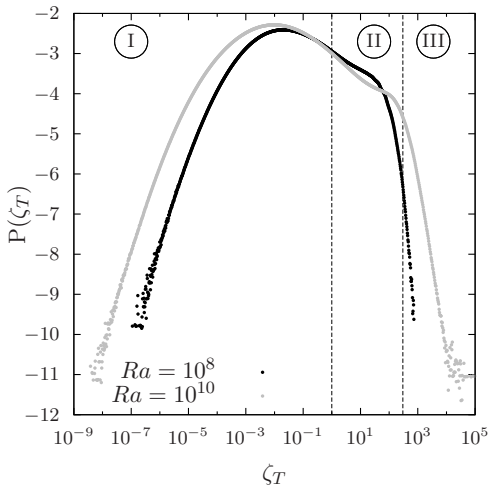

Figure 1.9: PDFs of normalized thermal dissipation rate $\zeta_T = \epsilon_T / \langle \epsilon_T \rangle_{V,t}$, plotted across the whole domain.

Basically, the thermal dissipation rate represents a reliable visualizer that indicates the evolution of thermal plumes following its thermal contrast and conductive heat transfer. Using its PDF distribution, Kaczorowski & Wagner [15] had separated the flow into three distinguished regions: (I) the bulk flow (turbulent background region), (II) the plumes/mixing layers and (III) the conductive sublayers. Similar to Ref. [15], our PDFs are displayed in Figure 1.9 and show the notable tendency of increasing the turbulent background contribution on account of decreasing the plumes region (steeper PDF), when the *Ra* number increases. The existence of the thermal BL and plumes implies that the PDF of ζ_T across the whole domain, deviates from the behaviour of a passive scalar convection (at $\zeta_T > 1$) [15]. Nonetheless, in the bulk region V_{bulk}, the PDF of ζ_T (Figures 1.10(a) and 1.8(b)) shows a picture similar to the results obtained in passive scalar convection [42]. The PDFs are neither symmetric nor Gaussian and for $\zeta_T \ll 1$ the Gaussian function falls below the PDFs, reflecting strong intermittency of the small scales. The right tail is fitted with a stretched exponential function for $\zeta_T > 10^{-3}$, given as

$$P(\zeta_T > 10^{-3}) = \frac{A_1}{\sqrt{\zeta_T}} \exp(-A_2 \zeta_T^{a/2}), \tag{1.34}$$

which was analytically derived for passive scalar turbulence with $a = 2/3$ in hard turbulent regime [43, 44]. The coefficients obtained through least-squares fits in

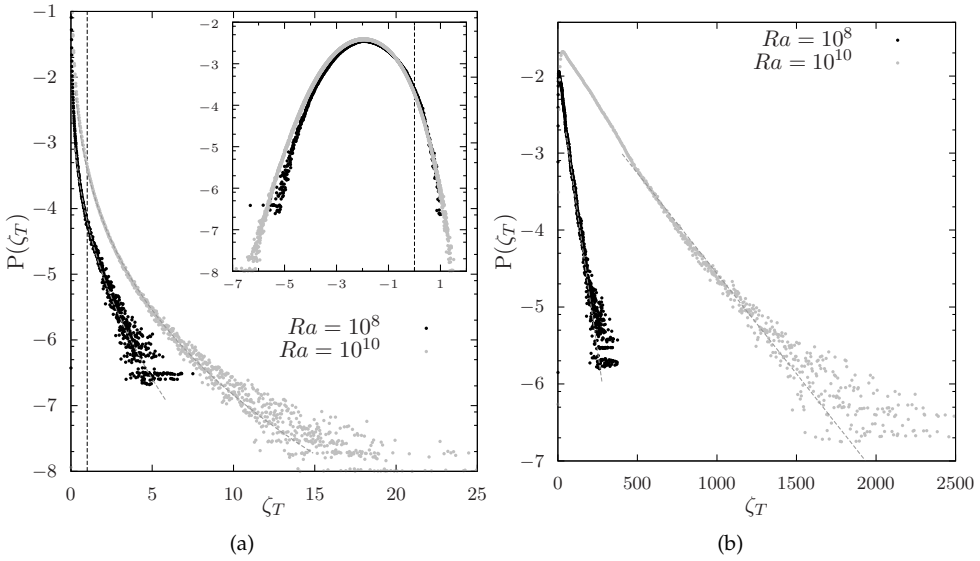

Figure 1.10: PDFs of normalized thermal dissipation rate $\zeta_T = \epsilon_T / \langle \epsilon_T \rangle_{V,t}$, plotted within the bulk (V_{bulk}) (a) and the thermal hot BL (b), with their respective least-squares fits (dashed lines). The inset in (a) shows the same PDFs on a log − log scale to illustrate the distribution of the small thermal dissipation rates.

Figure 1.10(a) read, $A_1 = 3 \times 10^{-3}$, $A_2 = 3.86$ and $a = 0.99$, at $Ra = 10^8$, and $A_1 = 8 \times 10^{-2}$, $A_2 = 5.33$ and $a = 0.71$, at $Ra = 10^{10}$. These findings in turn consist with Kaczorowski & Wagner [15], who observed the decreasing magnitude of a once the flow becomes fully turbulent with increasing Ra. *Thus, there seems to be a tendency for a to approach the theoretically predicted passive scalar scaling at high Ra* [15].

Likewise the bulk, the PDFs of ζ_T are plotted inside the thermal BL $(z = 0 \rightarrow \delta_T)$ in Figure 1.10(b). They show a fat stretched tail with a broader range of ζ_T by increasing the Ra. The vicinities of the conducting walls (BLs) hold the highest fluctuating values of the thermal dissipation rates $(\zeta_T > 100)$ in relevant to the thermal plumes, however, the smallest magnitudes of ζ_T, $(\zeta_T < 20)$ are centralized in the bulk. The distribution in Figure 1.10(b) follows an exponential scaling of the form,

$$P(\zeta_T >> 1) = B_1 \exp(-B_2 \zeta_T), \tag{1.35}$$

where the fitting coefficients read, $B_1 = 1 \times 10^{-2}, B_2 = 0.033$, for $Ra = 10^8$ and $B_1 = 1.1 \times 10^{-2}, B_2 = 0.006$, for $Ra = 10^{10}$. In consistency with [15], the exponent B_2 becomes smaller with increasing the Ra to imply a broader ζ_T range of significant

intermittent flow and increasing ratio of plumes emission at $Ra = 10^{10}$.

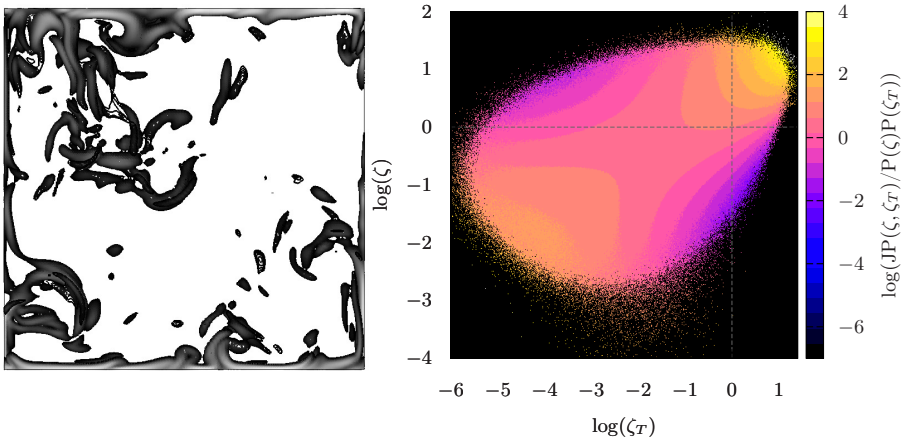

(a) (b)

Figure 1.11: (a) Vertically cut plane $(y\text{-}z)$ of instantaneous $\zeta_T > 1$ and $\zeta > 1$, at $Ra = 10^8$. (b) Represents the joint statistics $\Pi(\zeta, \zeta_T)$, given by Eq. 1.36, and plotted within the bulk (V_{bulk}), at the same Ra. The dashed lines in (b) refer to the mean dissipations.

Returning to Figure 1.8(a), the thermal dissipation rate seems to dominate the viscous dissipation in the range beyond its mean quantities, in regions of thermal plumes and conductive sublayers. Therein, the two dissipations tend to overlap at the largest events to manifest its important correlation at the BLs. However, in the bulk, ζ and ζ_T start to decorrelate because of the mixing action and conversely the kinetic dissipation becomes the dominant with more Gaussian and sharper PDF distribution (Figure 1.8(b)). The two dissipations tend again to overlap in the bulk at the rare largest values beyond the means. They indicate therefore, a small correlation associated with the expansion of plume chunks that travel far a way the BL through the bulk. One can verify further in Figure 1.11(a), where the viscous and thermal dissipative patterns that exceed the mean quantities *i.e.* $\zeta_T > 1$ and $\zeta > 1$, are shown. It can be seen how the high-amplitude dissipative structures interact and follow the mushroom-like plumes expanded in the bulk. These rare correlation events can also be underlined by plotting the joint PDF of the two dissipations, defined as

$$\Pi(\zeta, \zeta_T) = JP(\zeta, \zeta_T)/(P(\zeta)P(\zeta_T)), \tag{1.36}$$

and represented in Figure 1.11(b) at $Ra = 10^8$. Similar to Scheel *et al.* [28] findings, the

two dissipations are predominantly uncorrelated in the bulk unless at locations that exceed the unity values where the peak joint is observed. Finally, we should report that the essential behaviour of the kinetic and thermal energy dissipation rates in turbulent RBC is intimately implicated the true kinetic/thermal interaction mechanisms explained before in § 1.3.1. Moreover, these actions led in consistency, to the famous theory of Grossmann & Lohse [11, 29, 45], and recently [6], that splits the viscous dissipation rate into a bulk and BL contributions and the thermal dissipation rate into a background and plumes contributions. For detailed theoretical background about RBC and the scaling theories, the colloquium paper of Chillà and Schumacher [5], provides an overall reference for the readers.

1.3.3 Heat transport and wind

All findings before have indicated the vital relevance of the thermal/kinetic coupling mechanism with the thermal plumes advancement. Upon the type of flow (Pr) and its turbulence strength (Ra) the evolution of plumes is changing, and thus, the heat transfer mechanism, basically defined by Nu (Eq. 1.4). For example, when $Pr \gg 1$, the temperature exists on finer scales than velocity field and the plumes become narrower in less steep kinetic gradients [28]. While, at $Pr \ll 1$, as in liquid metals, the local bulk turbulent dissipation becomes stronger, *i.e.*, smaller dissipative scales develop since $\eta_k \propto Pr^{1/2}$ (Eq. 1.25), at the same time, an enhanced energy ejection occurs at larger spatial scale due to the coarser thermal plumes [46] and a decreasing scaling law β is found by Scheel & Schumacher [47]. Apart from the plumes dependence, there are another features that constrain the heat transport mechanism, such as the geometrical influence (confined nature dependent on Γ) and the feedback bulk dynamics. They determine the formation of the wind or Large-scale circulation (LSC) that fundamentally affects/controls the heat transport process in RBC. Historically, there are two different opinions about the origin of the LSC. The first one assumes, that the rolls that develop close to the onset of convection continue to exist at even the highest Ra, but only in an averaged sense [48]. The second one, proposed by Krishnamurti & Howard [49], considers the LSC as a high Rayleigh number effect, where the plumes detaching from the boundary layers interact with the mean shear. This results in tilted plumes generating a Reynolds stress to maintain a shear against dissipation. This idea is tested in chapter 3 and shown that the wind is driven by the mean buoyant forces at the sidewalls and no negative turbulent energy production (energy transport from fluctuations to the mean flow) takes place at the current setting. For large aspect ratio cells, Verdoold *et al.* [50] reported that the wind induces oscillations on time-scales far exceeding the turnover time, and these oscillations in turn, seem to be stronger as Ra increases. At high Ra, roughly around 10^{12}, Amati *et al.* [19] showed that the wind is substantially weakened. In the current study, we identify the LSC by performing an ensemble-averaging of flow

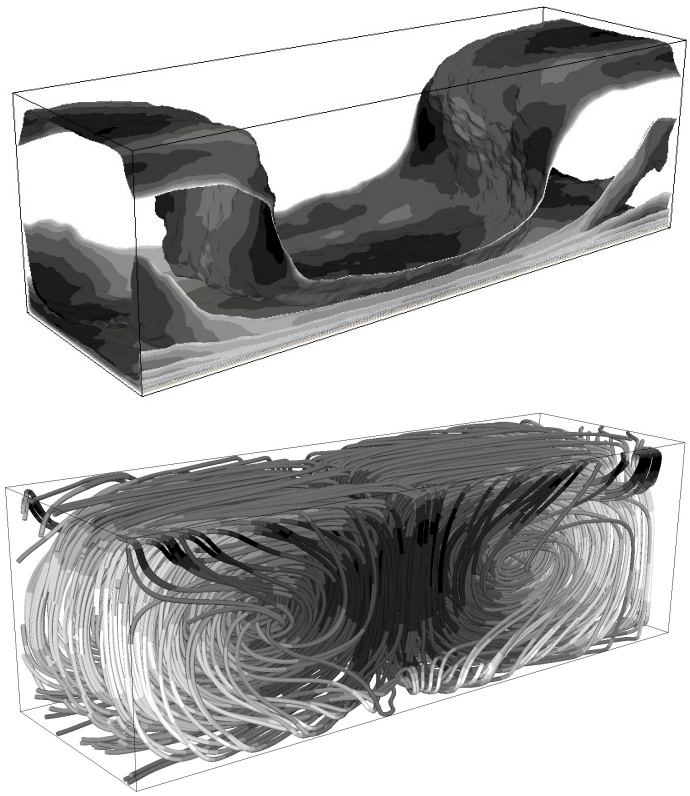

Figure 1.12: Results of ensemble-averaging at $Ra = 10^8$ for (a) 3D isosurfaces temperature, coloured by the turbulent kinetic energy $\langle k \rangle$, and (b) tubes of streamlines coloured by $\langle wT \rangle$. The gray scale is ascendantly changing from white to black in (a), and from maximum negative (black) to maximum positive (white), values in (b).

field in time. From Figure 1.12 (bottom), one can recognize the formation of two circulation rolls along the homogeneous x-direction at $Ra = 10^8$ (similarly observed at $Ra = 10^{10}$). The confined nature with the presence of sidewalls and isothermal top and bottom plates, seems to compact and enfold the two-cells wind. In Figure 1.12 (top), the 3D isosurfaces temperature, $T = 0 \rightarrow 0.5$, are drawn and clearly revealed the large scale organization. The isosurfaces are colored by the turbulent kinetic energy, $\langle k \rangle = \langle u'u' \rangle + \langle v'v' \rangle + \langle w'w' \rangle$, where the highest values (black) indicate the compression areas near the solid walls. Generally, these are the fingerprints of the role-like behaviour of the wind structure. The strength of the wind is roughly

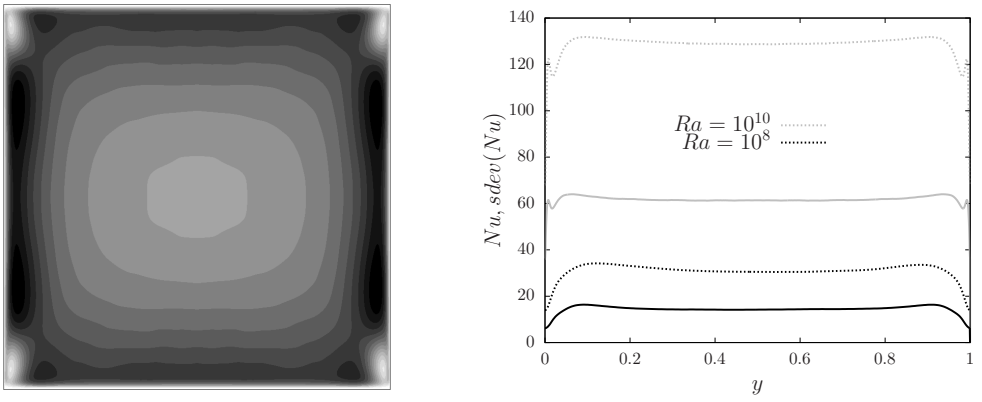

(a) (b)

Figure 1.13: (a) A vertical $(y\text{-}z)$ plane of turbulent heat flux $\langle w'T' \rangle$ averaged in x-direction, and colored by a gray scale ascendantly ranging from white to black, as $\langle w'T' \rangle \in [0, 0.00415]$, at $Ra = 10^8$. (b) Displays the local Nu distribution at the hot plate (dashed lines) together with its standard deviation (solid lines) for $Ra = 10^8$ (black) and $Ra = 10^{10}$ (gray).

characterized by the Reynolds number, defined as, $Re = H\sqrt{\langle k \rangle_{V,t} Ra/Pr}$. It relates with the turbulence strength, Ra, by a scaling law function given by, $Re \sim Ra^{\gamma}$, and reads here as, $Re = 0.32 Ra^{0.475}$. In turn, this exponent matches very well the scaling of Emran *et al.* [25] ($\gamma = 0.475$) and ($\gamma = 0.45$ in Emran *et al.* [26]), who dealt with a cylindrical cell. In Figure 1.12 (bottom), the streamline tubes across the whole domain are drawn and colored by the dominant heat transport, $\langle wT \rangle$, in correspondence to positive (white) and negative (black) values. Therewith, the coherent wind is falling at the midway distance in the longitudinal x-direction and rising at the periodic open-ends. It conveys a cold fluid of negative heat flux, $\langle wT \rangle < 0$, at the middle, and a hot fluid at the adjoining rising flow of positive heat transfer $\langle wT \rangle > 0$. The wind stirs the bulk fluid inside the two helical LSCs and the turbulence bulk arises as a consequence to transport the heat through the bulk. The turbulent heat flux measured as the buoyant production, $\langle w'T' \rangle$, appears to obtain its maximum values in the vicinities of the sidewalls, as shown in Figure 1.13(a). It indicates that the buoyant sidewall-flow is mostly characterized by incorporating groups of thermal plumes. The local Nu (averaged in x) at the heating plate in y positions, and its standard deviation $sdev(Nu)$, calculated as, $sdev(Nu) = \partial\sqrt{\langle T'^2 \rangle}/\partial z|_{z=0}$, are plotted together in Figure 1.13(b). It can be observed that a maximum global heat transport happens in relation to the thermal plumes accumulating and traveling next to the sidewalls.

The the boundary layer flow is laminar regime, obeying the Prandtl-Plasius scaling theory of Grossmann & Lohse [45] ($\delta_T = 0.5H/Nu$). The mean sidewall circulation is essentially reduced/diminished in the higher turbulent case, where $sdev(Nu)$ is trivially modified.

1.4 Conclusions

A set of complete 3D direct numerical simulations of turbulent RBC in a rectangular air-filled cavity of aspect ratio $\Gamma = 1$ and π spanwise open-ended distance, have been presented at two $Ra = \{10^8, 10^{10}\}$. Numerically, an explicit scheme has been used for temporal integration and a 4^{th}-order symmetry preserving scheme for spatial discretization. This scheme preserves the global kinetic energy balances even for very coarse grids. The trustworthy DNS grids which are appropriate to resolve all relevant turbulent scales, both in the bulk and near-wall areas, are constructed upon refinement tests on the base of Grötzbach [35] criterion. They adopt the lowest computational cost possible with the aid of a maximum coarsening approach in the homogeneous x-direction, without losing accuracy. On the other hand, they satisfy and exceed the current DNS resolution requirements for the BLs, proposed by Shishkina *et al.* [36]. As a result, the Nu findings present a good consistency with literature [28, 29].

The main findings read that an amplified coupling of kinetic and thermal turbulent fluctuations takes place in the boundary layers next to the heating and cooling isothermal plates. They induce the formation of patterns of sheet-like plumes leading to important interaction/correlation of viscous and thermal energy dissipation rates in the BLs. Both dissipations therein, reveal a non-Gaussian PDF distribution with stretched-exponential tails exposing the small-scale intermittency. They hold high amplitude events exceeding its temporal and volumetric averaged values, and a domination of the thermal dissipation over the viscous one occurs inside the BL. At the intersection points of the roots the plumes convolute and swirl away by buoyancy to arise into the bulk as mushroom-like plumes. As a result of the mixing action, the plumes dissipate in the bulk transforming its portable thermal energy into kinetic one and lead to a decorrelation action of the thermal and viscous dissipation rates. The viscous dissipation therefore, is conversely dominating in the bulk and the two dissipation are only correlated at the rare largest values beyond the means in association with the plume chunks in the bulk.

The coherent large-scale circulation or the wind has been identified using an ensemble-averaging of flow field in time. Two helical rolls are distinguished along the homogeneous x-direction, and enfolded by the solid walls. The interaction compression areas between the wind and the walls are found to be indicated by the

largest magnitudes of the turbulent kinetic energy. Generally, the wind organization is constituted into a cold falling down fluid of negative heat flux at the middle of the π periodic distance, and two rising up hot fluid at the adjoining open-ended sides with a positive heat flux. The turbulent heat flux is found to be maximal in the vicinities of the sidewalls in relevant to the plumes traveling over there; and the mean sidewall circulation is notably reduced/diminished at $Ra = 10^{10}$.

References

[1] E. D. Sigga. High Rayleigh number convection. *Annual Reviews of Fluid Mechanics*, 26:137, 1994.

[2] H. Bénard. Les tourbillons cellulaires dans une nappe liquide. - Méthodes optiques d'observation et d'enregistrement. *Journal of Theoretical and Applied Physics*, 10:254–266, 1901.

[3] L. Rayleigh. LIX.On convection currents in a horizontal layer of fluid, when the higher temperature is on the under side. *The London, Edinburgh, and Dublin Philosophical Magazine and Journal of Science*, 32:52–546, 1916.

[4] G. Ahlers, S. Grossmann, and D. Lohse. Heat transfer and large scale dynamics in turbulent Rayleigh-Bénard convection. *Reviews of Modern Physics*, 81:503–537, 2009.

[5] F. Chillà and J. Schumacher. New perspectives in turbulent Rayleigh-Bénard convection. *The European Physics Journal E*, 35:58, 2012.

[6] R. J. A. M. Stevens, E. P. van der Poel, S. Grossmann, and D. Lohse. The unifying theory of scaling in thermal convection: the updated prefactors. *Journal of Fluid Mechanics*, 730:295–308, 2013.

[7] B. Castaing, G. Gunaratne, F. Heslot, L. Kadanoff, A. Libchaber, S. Thomae, X. Wu, S. Zaleski, and G. Zanetti. Scaling of hard thermal turbulence in Rayleigh-Bénard convection. *Journal of Fluid Mechanics*, 204(1):1–30, 1989.

[8] X. Chavanne, F. Chillá, b. Chabaud, B. Castiang, and B. Hébral. Turbulent Rayleigh-Bénard convection in gaseous and liquid He. *Physics of Fluids*, 13:1300, 2001.

[9] P. E. Roche, F. Gauthier, R. Kaiser, and J. Salort. On the triggering of the ultimate regime of convection. *New Journal of Physics*, 12:085014, 2010.

[10] R. H. Kraichnan. Turbulent thermal convection at arbitrary prandtl number. *Physical Fluids*, 5:1374, 1962.

[11] S. Grossmann and D. Lohse. Multiple scaling in the ultimate regime of thermal convection. *Journal Physics of Fluids*, 23:045108, 2011.

[12] J. Niemela and K. R. Sreenivasan. Turbulent convection at high Rayleigh numbers and aspect ratio 4. *Journal of Fluid Mechanics*, 557:411–422, 2006.

[13] X. He, D. Funfschiling, H. Nobach, E. Bodenschatz, and G. Ahlers. Transition to the ultimate state of turbulent Rayleigh-Bénard convection. *Physical Review Letters*, 108:024502, 2012.

[14] R. Kerr. Rayleigh number scaling in numerical convection. *Journal of Fluid Mechanics*, 310:139, 1996.

[15] M. Kaczorowski and C. Wagner. Analysis of the thermal plumes in turbulent Rayleigh-Bénard convection based on well-resolved numerical simulations. *Journal of Fluid Mechanics*, 618:89–112, 2009.

[16] M. Kaczorowski and K. Xia. Turbulent flow in the bulk of Rayleigh-Bénard convection: small-scale properties in a cubic cell. *Journal of Fluid Mechanics*, 722:596–617, 2013.

[17] R. Bolgiano. Turbulent spectra in a stably stratified atmosphere. *Journal of Geophysical Research*, 64:2226–2229, 1959.

[18] M. Kaczorowski, K. Chong, and K. Xia. Turbulent flow in the bulk of Rayleigh-Bénard convection: aspect-ratio dependence of the small-scale properties . *Journal of Fluid Mechanics*, 747:73–102, 2014.

[19] G. Amati, K. Koal, F. Massaioli, K. R. Sreenivasan, and R. Verzicco. Turbulent thermal convection at high Rayleigh numbers for a boussinesq fluid of constant Prandtl number. *Physics of Fluids*, 17:121701, 2005.

[20] R. A. J. M. Stevens, R. Verzicco, and D. Lohse. Radial boundary layer structure and Nusselt number in Rayleigh-Bénard convection. *Journal of Fluid Mechanics*, 643:495–507, 2010.

[21] R. J. A. M. Stevens, D. Lohse, and R. Verzicco. Prandtl and Rayleigh number dependence of heat transport in high Rayleigh number thermal convection. *Journal of Fluid Mechanics*, 688:31–43, 2011.

[22] O. Shishkina and C. Wagner. Analysis of thermal dissipation rates in turbulent Rayleigh-Bénard convection. *Journal of Fluid Mechanics*, 546:51–60, 2006.

[23] O. Shishkina and C. Wagner. Local heat fluxes in turbulent Rayleigh-Bénard convection. *Physics of Fluids*, 19:085107, 2007.

[24] O. Shishkina and C. Wagner. Analysis of sheet-like thermal plumes in turbulent Rayleigh-Bénard convection. *Journal of Fluid Mechanics*, 19:085107, 2007.

[25] M. S. Emran and J. Schumacher. Fine-scale statistics of temperature and its derivatives in convective turbulence. *Journal of Fluid Mechanics*, 611:13–34, 2008.

[26] M. S. Emran and J. Schumacher. Conditional statistics of thermal dissipation rate in turbulent Rayleigh-Bénard convection. *The European Physical Journal E*, 35:108, 2012.

[27] M. S. Emran and J. Schumacher. Large-scale mean patterns in turbulent convection. *Journal of Fluid Mechanics*, 776:96–108, 2015.

[28] J. Scheel, M. S. Emran, and J. Schumacher. Resolving the fine-scale structure in turbulent Rayleigh-Bénard convection. *New Journal of Physics*, 15:113063, 2013.

[29] S. Grossmann and D. Lohse. Fluctuations in turbulent Rayleigh-Bénard convection: The role of plumes. *Physics of Fluids*, 1:4462–4472, 2004.

[30] R. W. C. P. Verstappen and A. E. P. Veldman. Symmetry-preserving discretization of turbulent flow. *Journal of Computational Physics*, 187:343–368, 2003.

[31] F. X. Trias and O. Lehmkuhl. A self-adaptive strategy for the time-integration of Navier-Stokes equations. *Numerical Heat Transfer, part B*, 60(2):116–134, 2011.

[32] A. J. Chorin. Numerical solution of the Navier-Stokes equation. *Mathematics of Computation*, 22:745–762, 1968.

[33] A. Gorobets, F. X. Trias, and A. Oliva. A parallel MPI+OpenMP+OpenCL algorithm for hybrid supercomputations of incompressible flows. *Computers and Fluids*, 88:764–772, 2013.

[34] F. X. Trias, M. Soria, C. D. Pérez-Segarra, and A. Oliva. Direct numerical simulation of two- and three-dimensional turbulent natural convection flows in a differentially heated cavity of aspect ratio 4. *Journal of Fluid Mechanics*, 586:259–293, 2007.

[35] G. Grötzbach. Spatial resolution requirements for direct numerical simulation of the Rayleigh-Bénard convection. *Journal of Computational Physics*, 49:241–264, 1983.

[36] O. Shishkina, R. J. A. M. Stevens, S. Grossmann, and D. Lohse. Boundary layer structure in structure in turbulent thermal convection and consequences for the required numerical resolution. *New Journal of Physics*, 12:075022, 2010.

[37] M. Van Reeuwijk, H. J. J. Jonker, and K. K. Hanjalić. Identification of the wind in Rayleigh-Bénard convection. *Physics of Fluids*, 17(5):051704, 2005.

[38] E. Brown, A. Nikolaenko, and G. Ahlers. Reorientation of the large-scale circulation in turbulent Rayleigh-Bénard convection. *Physical Review Letters*, 95:084503, 2005.

[39] F. F. Araujo, S. Grossmann, and D. Lohse. Wind reversals in turbulent Rayleigh-Bénard convection. *Physical Review Letters*, 95(8):084502, 2005.

[40] J. Scheel and J. Schumacher. Local boundary layer scales in turbulent Rayleigh-Bénard convection. *Journal of Fluid Mechanics*, 758:344–373, 2014.

[41] F. Dabbagh, F. X. Trias, A. Gorobets, and A. Oliva. Spectrally-consistent regularization of turbulent Rayleigh-Bénard convection. *6th European Conference on Computational Fluid Dynamics*, pages 7144–7155, 2014.

[42] J. Schumacher and K. R. Sreenivasan. Statistics and geometry of passive scalars in turbulence. *Physics of Fluids*, 17:125107, 2005.

[43] M. Chertkov, G. Falkovich, and I. V. Kololkov. Intermittent dissipation of a passive scalar in turbulence. *Physical Review Letters*, 80:2121–2124, 1998.

[44] A. Gamba and I. V. Kololkov. Dissipation statistics of a passive scalar multidimensional smooth flow. *Journal of Statistical Physics*, 94:759–777, 1999.

[45] S. Grossmann and D. Lohse. Scaling in thermal convection: A unifying theory. *Journal of Fluid Mechanics*, 407:27–56, 2000.

[46] J. Schumacher, P. Grötzfried, and J. D. Scheel. Enhanced enstrophy generation for turbulent convection in low-Prandtl-number fluids. *Proceedings of the National Academy of Sciences of the USA*, 112:9530–9535, 2015.

[47] J. D. Scheel and J. Schumacher. Global and local statistics in turbulent convection at low Prandtl numbers. *Journal of Fluid Mechanics*, 802:147–173, 2016.

[48] D. E. Fitzjarrald. An experimental study of turbulent convection in air. *Journal of Fluid Mechanics*, 73:693–719, 1976.

[49] R. Krishnamurti and L. N. Howard. Large-scale flow generation in turbulent convection. *Proceedings of the National Academy of Sciences of the USA*, 78:1981–1985, 1981.

[50] J. Verdoold, M. Tummers, and K. K. Hanjalić. Oscillating large-scale circulation in turbulent Rayleigh-Bénard convection. *Physical Reviews E*, 73:056304, 2006.

2

On the evolution of flow topology in turbulent Rayleigh-Bénard convection

Main contents of this chapter have been published in:

F. Dabbagh, F. X. Trias A. Gorobets and A. Oliva, On the evolution of flow topology in turbulent Rayleigh-Bénard convection , *Physics of Fluids*, **28**, 115105, 2016.

F. Dabbagh, F. X. Trias A. Gorobets and A. Oliva, Fine-scale dynamics in turbulent Rayleigh-Bénard convection, *THMT-15. Proceedings of the* 8^{th} *International Symposium On Turbulence, Heat and Mass Transfer*, September, 2015.

Abstract. Small-scale dynamics is the spirit of turbulence physics. It implicates many attributes of flow topology evolution, coherent structures, hairpin vorticity dynamics and mechanism of the kinetic energy cascade. In this chapter, several dynamical aspects of the small scale motions have been numerically studied in a framework of Rayleigh-Bénard convection (RBC). To do so, results from the direct numerical simulations in chapter 1, have been used. As a main feature, the average rate of the invariants of the velocity gradient tensor $(Q_{\mathsf{G}}, R_{\mathsf{G}})$ have displayed the so-called "teardrop" spiraling shape through the bulk region. Therein, the mean trajectories are swirling inwards revealing a periodic spin around the converging origin, of

a constant period that is found to be proportional to the plumes lifetime. Supplementary small-scale properties, which are widely common in many turbulent flows have been observed in RBC. For example, the strong preferential alignment of vorticity with the intermediate eigenstrain vector, and the asymmetric alignment between vorticity and the vortex-stretching vector. It has been deduced that in a hard turbulent flow regime, local self-amplifications of straining regions aid in contracting the vorticity worms, and enhance the local interactions vorticity/strain to support the linear vortex-stretching contributions. On the other hand, the evolution of invariants pertained to the traceless part of velocity-times-temperature gradient tensor have also been considered in order to determine the role of thermals in the fine-scale dynamics. By applying an identical approach, the rates of the new invariants have shown a symmetric cycling behaviour decaying towards two skew-symmetric converging origins at the lower *Ra* number. At the hard turbulent case, the spiraling trajectories travel in shorter tracks to reveal the reduced lifetime of plumes under the dissipative and mixing effects. The turbulent background kinetic derivatives get self amplified and the trajectories converge to a zero-valued origin. These and other peculiar scrutinies on the small scale motions in RBC have been enlightened, and may have a fruitful consequence on modelling approaches of buoyancy-driven turbulence.

2.1 Introduction

"Turbulent flow constitutes an unusual and difficult problem of statistical mechanics, characterized by extreme statistical disequilibrium, by anomalous transport processes, by strong dynamical nonlinearity, and by perplexing interplay of chaos and order" (Kraichnan [1]). Nevertheless, understanding the qualitative contents of the governing equations of turbulence can elucidate many physics therein. Namely, generic structural properties of the mathematical governing objects, called (strange) attractors, which are invariants in some sense, include many ingredients of turbulence physics (Tsinober [2]). Hence, the key point is in the small scale motions, and their universal qualitative aspects commonly found in a wide variety of turbulent flows. They result from the subtle balance between convective transport and diffusive dissipation to be definitely blameworthy of generating the hairpin vorticity dynamics, non-Gaussianity, strain/dissipation production and the cascade of kinetic energy mechanisms. Studying their evolution gives us fundamental perspectives of flow topology and thus, many physics of turbulence become intelligible.

Since the early 90s, a major attention has been given to the important role of velocity derivatives in the topological classification of fluid motions [3] and the small-scale dynamics [4,5]. Thereby, several universal features of the small scale turbulence are observed, *e.g.* the inclined "teardrop" shape of the joint probability density function (PDF) of Q_G (the second) and R_G (the third) invariants of the velocity gradient tensor, and the essential preferential alignment of vorticity with the intermediate eigenvector of the rate-of-strain tensor. They have been observed in various turbulent flow configurations such as isotropic turbulence [5], turbulent boundary layer [6], channel flow [7], turbulent mixing layer [8] and turbulent jets [9]. However, their thermally driven analogues, as in the developed natural convection flow heated from below and cooled from above, namely Rayleigh-Bénard convection (RBC), are far from being satisfactory.

Buoyancy-driven flow in RBC has always been an important subject of scientific studies with numerous applications in environment and technology. Its resultant dynamics is strongly featured by intrinsic instabilities, counter-gradient diffusion, augmented pressure fluctuations and strong interactions between kinetics and thermals diversely distributed over flow regions. This nature has inspired significant inherent complexities in the view of turbulence models, and the proper reproduction to the coherent large-scale circulations in RBC [10]. Therefore, understanding the dynamics of small scale motions and their lifetime evolution can play a major role in the scope of turbulence modeling. The small-scale properties were a focal point for many authors, *e.g.* Lohse and Xia [11], who investigated the so-called Bolgiano-Obukhov scaling existence within RBC. Moreover, the direct numerical simulation

(DNS) of Schumacher [12] and experiments of Gasteuil *et al.* [13] have monitored the turbulent local evolution of the thermal plumes in a Lagrangian frame to explore important statistical aspects of heat and momentum transport mechanisms. Some authors focused on studying the substantial turbulent components of thermal and kinetic energy dissipation rates [14,15], as we similarly performed in chapter 1. Only Schumacher *et al.* [16] have recently shed light on the universality picture of small scales in RBC regarding their scaling law performance. Even more recently, Park and Lee [17] have addressed a new study of the coherent structures in RBC using the joint PDF of the velocity gradient tensor. Their analysis [17] is limited to a soft turbulence regime, and no descriptions on the universal features of the small scale motions, the mechanisms of their dynamics and flow topology changes are given.

In this chapter, we provide an investigation on the dynamical universal features of small scale motions in RBC, commonly observed in many turbulent flows. Basically, the average evolution of Q_{G} and R_{G} invariants (defined in § 2.2) of velocity gradient tensor $\mathsf{G} = \nabla \boldsymbol{u}$, is studied within the bulk region to show the cyclical action of flow topology change converging towards the origin. By doing so, we extend the averaging dynamical approach applied to isotropic turbulence [4,5] and a turbulent boundary layer (BL) [6], to include the topology dynamics of RBC through the bulk. Important insights concerning the dynamics at hard turbulent regime, and the characteristic lifetime of the coherent energy containing eddies are explored, where the universal essential alignments of vorticity with straining and vortex-stretching geometries are addressed. On the other hand, an identical approach is considered for the novel invariants $Q_{\tilde{\mathsf{G}}_\theta}$ and $R_{\tilde{\mathsf{G}}_\theta}$ (defined in § 2.3) of the traceless part of the velocity-times-temperature gradient tensor $\tilde{\mathsf{G}}_\theta = \nabla(\boldsymbol{u}T) - 1/3tr(\nabla(\boldsymbol{u}T))\mathsf{I}$. The new invariants are introduced as combinations of thermal and kinetic small-scale topology and related predominantly with the dynamics of thermal plumes and turbulent heat flux. The new dynamical equations are deduced and the material averaging procedure is applied in order to provide new aspects of the life cycle of the small scales pertained to the thermals, which become worthwhile in turbulence modeling of RBC.

The remainder of this chapter is organized as follows. In § 2.2, the universal features of fine-scale dynamics and flow topology are discussed by analysing the averaged evolution of the classical velocity gradient tensor invariants. The pioneering invariants of the new velocity-times-temperature gradient tensor are considered and analysed identically in § 2.3. Finally, conclusions and future remarks are reported.

2.2 Invariants of $\nabla \boldsymbol{u}$ tensor

Extensive background material concerning the crucial role of velocity gradients in the topological classification of the flow and small-scale dynamics can be found in many works, *e.g.* Chong *et al.* [3], Cantwell *et al.* [18], Blackburn *et al.* [7], Soria *et al.* [8], Perry and Chong [19], Martín *et al.* [4], Ooi *et al.* [5] and others. A short review of the definitions and the physical meaning of the invariants of the velocity gradient tensor $\mathsf{G} = \nabla \boldsymbol{u}$ are given here for incompressible flow. Namely,

$$P_{\mathsf{G}} = -tr(\mathsf{G}) = -\nabla \cdot \boldsymbol{u} = 0, \tag{2.1}$$

$$Q_{\mathsf{G}} = -\frac{1}{2} tr(\mathsf{G}^2) = \frac{1}{4}\left[\boldsymbol{\omega}^2 - 2tr(\mathsf{S}^2)\right] = Q_{\Omega} + Q_{\mathsf{S}}, \tag{2.2}$$

$$R_{\mathsf{G}} = -det(\mathsf{G}) = -\frac{1}{3} tr(\mathsf{G}^3) = -\frac{1}{3}\left[tr(\mathsf{S}^3) + 3tr(\Omega^2 \mathsf{S})\right] = R_{\mathsf{S}} - tr(\Omega^2 \mathsf{S}), \tag{2.3}$$

where P_{G}, Q_{G} and R_{G} are the first, second and third invariant of G, respectively. It is

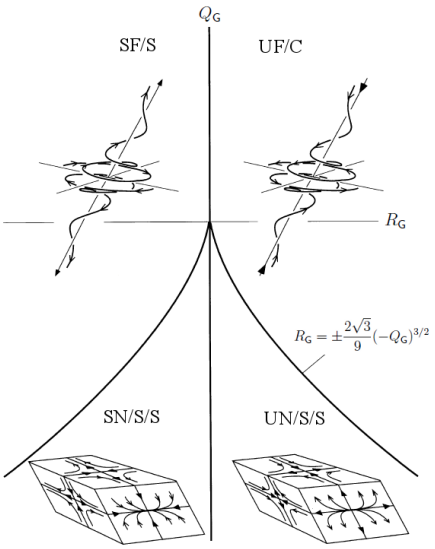

Figure 2.1: Classification of local flow topology following $(Q_{\mathsf{G}}, R_{\mathsf{G}})$ invariants of velocity gradient tensor for incompressible flow [taken from Ooi *et al.* [5], with SF/S: stable focus/stretching, SN/S/S: stable node/saddle/saddle, UN/S/S: unstable node/saddle/saddle and UF/C: unstable focus/compressing.

useful to recall that G can be decomposed into its symmetric and antisymmetric parts,

$\mathsf{S} = 1/2(\mathsf{G} + \mathsf{G}^t)$ and $\Omega = 1/2(\mathsf{G} - \mathsf{G}^t)$, respectively, where S denotes the rate-of-strain tensor, and Ω is the rate-of-rotation tensor. Their invariants play an important role in the identification of coherent structures [3, 5, 7, 9], and the development of new turbulence models [20]. For example, the second invariant $Q_\Omega = -1/2tr(\Omega^2) = 1/4|\boldsymbol{\omega}|^2$ is proportional to the enstrophy density. Therefore, it identifies tube-like structures with high vorticity $\boldsymbol{\omega} = \nabla \times \boldsymbol{u}$. The invariant $Q_\mathsf{S} = -1/2tr(\mathsf{S}^2) = -1/4(\epsilon/\nu)$ is proportional to the local rate of viscous dissipation, $\epsilon = 2\nu\mathsf{S}\colon\mathsf{S}$. Notice that $Q_\Omega \geq 0$ and $Q_\mathsf{S} \leq 0$ and these two invariants are related to Q_G with the identity (2.2). Hence, positive values of $Q_\mathsf{G} > 0$ are related to areas of enstrophy domination over viscous dissipative straining. Another important term is the third invariant of S *i.e.* $R_\mathsf{S} = -1/3tr(\mathsf{S}^3)$. It constitutes a part of the straining production (see Eq. 2.9), and R_G in the identity (2.3). Moreover, it correlates the three eigenvalues of S as $R_\mathsf{S} = -\sigma_1\sigma_2\sigma_3$, where $\sigma_1 \geq \sigma_2 \geq \sigma_3$ are arranged in a descending order. Due to incompressibility, the sum $\sigma_1 + \sigma_2 + \sigma_3 = 0$, and the sign of R_S follows the sign of the intermediate eigenvalue to categorise the structures shape to tube-like $R_\mathsf{S} < 0$ or sheet-like $R_\mathsf{S} > 0$. Generally speaking, when $R_\mathsf{G} < 0$ and $Q_\mathsf{G} \gg 0$, a positive enstrophy production is prevalent, and stable tube-like vortex stretching structures (the so-called worms) predominate the vorticity compression. However, when $R_\mathsf{G} > 0$ and $Q_\mathsf{G} \ll 0$, the straining production becomes the dominant one and associates mostly with strong and unstable sheet-like viscous dissipative structures. Figure 2.1 shows the four main classes of the possible flow topology in $(Q_\mathsf{G}, R_\mathsf{G})$ phase plane taken from Ooi *et al.* [5], where more details thereof can be found in the above references.

2.2.1 Universal aspects of turbulence structures

Many turbulent flows have revealed an inclined "teardrop" shape of the joint PDF $(Q_\mathsf{G}, R_\mathsf{G})$, which has been speculated as a kind of universality in the space of invariants [2]. Despite the different global flow geometries created in many types of turbulence, *e.g.* an isotropic turbulence [5], turbulent boundary layer [6], turbulent channel flow [7] and others [8, 9], all displayed the same feature of preferred $(Q_\mathsf{G}, R_\mathsf{G})$ statistical correlation in areas dominated by small-scale vortex stretching and viscous dissipation structures. This behaviour as a common aspect of 3D turbulence and its Gaussian-deviation property, is extended here to include the buoyancy-driven flows in a Rayleigh-Bénard framework at hard turbulent regime.

To do so, the joint PDFs of Q_G and R_G invariants through the bulk (V_{bulk}), have been plotted in Figure 2.2. The invariants are normalized using $\langle Q_\Omega \rangle$ (following Ooi *et al.* [5]) to show the same "teardrop" shape as a universal feature of the small scale motions in both turbulent cases. As can be seen, Figures 2.2(a) and 2.2(b) indicate that most of the flow domain is occupied by coherent dynamics of small mean gradients

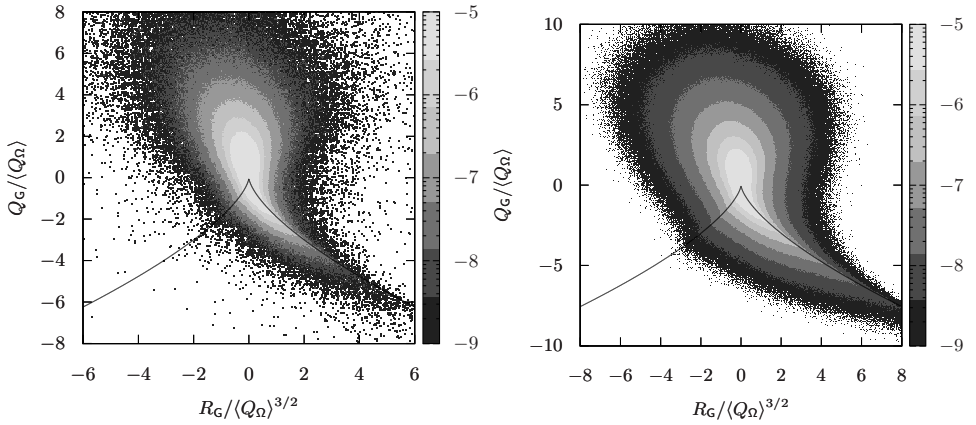

Figure 2.2: Joint PDF of normalized Q_G and R_G invariants on logarithmic scale at (a) $Ra = 10^8$ and (b) $Ra = 10^{10}$ through the bulk (V_{bulk}), where the solid black line represents the null-discriminant curve $D_G = (27/4)R_G^2 + Q_G^3 = 0$.

around the origin; while the rest of the flow *i.e.* fluctuations and small scales, obey substantially stable tube-like focus/stretching structures ($Q_G > 0$ and $R_G < 0$), and unstable sheet-like node/saddle/saddle topologies ($Q_G < 0$ and $R_G > 0$ the so-called Vieillefosse tail).

In order to gain an understanding of the spatial structure of turbulence, an instantaneous 3D visualization of Q_G iso-surface at high positive values is plotted in Figure 2.3. The structures take the shape of the so-called worms [2], which are classified as stable tube-like focal stretching topology of intensive enstrophy values. As can be seen in Figure 2.3(a), the worms are characterized by large fragmentations with an elliptical cross-section in the case of $Ra = 10^8$. They seem to be aligned in many places with the evolution of the thermal plumes (hot 2D black contours), which expand in the bulk to support the prevalence of the tube-like rotational topology.
Plotting the joint PDF map of Q_Ω and $-Q_S$ invariants can provide significant physical information about the dominant flow topologies respect to the kinetic energy dissipation. For example, points of high enstrophy (Q_Ω), but very small dissipation ($-Q_S$), indicate solid-body rotational structures (vortex tubes), while points of strong dissipation but little enstrophy represent irrotational straining domination. Balanced distribution of $Q_\Omega = -Q_S$ translates a vortex sheet topology that normally occurs in the BLs. As shown in Figures 2.4(a) and 2.4(b), the flow topology is mainly tube-like rotational in the bulk region, where the highest local value of $-Q_S$ is smaller than

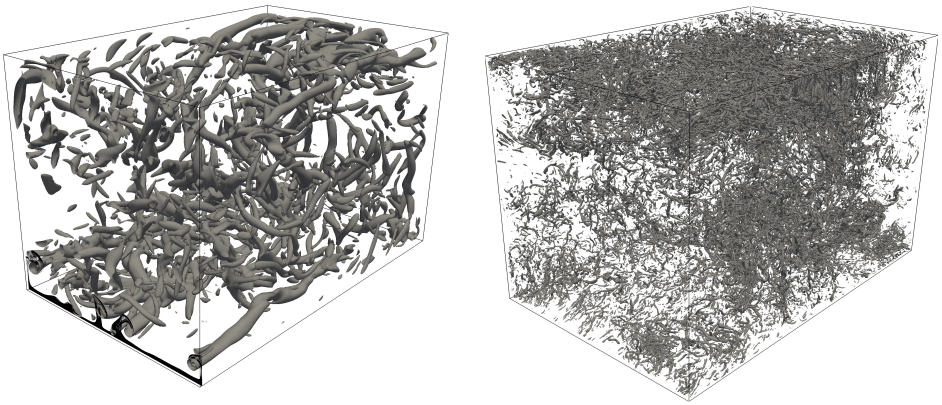

(a) (b)

Figure 2.3: Structures of Q_G positive values drawn in a portion of the domain for (a) $Ra = 10^8$ ($Q_G > 14.29$) and (b) $Ra = 10^{10}$ ($Q_G > 128.9$) (See movies of their dynamics [http://dx.doi.org/10.1063/1.4967495.1]). The solid black contours in (a) indicate the hot thermal plumes.

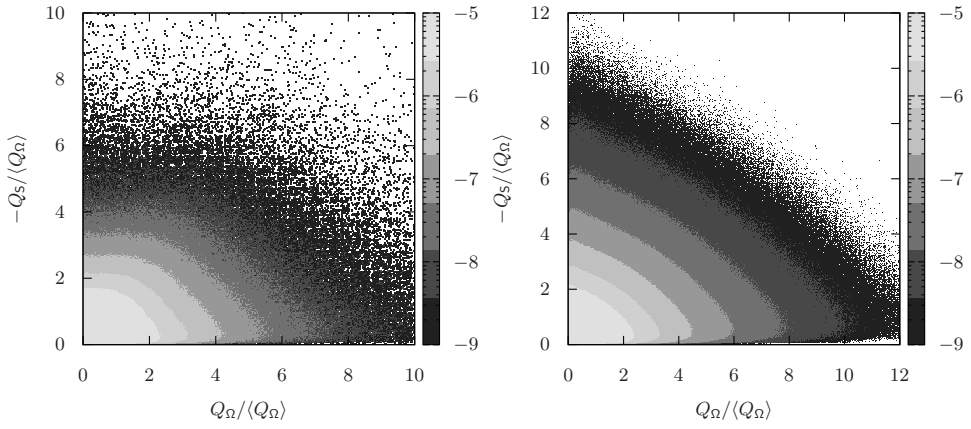

Figure 2.4: Joint PDF of normalized Q_Ω and $-Q_S$ invariants on logarithmic scale at (a) $Ra = 10^8$ and (b) $Ra = 10^{10}$, through the bulk (V_{bulk}).

the highest local value of Q_Ω, and the joint PDF is skewed towards high Q_Ω with long-lived solid-body rotation.

When the flow becomes significantly turbulent at $Ra = 10^{10}$, the turbulent background velocity derivatives as $-Q_\mathsf{S}$ (the viscous strain and Q_Ω in concomitant), get self-amplified [2]. They often surpass the original large-scale forces generated here by buoyancy, as reported by Tsinober [2]. This self-growing of turbulent dissipation $-Q_\mathsf{S}$ can be clearly identified in the $(Q_\Omega, -Q_\mathsf{S})$ map in Figure 2.4(b). It works on contracting the worms to be composed in smaller and numerous fragments within the bulk (see Figure 2.3(b)). Physically, the nonlinearities as the enstrophy production $(4tr(\Omega^2\mathsf{S}) = \boldsymbol{\omega} \cdot \boldsymbol{\omega}\mathsf{S})$, become increased, and conduct the local growing of the strain-dominated regions. While, an enhanced equilibrium between these nonlinearities (*e.g.* the vortex-stretching vector $\boldsymbol{\omega}\mathsf{S}$), and its viscous destruction $(Pr/Ra)^{1/2}\boldsymbol{\omega}\nabla^2\boldsymbol{\omega}$ take place mostly in regions of enstrophy concentrations (*i.e.* the worms) [2]. These processes are explained and justified in detail by Tsinober [2]. They are essentially interconnected in the frame of the enstrophy transport equation:

$$\frac{1}{2}\frac{D|\boldsymbol{\omega}|^2}{Dt} = \boldsymbol{\omega} \cdot \boldsymbol{\omega}\mathsf{S} + \sqrt{\frac{Pr}{Ra}}\boldsymbol{\omega}\nabla^2\boldsymbol{\omega} + \boldsymbol{\omega} \cdot \nabla \times \boldsymbol{f}, \tag{2.4}$$

and the transport equation of the strain product $\mathsf{S}^2/2$ (Eq. 2.9). Following Tsinober [2], these events are normally associated with (i) large strain (as outlined above), (ii) high alignment of vorticity with the most extensional eigenstrain $\boldsymbol{\lambda}_1$ (observed below), and (iii) strong tilting of worms (visible in Figure 2.3(b)).

Similarly to many turbulent flows we notice the preferential alignment between $\boldsymbol{\omega}$ and $\boldsymbol{\lambda}_2$, the intermediate eigenvector of the rate-of-strain tensor S, in both turbulent cases. PDF charts of $\cos(\boldsymbol{\omega}, \boldsymbol{\lambda}_i) = (\boldsymbol{\omega} \cdot \boldsymbol{\lambda}_i)/(|\boldsymbol{\omega}||\boldsymbol{\lambda}_i|)$ have been plotted within the bulk in Figure 2.5(a) to manifest the general common feature of the geometrical structure in 3D turbulence. This alignment becomes of notable importance in turbulent dynamics since it contributes to the enstrophy generation term given by $\boldsymbol{\omega} \cdot \boldsymbol{\omega}\mathsf{S} = \boldsymbol{\omega}^2\sigma_i \cos^2(\boldsymbol{\omega}, \boldsymbol{\lambda}_i)$. One of the noteworthy remarks is the high probability observed at $\cos(\boldsymbol{\omega}, \boldsymbol{\lambda}_1) = \pm 1$ for $Ra = 10^{10}$ in comparison with $Ra = 10^8$. It indicates a slightly enhanced alignment between $\boldsymbol{\omega}$ and $\boldsymbol{\lambda}_1$ to follow the self-amplified $-Q_\mathsf{S}$ regions and, therefore, assists the linear contributions of vortex-stretching term. In other words, these self and local strain growing regions at $Ra = 10^{10}$, contribute to local effects associated with (self) interactions of $\boldsymbol{\omega}$ and S [2]. However, we cannot generalize these events (with Ra increment), as many issues, *i.e.* the increased nonlinear enstrophy production, predominant nonlocality and interactions between large and small scales, are essential in vortex-stretching origins. For example, within a frame of forced, homogeneous, isotropic turbulence, Hamlington *et al.* [21] have

reported a preferential alignment of vorticity with the most extensional eigenvector of the *nonlocal* (background) strain. Namely, they decompose the strain rate into its *local* part *i.e.* the self-induced strain field within the vicinity of a typical vortical structure, and its *nonlocal* part, where the strain is essentially induced by all the surrounding other vorticities outside the vortical structure. They found that the vorticity is preferentially aligned with the most extensional background strain rate eigenvector to support the linear contribution to the vortex-stretching dynamics. Hence, this may lead us to the assumption that when the flow is extremely turbulent, the characteristic flow scales get smaller, and the vorticities lay closer and become correlated. As a result, the background-strain $(\boldsymbol{\omega}, \boldsymbol{\lambda}_1)$ alignment arises and combines with the local-based one to eventually yield a general enhancement of *local* interaction $\boldsymbol{\omega}/\mathsf{S}$.

Another important alignment defined by,
$\cos(\boldsymbol{\omega}, \boldsymbol{\omega}\mathsf{S}) = \sigma_i \cos^2(\boldsymbol{\omega}, \boldsymbol{\lambda}_i) / \{\sigma_i^2 \cos^2(\boldsymbol{\omega}, \boldsymbol{\lambda}_i)\}^{1/2}$, is outlined in this study, as a universal feature. Again, it emphasizes on the predominant vortex-stretching action through the bulk, and the net enstrophy production is always positive *i.e.* $\langle \boldsymbol{\omega} \cdot \boldsymbol{\omega}\mathsf{S} \rangle > 0$, in the two turbulent cases. As shown in Figure 2.5(b), both distributions are identically asymmetric and positively-skewed, which probably corresponds to the events associated with strong alignment between vorticity and the intermediate eigenstrain vector $\boldsymbol{\lambda}_2$.

2.2.2 Dynamics of Q_G and R_G invariants

The joint PDFs of $(Q_\mathsf{G}, R_\mathsf{G})$ invariants have provided a statistical picture of the most prevalent distribution for the flow topology and structures, averaged in time and volume. Nonetheless, studying the evolution of Q_G and R_G invariants in a Lagrangian frame allows a dynamical observation of the 3D small-scale turbulence mechanisms, such as the vortex stretching and turbulent kinetic dissipation. Namely, in the frame of a moving observer following a fluid particle, the local surrounding flow structures are essentially described by G and its Galilean invariants, *i.e.* Q_G and R_G. They change in time throughout their lifetime to be finally destroyed in average and leave the large scales of the coherent uniform flow. This change can be interpreted by the Lagrangian dynamics of invariant quantities that were first studied by Cantwell [22]. He deduced the evolution equations for Q_G and R_G and found an analytical solution, but for the inviscid Euler equations. A procedure to investigate the average dynamical behaviour of the invariants was proposed by Martín *et al.* [4] and Ooi *et al.* [5] who used a conditional averaging technique of the invariant rates in DNS of isotropic turbulence. Recalling the deduction by Cantwell [22], firstly, the evolution equation

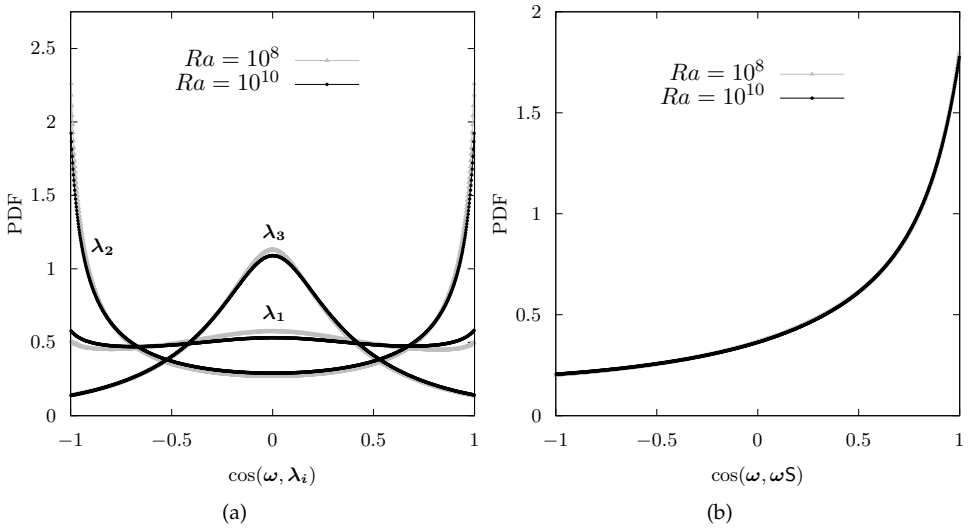

Figure 2.5: PDF of vorticity alignments with the eigenvectors of the rate-of-strain tensor (a) and the vortex-stretching vector $\boldsymbol{\omega}\mathsf{S}$ (b), through the bulk region (V_{bulk}).

of G can be obtained by taking the gradient of NS equations, yielding

$$\frac{D\mathsf{G}}{Dt} + \mathsf{G}^2 = -\mathsf{H}(p) + \sqrt{\frac{Pr}{Ra}}\nabla^2\mathsf{G} + \nabla \boldsymbol{f}, \tag{2.5}$$

where $\mathsf{H}(\phi) = \nabla\nabla\phi$ is the Hessian of a scalar field ϕ. Then, using the definitions of the invariants (Eqs.2.2 and 2.3), the evolution equations of Q_G and R_G read as follows:

$$\frac{DQ_\mathsf{G}}{Dt} = -3R_\mathsf{G} - tr(\mathsf{G}\mathsf{H}_\mathsf{G}) \quad , \qquad \frac{DR_\mathsf{G}}{Dt} = \frac{2}{3}Q_\mathsf{G}^2 - tr(\mathsf{G}^2\mathsf{H}_\mathsf{G}), \tag{2.6}$$

where H_G is a second-order tensor which includes the resultant pressure Hessian, diffusive and the buoyancy terms as follows:

$$\mathsf{H}_\mathsf{G} = -\left(\mathsf{H}(p) - \frac{2Q_\mathsf{G}}{3}\mathsf{I}\right) + \sqrt{\frac{Pr}{Ra}}\nabla^2\mathsf{G} + \nabla \boldsymbol{f}, \tag{2.7}$$

where I is the identity matrix.
The left-hand sides in Eqs.(2.6), *i.e.* DQ_G/Dt and DR_G/Dt, are analysed using an averaging approach identical to Ooi *et al.* [5] and Elsinga and Marusic [6]. Namely, the mean temporal rate of change in the invariants Q_G and R_G is computed from a

set of instantaneous flow fields conditionally upon the invariants themselves. The corresponding approach reads as follows:

$$\left\langle \frac{DQ_G}{Dt} | (Q_G^0, R_G^0) \right\rangle = \left\langle \frac{DQ_G}{Dt} | -\frac{1}{2} \leq \frac{(Q_G - Q_G^0)}{\Delta Q_G} < \frac{1}{2}; -\frac{1}{2} \leq \frac{(R_G - R_G^0)}{\Delta R_G} < \frac{1}{2} \right\rangle,$$
$$\left\langle \frac{DR_G}{Dt} | (Q_G^0, R_G^0) \right\rangle = \left\langle \frac{DR_G}{Dt} | -\frac{1}{2} \leq \frac{(Q_G - Q_G^0)}{\Delta Q_G} < \frac{1}{2}; -\frac{1}{2} \leq \frac{(R_G - R_G^0)}{\Delta R_G} < \frac{1}{2} \right\rangle, \tag{2.8}$$

where (Q_G^0, R_G^0) are the center coordinates of the bin size $(\Delta Q_G, \Delta R_G)$ over which the material derivative is averaged. An imposed bin size 0.05×0.1 in the range $-1 \leq R_G / \langle Q_\Omega \rangle^{3/2} \leq 1$ and $-2 \leq Q_G / \langle Q_\Omega \rangle \leq 2$, respectively in the area of interest, is used. It fulfills a good converging of rates with a robust number of samples (> 500 per bin). The averaged rates are expressed as vectors of two components $(\langle DQ_G/Dt \rangle, \langle DR_G/Dt \rangle)$ and plotted together with their integrated mean trajectories in Figure 2.6 for both *Ra*-number cases through the bulk.

Similarly to isotropic turbulence [4, 5], the trajectories are cyclically decaying towards the origins, moving on average, from regions of higher velocity gradients (small scale motions/fluctuations) to regions of smaller ones (large coherent scales) near the origin. They intrinsically indicate a clockwise spiraling change of the local flow topology around a fluid particle from unstable node saddle/saddle (UN/S/S), stable node saddle/saddle (SN/S/S), stable focus/stretching (SF/S) to unstable focus/compressing (UF/C). A scenario for the mean evolution of fluid particles was given by Ooi *et al.* [5] from that behaviour of the conditional mean trajectories. Namely, within the neighbourhood of coherent focal structure (SF/S), a fluid particle that stands there, in location probably UN/S/S topology $(R_G > 0, D_G < 0)$, will be sucked rapidly into the core of that elongated (intensive enstrophy) structure where the pressure is essentially low. The local topology around the particle changes from UN/S/S via SN/S/S to SF/S. Due to the vortex expansion, the particle travels along the core to regions where those focal structures lose their compact nature (at the ends and bends) by contraction, and the topology becomes UF/C. The compressing actions change the sign of DQ_G/Dt, and reduce the magnitude of invariants to support the decaying events. These events are rendered as an interplay of the non-local pressure Hessian with the viscous diffusion and energy-injecting terms (recent insights about these effects are available for the reader in Wilczek [23], and mainly in the references therein). It attenuates the evolution speed (proportional to the vector length) across the null-discriminant $D_G = (27/4)R_G^2 + Q_G^3 = 0$ curve at $R_G > 0$, and appears in opposite sign with damping effect to DQ_G/Dt and DR_G/Dt in Eqs.(2.6). The developed topology becomes nodal (UN/S/S) and under the dissipative actions, the trajectories

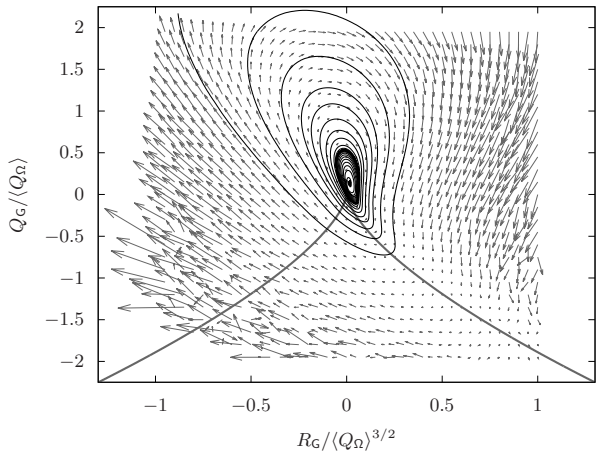

(a)

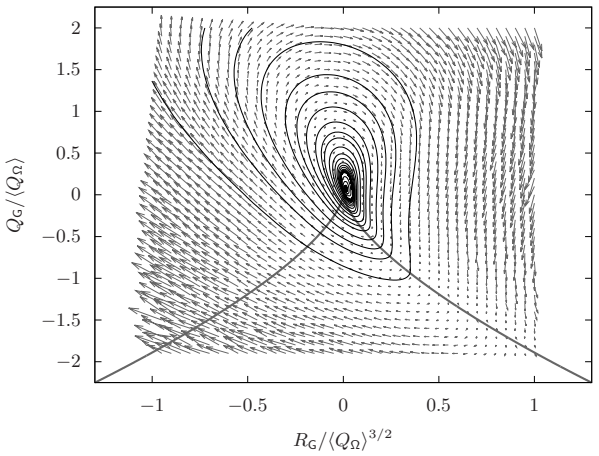

(b)

Figure 2.6: Conditional mean vectors of $\langle DQ_G/Dt \rangle$ and $\langle DR_G/Dt \rangle$ in (Q_G, R_G) plane together with their integral trajectories (black solid orbits) at (a) $Ra = 10^8$ and (b) $Ra = 10^{10}$, through the bulk (V_{bulk}), where the bold solid line indicates $D_G = 0$.

are twisted upwards converging to the origin instead of continuing towards higher values of $R_G > 0$ asymptotic to $D_G = 0$ curve in the case of inviscid Eulerian model $(H_G = 0)$ [22]. Comparing the two scenarios in Figure 2.6, one can note the influence of the local self-amplified velocity gradient (growing $-Q_S$), which is probably in-

duced by the nonlinear advection [22,23]. It contracts the structures further, and bend the trajectories inwards in the area of $D_{\mathsf{G}} > 0$ and $R_{\mathsf{G}} > 0$, at $Ra = 10^{10}$ (Figure 2.6(b)).

Analogously to the previous studies [4–6], the averaged trajectories have revealed that possible periodic spiralling before converging to the origin. The period measurements identified here regarded to one periodic orbit T_0, read $6.7[TU]$ and $4.8[TU]$, correspondingly for $Ra = 10^8$ and 10^{10}, which are suspected to be proportional to the characteristic lifetimes of energy containing eddies released in the bulk. They are found to be close to the periods of the estimated large eddy turnover time $T_0 \sim \tau_{eddy}$ indicating a shorter lifetime of the large coherent eddies in the bulk at the higher Ra-number case. This is not surprising since the large-scale eddies break up under the events associated with the self-amplification of G ($-Q_{\mathsf{S}}$ and Q_{Ω}) at $Ra = 10^{10}$. Broadly speaking, the turbulence type in the core region of RBC is found to be comparable, in statistical aspects, with the isotropic nature. For example, the joint PDF map of $(Q_{\Omega}, -Q_{\mathsf{S}})$ invariants displayed in Figure 2.4(a) presents a similar distribution as the forced isotropic turbulence investigated in Ooi *et al.* [5]. However, the present proportionality T_0 in respect to τ_{eddy}, differs from that outlined by Ooi *et al.* [5], who reported a factor of three times $T_0 \sim 3\tau_{eddy}$. This discrepancy could be returned to the confined configuration of our RBC (adiabatic sidewalls) as well as the mechanism of the thermal plumes in injecting the kinetic energy to the large-scale eddies. Indeed, the measured periods T_0 can be compared to the average plume lifetime τ_{pl} with almost three times factor $T_0 \sim 3\tau_{pl}$. Here, $\tau_{pl} \sim \delta_T^2\sqrt{RaPr}$ is defined as the plume lifetime through which it detaches with the thickness of the thermal BL δ_T, and loses its temperature contrast by the thermal diffusivity $1/\sqrt{RaPr}$ [24]. Following this approach, the determined average plume lifetimes in the current configurations read $\tau_{pl} \sim 2.190[TU]$ and $1.276[TU]$ for $Ra = 10^8$ and 10^{10}, respectively. These findings accordingly suggest the participation of the thermal plumes in the large-scale kinetic energy containing eddies and turbulent wind, especially when the plumes (mushroom-like) elongate importantly in the bulk before scattering. However, in a hard turbulent state at high Ra number such as 10^{10}, the role of plumes is outstandingly reduced due to the extreme fluctuations and the good mixing. Consequently, the role of the self-amplified $-Q_{\mathsf{S}}$ in creating the large-scale eddies in the bulk is enlarged. This could be the reason why the measured period T_0 exceeds somewhat the $3\tau_{pl}$, which confirms the prevalence of the self-amplified velocity derivatives by turbulence over the buoyant mechanisms.

2.2.3 Dynamics of R_{S} and $tr(\Omega^2\mathsf{S})$ nonlinearities

In order to elucidate the impact of the local self-amplification of G (at least at high Ra numbers) more, the dynamics of the physically meaningful third-moment nonlin-

earities described by the enstrophy production $R_S - R_G = tr(\Omega^2 S)$, and the quantity R_S (as a contribution of the straining production) have been studied. They both constitute the production term of the strain product $S^2/2 \sim -Q_S$ inside the transport equation, which reads as follows:

$$\frac{DQ_S}{Dt} = -3R_S + tr(\Omega^2 S) - tr(SH_S), \tag{2.9}$$

with

$$H_S = -\left(H(p) - \frac{2Q_G}{3}I\right) + \sqrt{\frac{Pr}{Ra}}\nabla^2 S + 1/2(\nabla \boldsymbol{f} + \nabla \boldsymbol{f}^t). \tag{2.10}$$

In the frame of an isotropic turbulence, statistical analysis of these nonlinearities, as the joint PDF $(R_S - R_G, R_S)$, was earlier performed by Kholmyansky *et al.* [25]. It revealed that the two such nonlinearities, namely, enstrophy and strain productions, are locally different and only weakly correlated. Others like Lüthi *et al.* [26], again for isotropic turbulence, have stressed on the importance of these nonlinearities by studying the evolution of the small scale motions in a 3D phase space $\{Q_G, R_S, R_S - R_G\}$.

In this work and in the bounds of V_{bulk}, the joint PDFs of $(R_S - R_G, R_S)$ are plotted in Figure 2.7 for both turbulent cases. The two invariant-based terms are normalized by $\langle Q_\Omega \rangle^{3/2}$, differently than in [25] where therein, the mean values $\langle R_S - R_G \rangle$ and $\langle R_S \rangle$ are respectively used for $R_S - R_G$ and R_S. In consistency with Kholmyansky *et*

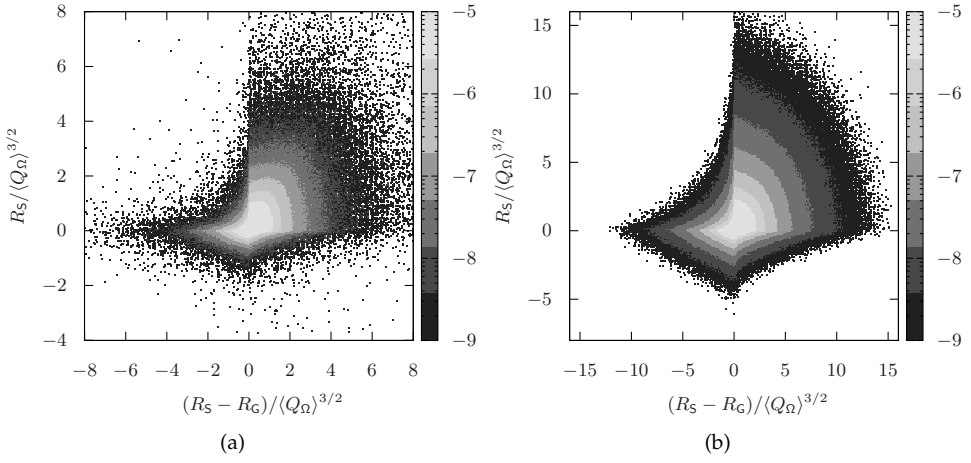

(a) (b)

Figure 2.7: Joint PDF of normalized $R_S - R_G$ and R_S invariants on logarithmic scale at (a) $Ra = 10^8$ and (b) $Ra = 10^{10}$ through the bulk (V_{bulk}).

al. [25], the two plots have shown a similar weak correlation locally of the two nonlinearities, but with different behaviour in the positive part of both. They reveal the presence of many points with large positive values of both nonlinearities, slightly shifted toward $R_S > 0$. Comparing the two charts in Figures 2.7(a) and 2.7(b), one can note the enhanced tendency of the distribution at $Ra = 10^{10}$ to be more linear with balanced nonlinearities in regions of vortex stretching and positive strain production. This can imply an enhanced localization to the nonlinearities in the regions dominated by the self-amplified strain, which corresponds to the observations outlined in § 2.2.1. Namely, at $Ra = 10^{10}$, a local self-amplification of G ($-Q_S$ and Q_Ω in concomitant) takes place and produces simultaneously an increase in the nonlinearity of vortex stretching (in slots of S [2]) with enhanced local interactions of vorticity/strain.

Following an identical procedure to $(DQ_G/Dt, DR_G/Dt)$ in the previous Section, the conditional mean trajectories of $(D(R_S - R_G)/Dt, DR_S/Dt)$ have been plotted in Figure 2.8 for both turbulent cases in the bulk. As can be seen, the two mean dynamics show a zero starting point since with no straining, no enstrophy will evolve and vice versa [2]. The trajectories start moving towards negative values of enstrophy production to emphasize always on the collaborated role between the vortex compression structures and the strain generation. When $R_S > 0$ the vectors suddenly change their signs to travel upwards with a notably enhanced linear evolution at $Ra = 10^{10}$ (see Figure 2.8(b)). The directional change can be returned to the opposite sign of these quantities in the production term of the strain rate $-Q_S$, inside Eq.(2.9). In agreement with the previous notes, the self-amplified viscous strain $-Q_S$ at the higher Ra number is apparently recognized through further contraction of vorticities $(R_S - R_G < 0)$ and growing strain regions $(R_S > 0)$, which is revealed in higher linear and organized act of trajectories in that zones. This confirms again the direct and local assistance of vortex compression to the dissipative actions and energy cascade [2] (in a hard turbulence case). Afterwards, once the evolution enters the stretching area $(R_S - R_G > 0)$, a sharp decay towards the small values of R_S takes place at $Ra = 10^8$ (Figure 2.8(a)). This displacement could be returned to the nonlocality effect since we are in the centered vorticity tube-like filaments/worms. However, at the higher Ra number the trajectories tend to move more softly indicating the improved localization of nonlinearities in those areas. It is sustained by strong linear interactions in regions of ($R_S > 0$ and $R_S - R_G < 0$), which in turn make a positive contribution to the magnitude of the vortex-stretching vector $\boldsymbol{\omega}$S [2]. Finally, the mean trajectories spiral inwards converging in part towards the origin. They tend to either return to the starting point close to the origin, or change their direction to higher values across $R_S < 0$ and $R_S - R_G > 0$, again, with higher linearity at $Ra = 10^{10}$. It is important to note the positive end (origin) of $(\langle D(R_S - R_G)/Dt\rangle, \langle DR_S/Dt\rangle)$, which asserts the predominance of vortex stretching $(\langle \boldsymbol{\omega} \cdot \boldsymbol{\omega}\mathsf{S}\rangle > 0)$, and the concomitant

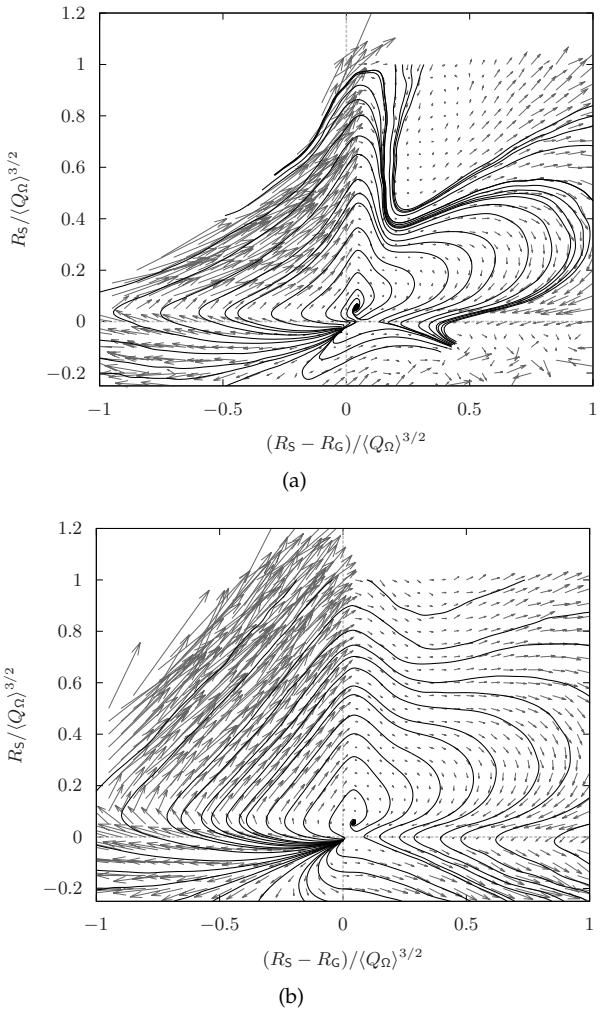

Figure 2.8: Conditional mean vectors of $\langle DR_S/Dt \rangle$ and $\langle D(R_S - R_G)/Dt \rangle$ in $(R_S, R_S - R_G)$ plane together with their integral trajectories (black solid lines) at (a) $Ra = 10^8$ and (b) $Ra = 10^{10}$, in the bulk (V_{bulk}).

predominant self-amplification of viscous strain/dissipation production $(R_S > 0)$, generally happening in 3D turbulence [2].

2.3 Invariants of $\nabla(\boldsymbol{u}T)$ tensor

Hereafter we consider the gradient of velocity multiplied by temperature tensor $\mathsf{G}_\theta = \nabla(\boldsymbol{u}T)$, which couples the kinetic and thermal small scales of motions. Notice that $\boldsymbol{u}$ and T are defined in such a way that $\int_\Omega \boldsymbol{u} d\Omega = 0$ and $\int_\Omega \langle T \rangle d\Omega = 0$. This tensor contributes to the turbulent heat flux and buoyant production, given as $\langle w'T' \rangle$, which is found to be directly associated with the evolution of thermal plumes [27]. On the other hand, its invariants (such as the magnitude $|\mathsf{G}_\theta| = (\mathsf{G}_\theta \colon \mathsf{G}_\theta)^{1/2}$) address in some sense, strong interactions of kinetic and thermal dissipation rates. Namely, $\mathsf{G}_\theta = T\mathsf{G} + \boldsymbol{u} \otimes \nabla T$, when T is constant, yields to $\mathsf{G}_\theta \sim \mathsf{G}$ and hence, $|\mathsf{G}_\theta|^2 \sim |\mathsf{G}|^2 = |\Omega|^2 + |\mathsf{S}|^2$. The strain part therein, is proportional to the local viscous dissipation ϵ, as $|\mathsf{S}|^2 = \mathsf{S} \colon \mathsf{S} = tr(\mathsf{S}^2) = 1/2(Pr/Ra)^{-1/2}\epsilon$. On the other hand, when $|\boldsymbol{u}| = 1$, the l^2-norm of G_θ is proportional to the thermal dissipation rate ϵ_T, *i.e.* $|\mathsf{G}_\theta|^2 = |\nabla T|^2 = (RaPr)^{1/2}\epsilon_T$. Moreover, the viscous and thermal dissipation rates are found to be locally interacted in the regions of thermal plumes, in particular when they exceed their mean values, as outlined in § 1.3.2. Consequently, it seems appropriate to utilize the tensor G_θ in order to investigate that important mechanism of turbulent heat transport (plumes) in a small scale point-of-view. To do so, we analyse the fine-scale dynamics deeply coupled with the evolution of the thermal plumes by considering a similar approach as for the classical tensor G, applied on the basic invariants of the traceless part of the new tensor, meaning $\tilde{\mathsf{G}}_\theta = \mathsf{G}_\theta - 1/3tr(\mathsf{G}_\theta)\mathsf{I}$. This can permit the analysing of the tensor characteristics identically to the G tensor.

As a starting point, we introduce the evolution equation for $\boldsymbol{u}T$ that follows from the NS and the energy equations (Eqs.1.2 and 1.3) through the formula $D(\boldsymbol{u}T)/Dt = \boldsymbol{u}DT/Dt + TD\boldsymbol{u}/Dt$, as:

$$\frac{D(\boldsymbol{u}T)}{Dt} = T(\boldsymbol{f} - \nabla p) + \sqrt{\frac{Pr}{Ra}} T\nabla^2\boldsymbol{u} + \frac{1}{\sqrt{RaPr}}\boldsymbol{u}\nabla^2 T. \tag{2.11}$$

At this point, the essential ideas behind this equation can be conveyed more easily by assuming that $Pr = 1$. In this case, the evolution equation reads

$$\frac{D(\boldsymbol{u}T)}{Dt} = T(\boldsymbol{f} - \nabla p) + \frac{1}{\sqrt{Ra}}\Big(\nabla^2(\boldsymbol{u}T) - 2\nabla\boldsymbol{u} \cdot \nabla T\Big). \tag{2.12}$$

Similarly to the kinetic energy transport equation $|\boldsymbol{u}|^2/2$, the evolution equation of $e_T = |\boldsymbol{u}T|^2/2$ is introduced as follows:

$$\frac{De_T}{Dt} = \boldsymbol{u}T^2 \cdot (\boldsymbol{f} - \nabla p) + \frac{1}{\sqrt{Ra}}\Big(\nabla^2 e_T - \nabla(\boldsymbol{u}T) \colon \nabla(\boldsymbol{u}T) - 2\boldsymbol{u}T \cdot \nabla\boldsymbol{u} \cdot \nabla T\Big). \tag{2.13}$$

Notice that the l^2-norm of G_θ contributes to the diffusive term of e_T evolution equation, *i.e.* $\nabla(\boldsymbol{u}T)\colon\nabla(\boldsymbol{u}T) = \mathsf{G}_\theta\colon\mathsf{G}_\theta = |\mathsf{G}_\theta|^2$. This characterizes the action of thermal plumes in dissipating the heat flux and feeding the momentum. In other words,

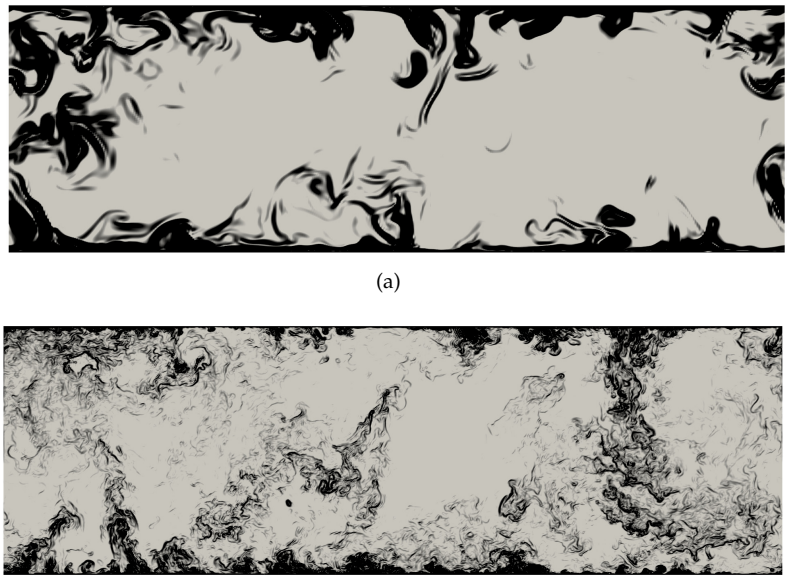

(a)

(b)

Figure 2.9: Visualization of the thermal plumes (black color) in (x, z) plane, indicated by high values of $|\tilde{\mathsf{G}}_\theta|$, past specific thresholds read $|\tilde{\mathsf{G}}_\theta| > 0.214$ for $Ra = 10^8$ in (a) and $|\tilde{\mathsf{G}}_\theta| > 0.154$ for $Ra = 10^{10}$ in (b). (See movies of plumes separation [http://dx.doi.org/10.1063/1.4967495.2]).

high values of $|\mathsf{G}_\theta|$ differentiate zones of high gradient heat flux from the rest of the flow, which are deeply related with the presence of the thermal plumes. Following a determined threshold of $|\tilde{\mathsf{G}}_\theta|$, a separation criterion of the thermal plumes from the turbulent background regions (rest of the flow), can be proposed. It corresponds to the most probable heat flux dissipation, *i.e.* the value of $|\mathsf{G}_\theta|$ at which the PDF is maximal, as a consequent value of the mixing activity (the most widespread). Larger values beyond that threshold disclose deep thermal-kinetic interactions, and hence the thermal plumes, while smaller values correspond to the turbulent background, as visually clear in Figure 2.9.

The invariant $Q_{\tilde{\mathsf{G}}_\theta} = -1/2tr(\tilde{\mathsf{G}}_\theta^2)$, has a similar meaning as $|\tilde{\mathsf{G}}_\theta|$ in describing the intensity of gradient heat flux. It visualizes the (fine-scale) structures associated with

high kinetic-thermal interactions. Its highest positive and negative values indicate the relevant thermal structures, while the near zero ones correspond to the turbulent background and well-mixing zones. As shown in Figure 2.10(a), one can observe how

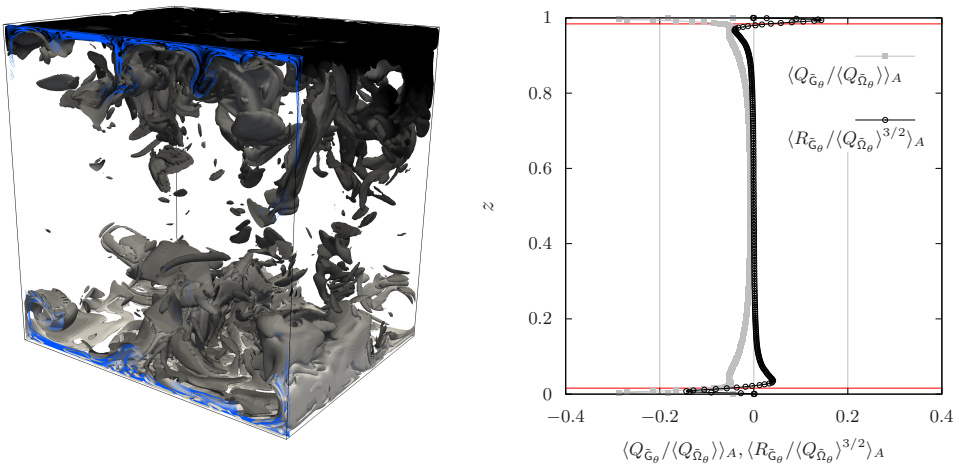

(a) (b)

Figure 2.10: (a) structures of high positive and negative values of $Q_{\tilde{G}_\theta}$ ($-0.7143 > Q_{\tilde{G}_\theta} > 0.7143$) figured through a portion of the domain at $Ra = 10^8$, (See movies of their dynamics [http://dx.doi.org/10.1063/1.4967495.3]) where the blue contours indicate the hot and cold plumes. (b) represents the averaged temporal and spatial (x-y) profiles of normalized invariants $Q_{\tilde{G}_\theta}$ and $R_{\tilde{G}_\theta}$ along the z distance, where the solid red lines refer to δ_T

.

the $Q_{\tilde{G}_\theta}$ structurally features the evolution of thermal plumes beyond positive and negative thresholds. Similarly $R_{\tilde{G}_\theta} = -1/3tr(\tilde{G}_\theta^3)$, is introduced as a third moment of concentrated kinetic-thermal small scale interactions. It nearly obeys a similar distribution to the skewness profile of the temperature fluctuation, showed before in Figure 1.6(b), and similarly calculated by Emran and Schumacher [28], as shown in Figure 2.10(b). Therein, the profiles of $\langle Q_{\tilde{G}_\theta}/\langle Q_{\tilde{\Omega}_\theta}\rangle\rangle_A$ and $\langle R_{\tilde{G}_\theta}/\langle Q_{\tilde{\Omega}_\theta}\rangle^{3/2}\rangle_A$ have been plotted in the lower turbulent case, since the better determination of thermals always belongs to $Ra = 10^8$ in this study. Briefly speaking from Figure 2.10(b), the two profiles of invariants start from zero value at the isothermal walls towards negative averaged values of $Q_{\tilde{G}_\theta}$ within the thermal BLs. However, $R_{\tilde{G}_\theta}$ tends to have negative and positive values through the BLs in correspondence with the moving up and down thermals (plumes). Afterwards, in the bulk both mean invariants hold a zero value

due to the mixing action and plumes diffusion.

2.3.1 Joint PDF of invariants $Q_{\tilde{\mathsf{G}}_\theta}$ and $R_{\tilde{\mathsf{G}}_\theta}$

Likewise in the classical tensor, the qualitative properties of the new invariants $Q_{\tilde{\mathsf{G}}_\theta}$ and $R_{\tilde{\mathsf{G}}_\theta}$ are investigated by means of plotting their joint PDF, as represented in Figure 2.11. The statistical analysis therein is similar to the classical-based one reported in Figure 2.2, except that the studied regime is extended broadly to cover all the domain in order to include the vicinities of emanating thermals. Interestingly, the general aspect shown in Figures 2.11(a) and 2.11(b) tends to be symmetric respect to $R_{\tilde{\mathsf{G}}_\theta} = 0$. Thereby, it seems to follow the statistical characteristics of the thermal plumes since various studies have revealed the log-normal statistics as a universal distribution for the thermal plumes geometries. For example, Zhou and Xia [29] showed that the sizes of the mushroom-like plumes obey log-normal statistics. Likewise, the geometric measures of the sheet-like plumes such as its normalized area, length and width, its aspect ratio and the shape complexity [30], as well the heat content [31], are all log-normally distributed.
From observing the statistics in Figure 2.11, one can note how the distributions in both cases obey an arrangement similar to the isolines of discriminant $D_{\tilde{\mathsf{G}}_\theta} = (27/4)R^2_{\tilde{\mathsf{G}}_\theta} + Q^3_{\tilde{\mathsf{G}}_\theta}$, drawn in the $(Q_{\tilde{\mathsf{G}}_\theta}, R_{\tilde{\mathsf{G}}_\theta})$ space (Figure 2.11(c)). By definition, the discriminant holds a similar significance as $Q_{\tilde{\mathsf{G}}_\theta}$ and $R_{\tilde{\mathsf{G}}_\theta}$ invariants, since it formulates their combination to follow identically the regions tightly associated with the thermal plumes. Particularly in the hard turbulent state (Figure 2.11(b)), when the plumes are evolving in many scaled-down fragments, the statistics shows a clear following to $D_{\tilde{\mathsf{G}}_\theta}$-isolines due to the extensive amount of plumes generated. In a general description, both cases share the aspect that most of the flow is occupied by well-mixed areas (turbulent background) of very low $(Q_{\tilde{\mathsf{G}}_\theta}, R_{\tilde{\mathsf{G}}_\theta})$ values near the origin, while the thermal plumes take high values (negative and positive) of invariants far from the origin. The plumes at $Ra = 10^8$ are identified in relatively large geometries, emanate few and elongate significantly into the bulk (mushroom-like) before scattering. Therefore, the points in Figure 2.11(a) become more dispersed to take relatively high values of $(Q_{\tilde{\mathsf{G}}_\theta}, R_{\tilde{\mathsf{G}}_\theta})$. They compose a joint PDF feature which seems to be almost similar to the one based on a Gaussian flow field (see Tsinober [2] Figure 9.1(f) as an example of joint PDF of $(Q_{\mathsf{G}}, R_{\mathsf{G}})$ for a Gaussian velocity field). However, in the hard turbulent state, the plumes are abundantly emitted in the BLs, and rapidly destroyed in the bulk to make the points closely located next to the origin, holding moderate values of $(Q_{\mathsf{G}}, R_{\mathsf{G}})$ (Figure 2.11(b)). Since the mean profile of $Q_{\tilde{\mathsf{G}}_\theta}$, displayed in Figure 2.10(b), appears to be negatively shifted inside the thermal BLs, it

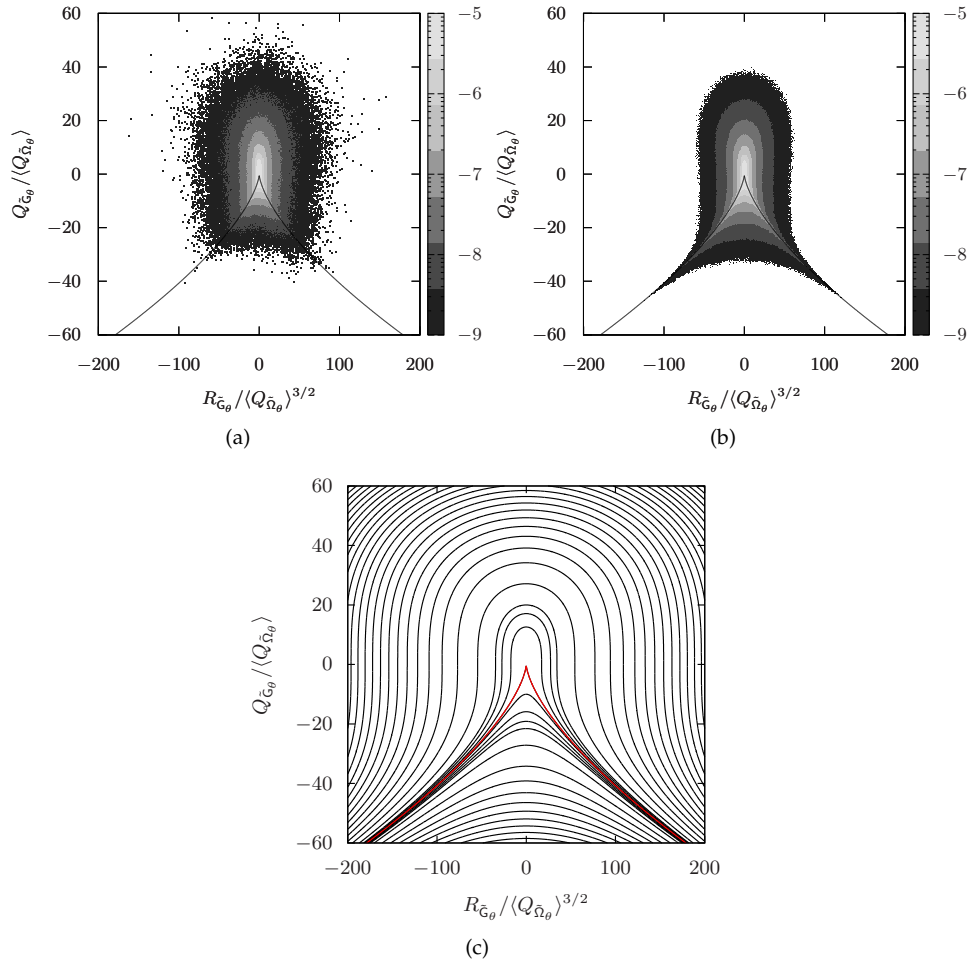

Figure 2.11: Joint PDF of normalized $Q_{\tilde{G}_\theta}$ and $R_{\tilde{G}_\theta}$ on logarithmic scale at (a) $Ra = 10^8$ and (b) $Ra = 10^{10}$, in the whole domain. (c) displays the representative isolines of the discriminant $D_{\tilde{G}_\theta} = (27/4)R^2_{\tilde{G}_\theta} + Q^3_{\tilde{G}_\theta}$ in the invariants space, where the solid tent-black line in (a), (b) and the red identical one in (c), is $D_{\tilde{G}_\theta} = 0$.

suggests that most of the plumes (sheet-like) or the deep kinetic-thermal interactions therein, are indicated by $Q_{\tilde{G}_\theta} < 0$ values. Hence, many more points are placed down under the line $D_{\tilde{G}_\theta} = 0$ in Figure 2.11(b) (than in 2.11(a)), to correspond probably with

the abundant thermals/small-scale interactions emanating in the BLs at $Ra = 10^{10}$.

2.3.2 Dynamics of $Q_{\tilde{\mathsf{G}}_\theta}$ and $R_{\tilde{\mathsf{G}}_\theta}$ invariants

An analysis of the dynamics of $Q_{\tilde{\mathsf{G}}_\theta}$ and $R_{\tilde{\mathsf{G}}_\theta}$ invariants, similar to the classical-based one, is considered hereafter. Firstly, the evolution equation of G_θ can be obtained easily by differentiating Eq.(2.12) (for such a simplified formulae considering $Pr = 1$) as follows:

$$\frac{D\mathsf{G}_\theta}{Dt} + \mathsf{G}\mathsf{G}_\theta = -\nabla T \otimes \nabla p - T\mathsf{H}(p) + 2\boldsymbol{f} \otimes \nabla T + \frac{1}{\sqrt{Ra}}\Big(\nabla^2 \mathsf{G}_\theta - 2\nabla \mathsf{G} \cdot \nabla T - 2\mathsf{G}\mathsf{H}(T)\Big). \tag{2.14}$$

Afterwards, the mean temporal rates of change in invariants $Q_{\tilde{\mathsf{G}}_\theta}$ and $R_{\tilde{\mathsf{G}}_\theta}$ have been studied in the same manner as in § 2.2.2. They aid to elucidate the scenarios and lifetimes of the kinetic-thermal small scale motions indicating mainly the presence of the thermal plumes, their survival and their continuous mean changing under the dissipative actions. To do so, the averaging approach described in Eqs.(2.8) is used pertaining the new invariants $\langle DQ_{\tilde{\mathsf{G}}_\theta}/Dt\rangle$, $\langle DR_{\tilde{\mathsf{G}}_\theta}/Dt\rangle$, and the resultant vectors are presented together with their integral trajectories within the total domain in Figure 2.12. The bin size is imposed identically to obtain a division of 40×40 for the corresponding ranges of $R_{\tilde{\mathsf{G}}_\theta}/\langle Q_{\tilde{\Omega}_\theta}\rangle^{3/2}$ and $Q_{\tilde{\mathsf{G}}_\theta}/\langle Q_{\tilde{\Omega}_\theta}\rangle$, which sufficiently fulfills the convergence of the rates.

According to Figure 2.12, our analysis starts from the fact that the trajectories are born from zero valued $(Q_{\tilde{\mathsf{G}}_\theta}, R_{\tilde{\mathsf{G}}_\theta})$ at the isothermal walls, and move down towards the negative values of $Q_{\tilde{\mathsf{G}}_\theta}$ in correspondence with the generation of the sheet-like plumes or the roots of the original mushroom-like plumes (see Figure 2.13(b)). These roots are generated within the thermal BLs under the impact of the surrounding interaction areas, *i.e.* the impingement of the mixed flow coming from the bulk and the opposite-side plumes which reach to the BL and collide the wall therein. They excite the creation of horizontal waves (also provoked by shear strain) that travel in the BL, and interact with each other to compose the sheet-like plumes (roots). These sheet-like rods convolute and swirl away by buoyancy to arise into the bulk as the mushroom-like plumes. The areas of interactions around the roots are mostly addressed by positive values of $Q_{\tilde{\mathsf{G}}_\theta}$, as can be seen in Figure 2.13(b). More evidence of this can be taken from the behaviour of the mean trajectories within the thermal BLs, represented in Figure 2.13(a). Therein, the averaged evolution starts from zero to swirl downwards to $Q_{\tilde{\mathsf{G}}_\theta} < 0$ from $R_{\tilde{\mathsf{G}}_\theta} > 0$ to $R_{\tilde{\mathsf{G}}_\theta} < 0$ in the hot BL, and conversely in the cold one. This action accordingly validates the behaviour of $Q_{\tilde{\mathsf{G}}_\theta}$ and $R_{\tilde{\mathsf{G}}_\theta}$ mean profiles showed in Figure 2.10(b) to emphasize correctly on their aforementioned

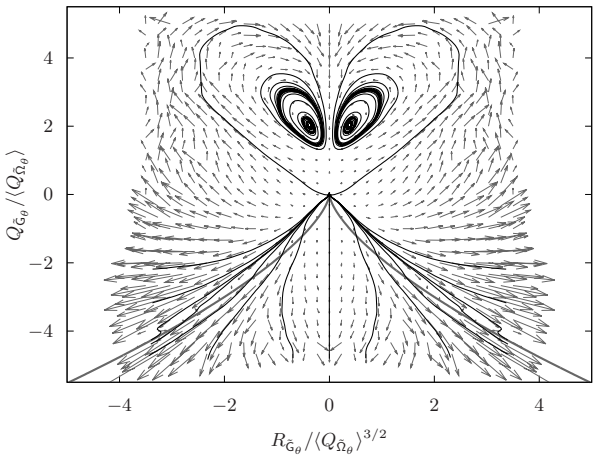

(a)

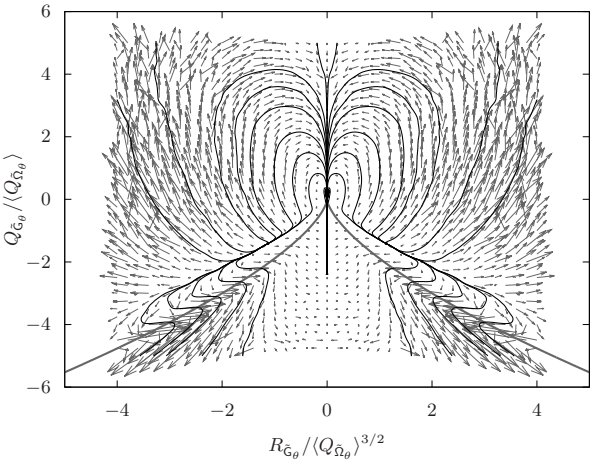

(b)

Figure 2.12: Conditional mean vectors of $\langle DQ_{\tilde{G}_\theta}/Dt\rangle, \langle DR_{\tilde{G}_\theta}/Dt\rangle$ in $(Q_{\tilde{G}_\theta}, R_{\tilde{G}_\theta})$ plane together with their integral trajectories (black solid orbits) at (a) $Ra = 10^8$ and (b) $Ra = 10^{10}$, through the total domain, where the bold solid line indicates $D_{\tilde{G}_\theta} = 0$.

meanings.

Going back to Figure 2.12 and along the downward path, the mean rates of invariants are slowing down with directional change at crossing the null-discriminant curve to later continue moving separately upwards away or downwards asymptotically parallel to the null-discriminant curve. This slowdown could be returned to the fact that no plumes formulation exists in that zone as $D_{\tilde{\mathsf{G}}_\theta}$ analogously follows the evolution of plumes. However, from a physical point of view, it can give us an impression that the curve of null-discriminant can separate the sheet-like plumes evolution that moves downwards, from the evolution of the arisen mushroom-like plumes which moves upwards. The phenomenon of the directional change in the harder turbulent state is so remarkable because of the extreme emanating plumes in general, and many provoked sheet-like plumes attend to favourable fluctuations and intermittency within the BL.

All the trajectories tend to move rapidly towards high positive and negative values of $(Q_{\tilde{\mathsf{G}}_\theta}, R_{\tilde{\mathsf{G}}_\theta})$, to eventually address the fine-scale relevant dynamics of thermal plumes. Above the curve $D_{\tilde{\mathsf{G}}_\theta} = 0$, the trajectories reveal an upward spiraling behaviour before converging towards two skew-symmetric origins in respect to $R_{\tilde{\mathsf{G}}_\theta} = 0$ (mostly referring to the hot and cold thermals) at $Ra = 10^8$ (see Figure 2.12(a)). The trajectories near origins probably indicate the mean evolution and lifecycle of the mushroom-like thermal plumes that elongate far from the thermal BLs and contribute predominately to the coherent large scales of heat flux. By measuring the period of one periodic orbit around the origin (the bigger orbits), we see that it follows the lifetime of plumes $\tilde{T}_0 = 6.56 \sim 3\tau_{pl} = 6.58[TU]$, since the plumes travel mostly in groups near the lateral sidewalls and organize to the large-scale circulation therebeside.
In the hard turbulent state addressed in Figure 2.12(b), the spiraling trajectories seem to travel upwards in shorter tracks (than in $Ra = 10^8$) to show the reduced lifetime of the mushroom-like plumes under the dissipative and mixing effects. The flow regime, at $Ra = 10^{10}$, is essentially characterized by high perturbations and a noteworthy local self-amplification of velocity derivatives $-Q_{\mathsf{S}}$. The plumes are abundantly emitted in the BLs as scaled-down fragments. They scatter effectively under the impact of the amplified mixing $(-Q_{\mathsf{S}})$ to eventually make the trajectories converging towards a zero-valued origin (Figure 2.12(b)). This accordingly, suggests that the thermal plumes, at the high Ra number, do not contribute to the mean large scales of heat flux, and just give them a life. This in turn, is not so strange since experiments and DNS indicate that the large scale circulation decreases with increasing the Ra which can be attributed to the decreasing fragmentation of the plumes [27].

In order to give a broader picture, the mean rate trajectories of $Q_{\tilde{\mathsf{G}}_\theta}$ and $R_{\tilde{\mathsf{G}}_\theta}$ invariants are plotted similarly, through the bulk region (V_{bulk}) in Figure 2.14(a). Therein, all the trajectories obey generally an upward moving action decaying towards

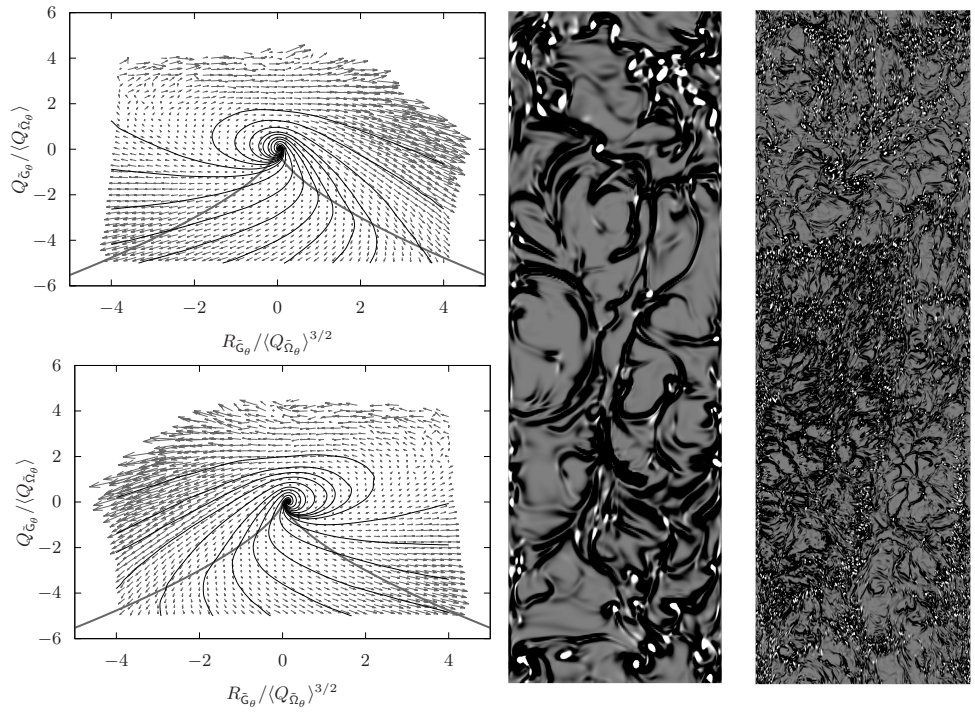

Figure 2.13: (a) represents the same approach as displayed in Figure 2.12, but calculated within the thermal hot (top) and cold (bottom) boundary layers at $Ra = 10^{10}$. (b) shows horizontal (x, y) planes of high positive (white) and negative (black) values of $Q_{\tilde{\mathsf{G}}_\theta}$ extracted at the hot thermal BL levels $z = 0.016$ for $Ra = 10^8$ (left), and $z = 0.004$ for $Ra = 10^{10}$ (right).

a zero-valued origins for both Ra numbers. Below the $D_{\tilde{\mathsf{G}}_\theta} = 0$ curve, the mean rate tracks are moving up indicating the extended parts of the original plumes in the bulk. Likewise, above the null-discriminant curve the tracks are upwarded in spiraling behaviour to address the elongating action of the mushroom-like plumes, and the subsequent scattering by the dissipative mixing (see Figure 2.14(b)). It can be an interesting point observing the upward direction behaviour of the tracks in region of $Q_{\tilde{\mathsf{G}}_\theta} < 0$ through the bulk, whereas they were downwarded in the whole domain (Figure 2.12). This manifests the fact that two evolutions of plumes exist: the sheet-like

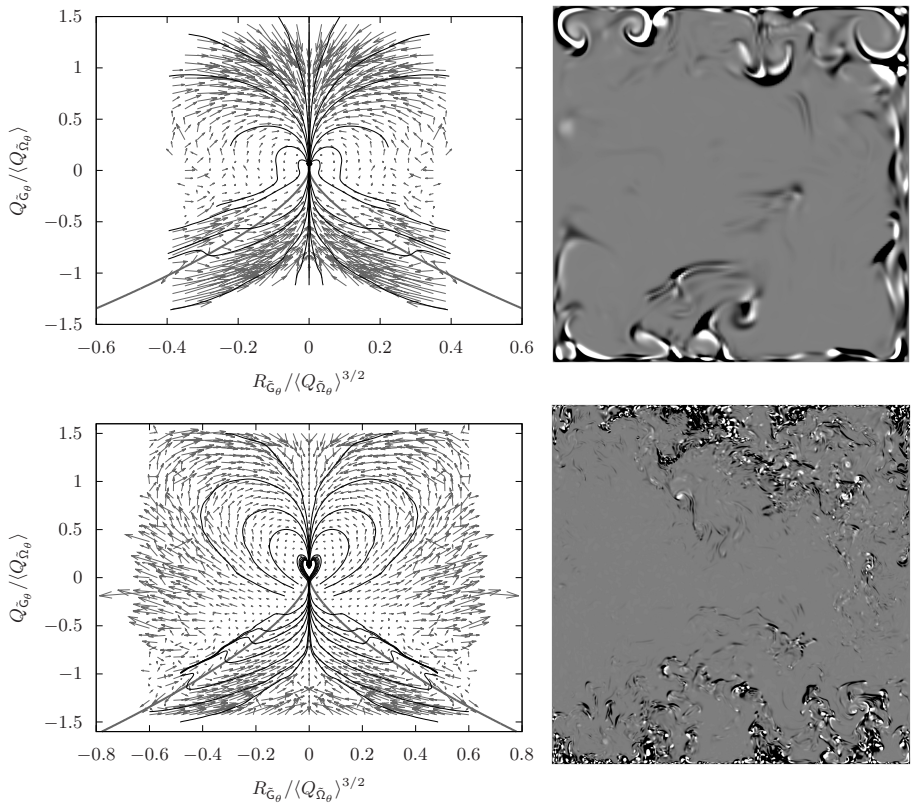

Figure 2.14: (a) the same representations as Figure 2.12, but through the bulk region (V_{bulk}), for $Ra = 10^8$ (top) and $Ra = 10^{10}$ (bottom). (b) displays vertical planes (y, z) of $Q_{\tilde{\mathsf{G}}_\theta}$ coloured similarly to Figure 2.13(b), for $Ra = 10^8$ (top) and $Ra = 10^{10}$ (bottom).

ones or the original roots that emanate in the BLs, and the the mushroom-like ones, which travel and expand in the bulk. It is also worthwhile noting that the trajectories swirl with longer and wider tracks above the $D_{\tilde{\mathsf{G}}_\theta} = 0$ curve in Figure 2.14 (bottom) (than in Figure 2.14 (top)). This can be classified as a natural result of increasing the rate of plumes production, injected forwards in the bulk, at $Ra = 10^{10}$. Finally, in both cases, all the trajectories seem to converge towards zero-value origins due to the effective mixing activities in the bulk, keeping in mind that V_{bulk} is quite far of

including the solid wall influences. The plumes are destroyed in mean, absolutely at a constant averaged heat flux across the bulk, and yielding naturally to a zero-gradient heat flux and null means for $Q_{\tilde{\mathsf{G}}_\theta}$ and $R_{\tilde{\mathsf{G}}_\theta}$ (see Figure 2.10(b)).

2.4 Conclusions

Several universal small-scale features observed in various turbulent flows have been recaptured in buoyancy-driven turbulent RBC. The common inclined "teardrop" shape of the joint PDF statistics of the classical invariants $(Q_\mathsf{G}, R_\mathsf{G})$ through the bulk region are observed. Furthermore, the mean temporal rate of invariants change $(\langle DQ_\mathsf{G}/Dt\rangle, \langle DR_\mathsf{G}/Dt\rangle)$ is plotted in that region to reveal the common spiralling clockwise behaviour of trajectories converging towards the origin. In consistency with previous studies on the small-scale motions (Ooi *et al.* [5] and Elsinga and Marusic [6]), the topology surrounding a fluid particle is varying in a cyclical aspect, in the $(Q_\mathsf{G}, R_\mathsf{G})$ space, from unstable focus, unstable node, stable node to stable focus structures in the both cases. A local self-amplification of velocity derivatives (viscous straining $-Q_\mathsf{S}$ in the turbulent background) at $Ra = 10^{10}$, aids in contracting the vorticity worms further which assists the decaying events (interplay of the non-local pressure Hessian with the viscous diffusion and energy-injecting terms), and bends the trajectories inwards above the null-discriminant curve. The one period of the periodic spiral orbits near the origin is found to approach $T_0 \sim \tau_{eddy}$ an estimated large eddy turnover time defined in the bulk. On the other hand, the measured period has been compared with the average plume lifetime $T_0 \sim 3\tau_{pl}$ to suggest the participation of the thermal plumes in the large-scale kinetic energy containing eddies and turbulent wind created in the bulk; particularly when the plumes elongate significantly before scattering, at $Ra = 10^8$. Other universal features of (small scale) 3D turbulence are observed through the bulk region. For example, the preferential alignment between $\boldsymbol{\omega}$ and $\boldsymbol{\lambda}_2$ the intermediate eigenstrain vector, and the asymmetric $\boldsymbol{\omega}$ alignment with the vortex-stretching vector. The local self-amplification of velocity derivatives $(-Q_\mathsf{S}/Q_\Omega)$ at $Ra = 10^{10}$ has revealed enhanced local effects associated with (self) interactions of vorticity/strain in the strain dominated regions and thus, improve slightly the linear contributions of the vortex stretching mechanism.

On the other hand, the evolution of relevant thermals has been addressed in small scale point-of-views. Namely, considering the invariants of the traceless part of velocity-times-temperature gradient tensor $(Q_{\tilde{\mathsf{G}}_\theta}, R_{\tilde{\mathsf{G}}_\theta})$, an identical approach of studying their mean temporal rate and joint PDF, has been applied. The new invariants have demonstrated a direct picture on the small-scale kinetic and thermal interaction dynamics. They have expressed a correct following to the evolution of thermal plumes in RBC. It is found that the conditional averaged trajectories travel

downwards to expose the sheet-like plumes dynamics (roots) within the BLs, and upwards to exhibit the mushroom-like plumes evolution that expand in the bulk. The trajectories –through the total domain– spiral upwards before converging towards two skew-symmetric origins with periodic orbits correspond in their period to approximately 3 times the lifetime of plumes at $Ra = 10^8$. By that end, it was emphasized on the predominant role of hot and cold plumes in contributing to the coherent large scales of heat flux, in average, which roll near the lateral sidewalls. Shorter tracks of the trajectories have been recorded at the higher *Ra* number (in the whole domain) to show the reduced lifetime of mushroom-like plumes under the dissipative and mixing effects. At that *Ra*, the flow regime is essentially characterized by high perturbations and a noteworthy local self-amplification of velocity derivatives $-Q_S$. It exceeds the evolution of thermal plumes, which emanate abundantly in small-scale geometries, in the BL. The plumes scatter strongly under the amplified turbulent background mixing events to make the trajectories converging towards a zero-valued origin. This accordingly has suggested that the thermal plumes at this high *Ra* number do not contribute to the mean large scales of heat flux and just give them a life. Finally, and due to the effective mixing activities, all the averaged trajectories through the bulk have revealed an upwards movement (mushroom-like plumes) decaying towards a zero-valued origins for both *Ra* numbers, since the heat flux is constant spatially and temporally in mean and the plumes are completely destroyed with zero-valued means of $Q_{\tilde{G}_\theta}$ and $R_{\tilde{G}_\theta}$.

In summary, these findings have extended the scope of small-scale turbulence universality to include the turbulent buoyancy-driven flows. On the other hand, the observations of $Q_{\tilde{G}_\theta}$ and $R_{\tilde{G}_\theta}$ invariants behaviour have demonstrated a successful prediction to the mean evolution of the small scale motions associated intrinsically with the thermal plumes, which can open many options in turbulence modeling approaches of thermals.

References

[1] R. H. Kraichnan. Some modern developments in the statistical theory of turbulence. Statistical mechanics: New concepts, New Problems, New Applications. pages 201–228, 1972.

[2] A Tsinober. *An Informal Introduction to Turbulence*, volume 63. Fluid Mechanics and its Applications, Kluwer Academic Publishers, 2001.

[3] M. S. Chong, A. E. Perry, and B. J. Cantwell. A general classification of three-dimensional flow fields. *Physics of Fluids A*, 2:765, 1990.

[4] J. Martín, A. Ooi, M. S. Chong, and J. Soria. Dynamics of the velocity gradient tensor invariants in isotropic turbulence. *Physics of Fluids*, 10:2336, 1998.

[5] A. Ooi, J. Martin, J. Soria, and M. S. Chong. A study of the evolution and characteristics of the invariants of the velocity-gradient tensor in isotropic turbulence. *Journal of Fluid Mechanics*, 381:141, 1999.

[6] G. E. Elsinga and I. Marusic. Evolution and lifetimes of flow topology in a turbulent boundary layer. *Physics of Fluids*, 22(1):015102, 2010.

[7] H. M. Blackburn, N. N. Mansour, and B. J. Cantwell. Topology of fine-scale motions in turbulent channel flow. *Journal of Fluid Mechanics*, 310:269–292, 1996.

[8] J. Soria, R. Sondergaard, B. J. Cantwell, M. S. Chong, and A. E. Perry. A study of the fine-scale motions of incompressible time-developing mixing layers. *Physics of Fluids*, 6(2):871–884, 1994.

[9] C. B. da Silva and J. C. F. Pereira. Invariants of the velocity-gradient, rate-of-strain, and rate-of-rotation tensors across the turbulent/nonturbulent interface in jets. *Physics of Fluids*, 20(5):055101, 2008.

[10] K. Hanjalić. One-point closure models for buoyancy-driven turbulent flows. *Annual Reviews of Fluid Mechanics*, 34:321–347, 2002.

[11] D. Lohse and K. Xia. Small-scale properties of turbulent Rayleigh-Bénard convection. *Annual Reviews of Fluid Mechanics*, 42:335–364, 2010.

[12] J. Schumacher. Lagrangian dispersion and heat transport in convective turbulence. *Physical Review Letters*, 100:134502, 2008.

[13] Y. Gasteuil, WL. Shew, M. Gilber, F. Chillà, B. Castaing, and JF. Pinton. Lagrangian temperature, velocity, and local heat flux measurement in Rayleigh-Bénard convection. *Physical Review Letters*, 99:234302, 2007.

[14] J. Scheel, M. S. Emran, and J. Schumacher. Resolving the fine-scale structure in turbulent Rayleigh-Bénard convection. *New Journal of Physics*, 15:113063, 2013.

[15] M. Kaczorowski and K. Xia. Turbulent flow in the bulk of Rayleigh-Bénard convection: small-scale properties in a cubic cell. *Journal of Fluid Mechanics*, 722:596–617, 2013.

[16] J. Schumacher, J. D. Scheel, D. Krasnov, D. A. Donzis, V. Yakhot, and K. R. Sreenivasan. Small-scale universality in fluid turbulence. *Proceedings of the National Academy of Sciences of the USA*, 111(30):10961–10965, 2014.

[17] S. Park and C. Lee. Analysis of coherent structures in Rayleigh-Bénard convection. *Journal of Turbulence*, 16(12):1162–1178, 2015.

[18] B. J. Cantwell. On the behavior of velocity gradient tensor invariants in direct numerical simulations of turbulence. *Physics of Fluids A*, 5:2008, 1993.

[19] A. E. Perry and M. S. Chong. Topology of flow patterns in vortex motions and turbulence. *Applied Scientific Research*, 53:357–374, 1994.

[20] F. X. Trias, D. Folch, A. Gorobets, and A. Oliva. Building proper invariants for eddy-viscosity subgrid-scale models. *Physics of Fluids*, 27:065103, 2015.

[21] P. E. Hamlington, J. Schumacher, and W. J. A. Dahm. Direct assessment of vorticity alignment with local and nonlocal strain rates in turbulent flows. *Physics of Fluids*, 20:111703, 2008.

[22] B. J. Cantwell. Exact solution of the restricted Euler equation for the velocity gradient tensor. *Physics of Fluids A*, 4:782, 1992.

[23] M. Wilczek. New insights into the fine-scale structure of turbulence. *Journal of Fluid Mechanics*, 784:1–4, 2015.

[24] S. Grossmann and D. Lohse. Fluctuations in turbulent Rayleigh-Bénard convection: The role of plumes. *Physics of Fluids*, 1:4462–4472, 2004.

[25] M. Kholmyansky, A. Tsinober, and S. Yorish. Velocity derivatives in the atmospheric surface layer at $Re_\lambda = 10^4$. *Physics of Fluids*, 13:311–314, 2001.

[26] B. Lüthi, M. Holzner, and A. Tsinober. Expanding the Q-R space to three dimensions. *Journal of Fluid Mechanics*, 641:497–507, 2009.

[27] F. Chillà and J. Schumacher. New perspectives in turbulent Rayleigh-Bénard convection. *The European Physics Journal E*, 35:58, 2012.

[28] M. S. Emran and J. Schumacher. Fine-scale statistics of temperature and its derivatives in convective turbulence. *Journal of Fluid Mechanics*, 611:13–34, 2008.

[29] S. Q. Zhou and K. Q. Xia. Plume statistics in thermal turbulence: mixing of an active scalar. *Physical Review Letters*, 89:184502, 2002.

[30] S. Q. Zhou and K. Q. Xia. Physical and geometrical properties of thermal plumes in turbulent Rayleigh-Bénard convection. *New Journal of Physics*, 12:075006, 2010.

[31] S. Q. Zhou, C. Sun, and K. Q. Xia. Morphological evolution of thermal plumes in turbulent Rayleigh–Bénard convection. *Physical Review Letters*, 98:074501, 2007.

3

A priori study of subgrid-scale features in turbulent Rayleigh-Bénard convection

Main contents of this chapter have been published in:

F. Dabbagh, F. X. Trias A. Gorobets and A. Oliva, *A priori* study of subgrid-scale features in turbulent Rayleigh-Bénard convection , *Physics of Fluids*, 2017 (submitted).

F. Dabbagh, F. X. Trias A. Gorobets and A. Oliva, New subgrid-scale models for large-eddy simulation of Rayleigh-Bénard convection, *Journal of Physics: Conference Series*, **745**, 032041, 2016.

Abstract. At the crossroad between flow topology analysis and turbulence modeling, *a priori* studies are a reliable tool to understand the underlying physics of the subgrid-scale (SGS) motions in turbulent flows. In this chapter, properties of the SGS features in the framework of large-eddy simulation are studied for a turbulent Rayleigh-Bénard convection (RBC). To do so, data from direct numerical simulation (DNS) in chapter 1, is employed. Firstly, DNS at $Ra = 10^8$ is used to assess the performance of eddy-viscosity models such as, QR, WALE and the recent S3PQR-models proposed by Trias *et al.*[PoF, 27, 065103 (2015)]. The outcomes imply that the eddy-viscosity modeling smoothes the coarse-grained viscous straining and retrieves

fairly well the effect of the kinetic unfiltered scales in order to reproduce the coherent large scales. However, these models fail to approach the exact evolution of the SGS heat flux, and are incapable to reproduce well the further dominant rotational enstrophy pertaining to the buoyant production. Afterwards, the key ingredients of eddy-viscosity, ν_t, and eddy-diffusivity, κ_t are calculated *a priori* and revealed a positive prevalent values to maintain a turbulent wind essentially driven by the mean buoyant force at the sidewalls. The topological analysis suggests that the effective turbulent diffusion paradigm and the hypothesis of constant turbulent Prandtl number are only applicable in the large-scale strain-dominated areas in the bulk. It is shown that the bulk-dominated rotational structures of vortex-stretching (in concomitant the viscous dissipative structures) hold the highest positive values of ν_t, however the zones of backscatter energy and countergradient heat transport are related to the areas of compressed focal vorticity. More arguments have been attained through *a priori* investigation of the alignment trends imposed by existing parameterizations for the SGS heat flux, tested here inside RBC. It is shown that the parameterizations based linearly on the resolved thermal gradient are invalid in RBC. Alternatively, the tensor-diffusivity approach becomes a crucial choise of modeling the SGS heat flux, in particular the tensorial diffusivity that includes the SGS stress tensor. This and other crucial scrutinies on a future modeling to the SGS heat flux in RBC are sought.

3.1 Introduction

Buoyancy-driven flows have always been an important subject of scientific studies with numerous applications in environment and technology. A famous example thereof is the thermally driven flow developed in a fluid layer heated from below and cooled from above, *i.e.* Rayleigh-Bénard convection (RBC) [1]. It approaches many circulations in nature and industry, such as governing flows in nuclear reactors, solar thermal power plants, electronic devices, and convection in atmosphere, oceans and deep mantle. Most of these flows are ruled by turbulent regime purely sustained by buoyancy, the reason that imparts a significant complexity into the flow system. Mainly, the chief dynamics therein such as the vortical structures and thermal plumes are essentially associated with immanent unsteadiness, energy nonequilibriums, strong pressure fluctuations and hardly interacted different-size scales of motions [2]. Following the self-sustained cycle of the plumes, they produce alternative nonequilibriums between the buoyant production and the viscous dissipation, which are mainly compensated by the pressure transport mechanisms [3]. As a consequence, predicting the complex coherent dynamics in a turbulent RBC derives formidable challenges, particularly within the scope of turbulence modeling.

Direct numerical simulation (DNS) has provided a fruitful knowledge about the problem in the fields of coherent dynamics and turbulence physics [4, 5]. Apart from overcoming the uncertainties pertaining to the experimental studies, DNS has allowed to investigate and resolve many queries in RBC at relatively high Rayleigh (Ra) numbers [6, 7]. However, the fully-resolution of every generated vortical filament in DNS requires increasing computational demands with Ra. Therefore, in the foreseeable future the numerical simulations of hard turbulent RBC will have to resort to turbulence modeling. An approach which has gained a considerable attention in recent years is the Large-eddy simulation (LES). Therein, only the large-scale energy containing flow is computed directly and the influence of the small scale motions, which is assumed as isotropic and universal, is modeled. The key feature of LES depends on how properly the unresolved subgrid-scale (SGS) of the Reynolds stress and heat flux terms evolved in the filtered governing equations, are approximated. Following the prominent assumption of eddy-viscosity, ν_t, modeling, Eidson [8] extended the well-known Smagorinsky model by including the buoyant production contribution in evaluating ν_t for RBC. His results showed a good consistency with experiments at low numbers of Ra, however for hard turbulent regimes, they start to be occasionally erroneous with non-real behavior [9]. Peng and Davidson [9], later modified the Eidson's formula to remedy this problem. They applied the dynamic procedure [10,11] to compute the model coefficients. Then, in Ref. [12], they employed the dynamic Smagorinsky model in evaluating ν_t with the dynamic approach for the turbulent Prandtl number, Pr_t, used to calculate the eddy-diffusivity, κ_t, (gradient

diffusion assumption). The dynamic procedure provided results that agree fairly well with DNS, however this approach has multiple limitations. Namely, the averaging procedure in the periodic-directions is necessary in order to prevent numerical instabilities. This makes the dynamic approach less amenable for geometrically complex flows. Another authors as Czarnota *et al.* [13] had performed a comparative study using the dynamic Smagorinsky model and the dynamic scale similarity model for the momentum equation in RBC. They used the model of Peng and Davidson [14] for the SGS heat flux, and showed that the dynamic Smagorinsky model produces occasionally unphysical temperature values. More recent, Foroozani *et al.* [15] has applied the Lagrangian dynamic technique [16] in the Smagorinsky model. The above-mentioned clipping of the dynamic procedure is overcome in the Lagrangian averaging, however the procedure entails significant complexity and computational cost. In a general perspective, most of the aforesaid strategies of thermal turbulence modeling (LES) are restrained by such complexities, considerable cost and the necessity to use a dynamic technique in order to precisely follow the interacted scales of buoyant/strain production. Hence, a critical understanding of the problem dynamics in the frame of turbulence modeling performance is necessary.

Based on the DNS results, the statistical analysis of the SGS features becomes of great interest in verifying the assumptions of existing models. It can provide insights on the underlying physics of the small scale dynamics in the spirit of turbulence models. Hence, one can note how well the model matches the topological characteristics, *e.g.* the alignment trends, of the modeled quantities with respect to the resolved flow structures. In this chapter, we first investigate *a posteriori*, the performance of LES eddy-viscosity models, such as WALE, QR and the novel S3PQR [17] modeling, in RBC at $Ra = 10^8$. Therein, the SGS heat flux is modeled following the gradient transport hypothesis where the assumption of constant-Pr_t, is used. These models possess important properties, such as the simplicity and the ability to work in complex geometries without limitations. Afterwards, the key ingredients in the LES models of the eddy-viscosity ν_t, eddy-diffusivity κ_t and turbulent Prandtl number Pr_t, are studied *a priori*. The analysis includes a statistical study of the underlying flow topology associated to the SGS components. Moreover, we investigate *a priori* the performance of SGS heat flux models defined in the frame of the gradient diffusion assumption (the SGS heat flux in aligned against the thermal gradient). Namely, we propose to judge the behavior of the most used SGS heat flux models such as Peng and Davidson [14] and Daly and Harlow [18] in the mixed model space, similar to Higgins *et al.* [19]. The data set used is based on our DNS results of an air turbulent RBC at $Ra = 10^8$ and 10^{10}, performed in chapter 1.

The remainder of the chapter is organized as follows. A comparative test regard-

Table 3.1: Summary of detailed parameters relevant to the DNS (Table 1.1) and LES, providing the overall Nu results. η_{LES} is identically defined as η_{DNS} by, $(\Delta x \Delta y \Delta z)^{1/3}_{max}$.

DNS			LES ($Pr_t = 0.4$)		
	$Ra = 10^8$	$Ra = 10^{10}$		$Ra = 10^8$	
	$N_x \times N_y \times N_z$	$N_x \times N_y \times N_z$		Mesh A	Mesh B
Mesh	$400 \times 208 \times 208$	$1024 \times 768 \times 768$		$N_x \times N_y \times N_z$	$N_x \times N_y \times N_z$
				$120 \times 80 \times 80$	$168 \times 110 \times 110$
$\iota_y = \iota_z$	1.4	1.6	$\iota_y = \iota_z$	2	2
Δt	1.45×10^{-3}	4.14×10^{-4}	Δt	2.56×10^{-3}	1.46×10^{-3}
			$\xi[TU]$	500	500
N_{BL}	9	12	N_{BL}	6	8
			η_{LES}	2.62×10^{-2}	1.87×10^{-2}
η_{DNS}	7.7×10^{-3}	2.50×10^{-3}	Nu		
			No-model	39.2	35.6
$\xi[TU]$	500	200	S3QR	38.0	35.0
			QR	38.6	35.4
			WALE	35.6	33.3
$\xi_{st}[\tau_{eddy}]$	40	10	$\xi_{st}^{\text{No-model}}[\tau_{eddy}]$	–	94
Nu	30.9	128.1	$\xi_{st}^{\text{S3QR}}[\tau_{eddy}]$	–	94

ing the performance of such well-known eddy-viscosity models in LES is presented in § 3.2. Afterwards, *a priori* study over the SGS components of the Pr_t is included in § 3.3. The statistical analysis of the SGS heat flux models is addressed in § 3.4, and a new approach towards a future modeling of the SGS heat flux in RBC is proposed. Finally, relevant results are summarized and conclusions are given.

3.2 Large-eddy simulation models and flow topology

The LES equations result from applying a spatial filtering to the governing equations (Eqs. 1.2 and 1.3), as following

$$\partial_t \bar{\boldsymbol{u}} + (\bar{\boldsymbol{u}} \cdot \nabla)\bar{\boldsymbol{u}} = -\nabla \bar{p} + (Pr/Ra)^{1/2} \nabla^2 \bar{\boldsymbol{u}} + \bar{\boldsymbol{f}} - \nabla \cdot \bar{\tau}, \quad \nabla \cdot \bar{\boldsymbol{u}} = \boldsymbol{0}, \tag{3.1}$$

$$\partial_t \bar{T} + (\bar{\boldsymbol{u}} \cdot \nabla)\bar{T} = (RaPr)^{-1/2} \nabla^2 \bar{T} - \nabla \cdot \bar{\boldsymbol{q}}, \tag{3.2}$$

where $\bar{\boldsymbol{u}}$, $\bar{T}$ and $\bar{p}$ are respectively the filtered velocity, temperature and pressure. The filtered large scales above a filter length Δ in the Kolmogorov equilibrium, and which are more energetic and boundary conditions dependent, are resolved directly.

However, the SGS turbulence that is assumed to be more isotropic in nature is modeled. Hereafter, the overbar-terminology $\bar{(\cdot)}$ refers to the filtered fields, while the non-overlined terms refer to DNS fields. The SGS stress tensor $\bar{\tau}$ and the SGS heat flux vector $\bar{\boldsymbol{q}}$, approximate the effect of the (small) under-resolved scales,

$$\bar{\tau} \simeq \overline{\boldsymbol{u} \otimes \boldsymbol{u}} - \bar{\boldsymbol{u}} \otimes \bar{\boldsymbol{u}}, \tag{3.3}$$

$$\bar{\boldsymbol{q}} \simeq \overline{\boldsymbol{u}T} - \bar{\boldsymbol{u}}\bar{T}, \tag{3.4}$$

and they need to be modeled in order to close the system. The most popular approach is the eddy-viscosity assumption, where the SGS stress tensor is computed in alignment with the local strain rate tensor, $\bar{\mathsf{S}} = 1/2(\nabla\bar{\boldsymbol{u}} + \nabla\bar{\boldsymbol{u}}^t)$, *i.e.*,

$$\bar{\tau} \approx -2\nu_t\bar{\mathsf{S}}. \tag{3.5}$$

In analogy to $\bar{\tau}$, the SGS heat flux is approximated employing the gradient-diffusion hypothesis, given as

$$\bar{\boldsymbol{q}} \approx -\kappa_t\nabla\bar{T}, \tag{3.6}$$

and the Reynolds analogy assumption is applied in evaluating κ_t. Namely, in a turbulent system the heat flux is assumed to be analogous to the momentum flux and its ratio therefore, is constant. In this case, the eddy-diffusivity, κ_t, is derived from the eddy-viscosity, ν_t, by a constant turbulent Prandtl number Pr_t independent of the instantaneous flow conditions, as follows

$$\kappa_t = \nu_t / Pr_t. \tag{3.7}$$

An investigation of the underlying physics of the Pr_t and its determined constant value is presented in § 3.3. In this section, the value of Pr_t is assigned to the most used value in literature [8], *i.e.* $Pr_t = 0.4$. The ν_t value is evaluated here within a comparative examination of three eddy-viscosity models such as QR, WALE and the novel S3PQR models [17] proposed by the authors. They all possess a list of desirable properties based on physical, numerical and practical arguments. For example, positiveness and locality (all three models), the proper cubic near-wall behavior (WALE and S3PQR), automatically switching off $(\nu_t = 0)$ for 2D flows (S3PQR and QR), they are well-conditioned and do not have any intrinsic limitation for statistically inhomogeneous flows (all). In rely on a combination of invariants of the resolved velocity gradient tensor $\bar{\mathsf{G}} \equiv \nabla\bar{\boldsymbol{u}}$, the foregoing models can be described in a unified framework [17]. Namely,

$$\nu_t^{S3QR} = (C_{s3qr}\Delta)^2 Q_{\bar{\mathsf{G}}\bar{\mathsf{G}}^t}^{-1} R_{\bar{\mathsf{G}}\bar{\mathsf{G}}^t}^{5/6}, \tag{3.8}$$

$$\nu_t^{QR} = (C_{qr}\Delta)^2 \frac{|R_{\bar{\mathsf{S}}}|}{-Q_{\bar{\mathsf{S}}}}, \tag{3.9}$$

$$\nu_t^{WALE} = (C_W\Delta)^2 \frac{(\mathsf{V}_{\bar{\mathsf{G}}}^2/2 + 2Q_{\bar{\mathsf{G}}}^2/3)^{3/2}}{(-2Q_{\bar{\mathsf{S}}})^{5/2} + (\mathsf{V}_{\bar{\mathsf{G}}}^2/2 + 2Q_{\bar{\mathsf{G}}}^2/3)^{5/4}}, \tag{3.10}$$

where $Q_{\bar{\mathsf{G}}\bar{\mathsf{G}}^t} = \mathsf{V}_{\bar{\mathsf{G}}}^2 + Q_{\bar{\mathsf{G}}}^2$ and $R_{\bar{\mathsf{G}}\bar{\mathsf{G}}^t} = -R_{\bar{\mathsf{G}}}^2$, are the second and the third invariants of the $\bar{\mathsf{G}}\bar{\mathsf{G}}^t$ tensor, respectively. $C_{(\cdot)}$ is the model's constant determined as $C_{s3qr} = 0.762$ [17], $C_W = \sqrt{0.5}$ [20] and $C_{qr} = 1/\pi\sqrt{3/2}$ [21], and $\mathsf{V}_{\bar{\mathsf{G}}}^2$ is the L^2-norm of the vortex-stretching vector $\mathsf{V}_{\bar{\mathsf{G}}}^2 = |\bar{\boldsymbol{\omega}}\bar{\mathsf{S}}|^2$.

3.2.1 *A posteriori* LES results

For the sake of low computational cost we restrict our *a posteriori* analysis to the lowest turbulent case ($Ra = 10^8$). We use two coarse meshes for LES (Mesh A and Mesh B presented in Table 3.1). The meshes are constructed keeping the same grid points distribution as for the DNS but with a coarser spatial resolution. The concentration parameters used $\iota_z = \iota_y$, have been modified in order to increase the boundary layer grid resolution. Regarding to the numerical discretisation and algorithms used, all are adopted similarly to the DNS (§ 1.2.2), where the same trusty converging periods (ξ) are employed. Table 3.1 shows detailed parameters relevant to LES, along with the DNS parameters, where the overall Nu results given by each model are presented. The performance of the eddy-viscosity models is assessed by a comparison with the DNS profiles of turbulent statistics such as, the turbulent kinetic energy and heat flux, averaged in time and homogeneous direction. The profiles are extracted at the midwidth plane ($z = 0.5$) and represented in Figures 3.1 and 3.2, respectively, for $\langle\bar{k}\rangle$ and $\langle\bar{w}'\bar{T}'\rangle$, on the two grids used, *i.e.* Mesh A (left) and Mesh B (right). As it can be seen in Figure 3.1, the turbulent kinetics are fairly well predicted with the S3QR and WALE models, both in the bulk and the near-wall areas. They give an enhanced capturing of the kinetics evolution in comparison with the case of not using any model (the No-model case) at the coarser grid (Mesh A in Figure 3.1(a)). When the grid spacing becomes refined (in Mesh B), the turbulent energy contained in the unfiltered scales (SGS) is less. Hence, a subsequent grid refinement should asymptotically drive a LES to DNS and Mesh B is appropriately resolving the turbulent kinetic quantities in Figure 3.1(b). Regarding the turbulent heat flux, all the models fail in predicting the fluctuated thermals, particularly in the near-wall areas. They seem to overestimate the turbulent heat flux peak, as shown in Figure 3.2, which is essentially related to the role of the thermal plumes in the bulk region (transitional area). As a result, the obtained Nu values are overestimated (see Table 3.1) in all the models. Similar to Figure 3.1(b), the modeling of turbulent heat flux performs better on the refined grid (Mesh B in Figure 3.2(b)). The effect of the SGS modeling on the coarser grid (Mesh A in Figure 3.2(a)) is more notable than on the refined grid (Mesh B), if we compare it with the No-model case (particularly in the bulk). Moreover, the more refined grid, the closer behavior between the LES modeling and the No-model, till approaching the DNS mesh. Hence, in the case of hard turbulent regime, *i.e.* at $Ra = 10^{10}$, the trustworthy LES grid size is found to be of an excessive level. The structures at that

Ra, have revealed a self-amplification of the (turbulent background) viscous straining $(-Q_S)$, and simultaneously of enstrophy (Q_Ω) § 2.2.1. As a result, both buoyant and strain productions take place on scaled-down motions and require very refined grids.

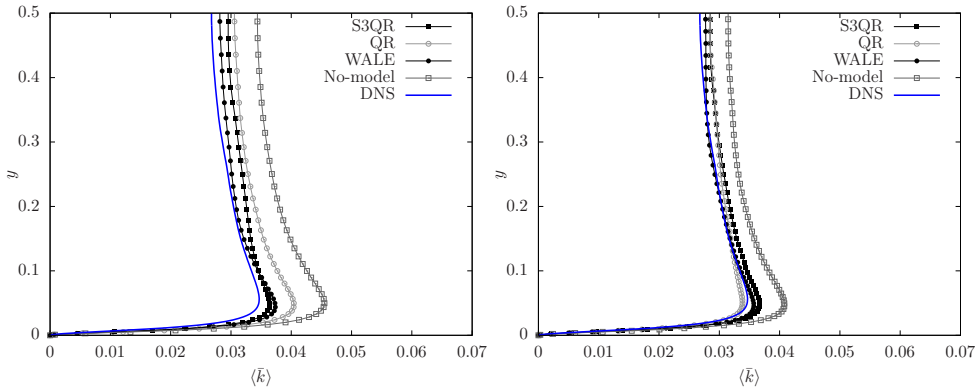

Figure 3.1: Vertical profiles of the turbulent kinetic energy $\langle \bar{k} \rangle$, taken along the mid-width $z = 0.5$ plane and averaged in time and homogeneous x-direction on two grids, Mesh A (a) and Mesh B (b).

In order to explore the underlying influence of the SGS modeling, we conduct a statistical analysis related to flow topology classification and dominant small-scale physics for the cases of DNS, No-model and S3QR modeling. This last one is chosen as a representative LES modeling since no important differences among different models are observed. To do so, five joint probability density function (JPDF) spaces of invariant pairs pertaining to the velocity gradient tensor, normalized using $\langle Q_\Omega \rangle$ (following Ooi *et al.* [22]), have been considered in the bulk (V_{bulk}) at $Ra = 10^8$. The instantaneous data is gathered over adequate converging periods ($\xi_{st}^{\text{No-model}}$ and ξ_{st}^{S3QR}, in Table 3.1). Firstly, the JPDF of (Q_G, R_G) invariants plotted in Figures 3.3(a),3.3(b) and 3.3(c), reveals the well-known inclined "teardrop" shape as a universal feature of small-scale turbulence. Meaning that, the fine flow patterns obey substantially stable tube-like vortex stretching structures and in concomitant, unstable sheet-like viscous dissipative structures in the bulk of RBC, as showed in § 2.2.1. It can be seen from Figure 3.3(c) that the S3QR model successfully reproduces the coherent large-scale structures allocated normally near the origin. It retrieves the effect of the unfiltered scales at the filter length Δ and relaxes the spatial resolution in the dominant struc-

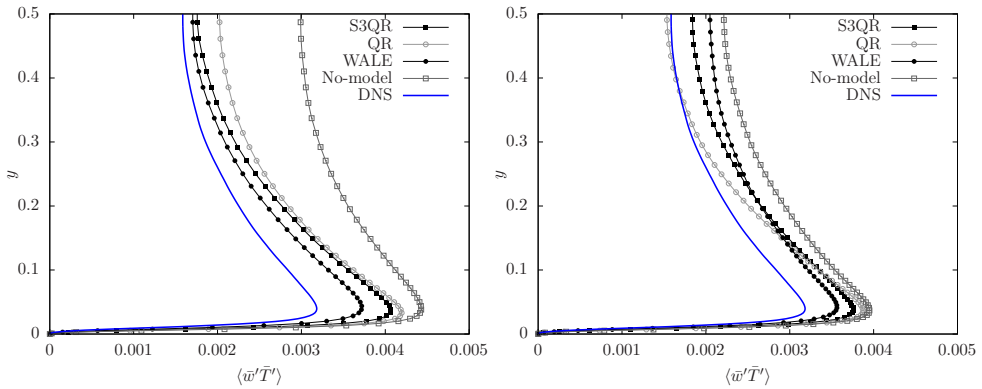

Figure 3.2: Vertical profiles of the turbulent heat flux $\langle \bar{w}'\bar{T}' \rangle$, taken along the mid-width $z = 0.5$ plane and averaged in time and homogeneous x-direction on two grids, Mesh A (a) and Mesh B (b).

tures of tube-like vortex-stretching and sheet-like viscous dissipation. In contrast, Figure 3.3(b) displays highly dispersed distribution with excessive spatial viscous dissipation in the case of No-model. It reveals the coarse-grained velocity gradient distribution in the inertial range where the energy transfer is associated with the large negative straining ($R_S < 0$) [23]. In this span, it occurs on the axisymmetric contracted deformation aligned with the left null-discriminant tent-line ($D_G = 0$) in Figure 3.3(b), or more evidently its counterpart $D_S = 0$ of (Q_S, R_S) space in Figure 3.3(e). The (Q_S, R_S) map is particularly useful to analyze the geometry of the local straining of the fluid elements. As a universal aspect of turbulent flows, a strong preference for the zone $R_S > 0$, $Q_S < 0$, indicating a predominance of sheet-like structures to the kinetic energy dissipation, appears in Figures 3.3(d), 3.3(e) and 3.3(f). It can be seen the well-smoothing of the small-scale effect retrieved to the large-scale shear by using the model in comparison with the case of the No-model, notably near the left $D_S = 0$ line. ($-Q_S, Q_\Omega$) map provides physical information about the dominant flow topologies with respect to the kinetic energy dissipation. The horizontal line Q_Ω represents points of high enstrophy but very small dissipation indicating the solid-body rotational at the center of the vortex tubes, while the vertical line $-Q_S$ represents points of strong dissipation but little enstrophy density to indicate the irrotational straining outside and away from the vortex tubes. Balanced distribution of $Q_\Omega = -Q_S$ translates vortex sheet structures that normally occurs in the boundary layers. As showed in § 2.2.1, the DNS in Figure 3.3(g), manifests that the flow topology is mainly

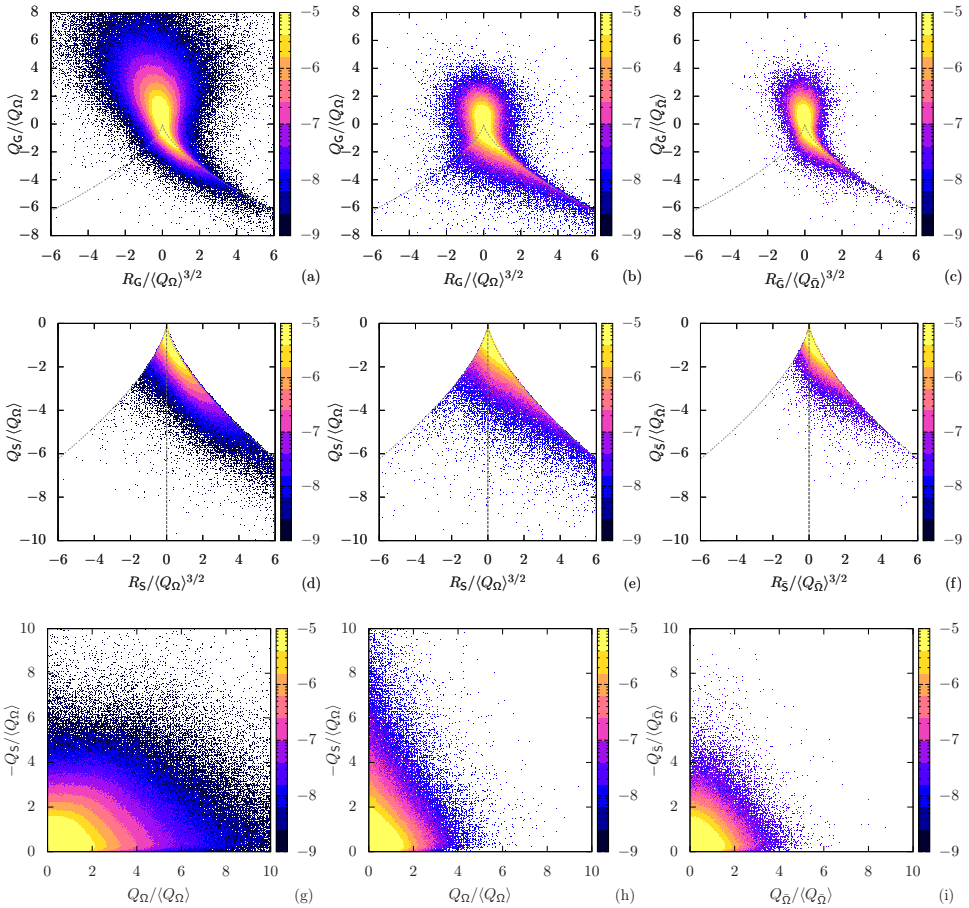

Figure 3.3: JPDF of normalized invariants pair for the corresponding DNS (left), No-model (middle) and S3QR-modeling (right). (Q_G, R_G) in (a,b,c), (Q_S, R_S) in (d,e,f), $(-Q_S, Q_\Omega)$ in (g,h,i). The data used are extracted from the bulk region at $Ra = 10^8$. Coarse-grained simulations (No-model and S3QR) correspond to Mesh B (see Table 3.1). The dashed tent-lines therein refer to the corresponding null-discriminants.

tube-like rotational in the bulk region, where the highest local value of $-Q_S$ is smaller than the highest local value of Q_Ω, and the JPDF is horizontally shifted towards the long-lived solid-body rotation. This grouping is reversed in the No-model case due to the high viscous dissipation produced, as shown in Figure 3.3(h). However, the S3QR

modeling displays a subtle balance between the rotational enstrophy and the strain dissipation in Figure 3.3(i). It restrains the production of further enstrophy pertained to the buoyancy and thermal plumes in the bulk, and hence it is unable to capture well the subtle coupling of buoyant production and viscous straining. In fact, this can give a trend for the eddy-viscosity modeling to work better at very hard turbulent regime when the turbulent background dissipation is amplified enough (at much harder turbulence, $Ra > 10^{10}$). However in this case, the modeling should keep in consideration two issues: the good prediction to the orientation of the SGS thermals and the high refined grid sufficient for the scaled-down straining. Finally, the invariants

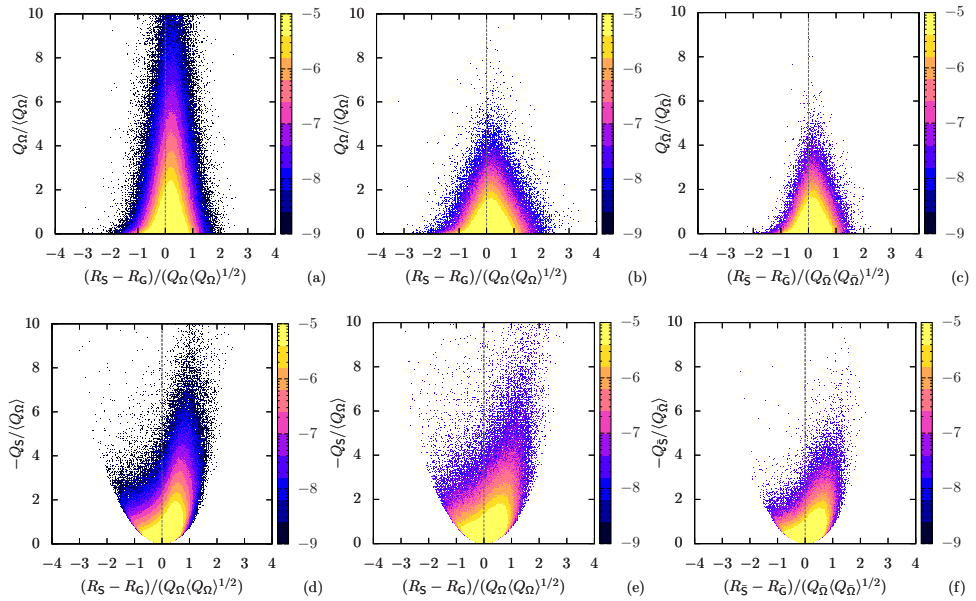

Figure 3.4: JPDF of normalized invariants pair for the corresponding DNS (left), No-model (middle) and S3QR-modeling (right). $(Q_\Omega, (R_S - R_G)/Q_\Omega)$ in (a,b,c), and $(-Q_S, (R_S - R_G)/Q_\Omega)$ in (d,e,f). The data used are extracted from the bulk region at $Ra = 10^8$. Coarse-grained simulations (No-model and S3QR) correspond to Mesh B (see Table 3.1).

combination $(R_S - R_G/Q_\Omega, Q_\Omega)$ and $(R_S - R_G/Q_\Omega, -Q_S)$ spaces in Figure 3.4, indicate the underlying mechanisms of the vorticity magnitude to be amplified/reduced by the positive (stretched vortex)/negative (contracted vortex) sign of the stretching rate $(R_S - R_G)/Q_\Omega$, in relation to Q_Ω (enstrophy) and $-Q_S$ (strain rate) quantities. The DNS-based JPDF maps are displayed in Figures 3.4(a) and 3.4(d), and show a

persistent consistency with the isotropic turbulence behavior studied by Ooi *et al.* [22]. As shown in both Figures, most of the points in the flow have a positive stretching rate and the enstrophy production is positive on average § 2.2.1. In Figure 3.4(a), the high stretching rate is associated with regions of small Q_Ω implying that there is little evidence of self-stretching by strong enstrophy structures, as interpreted by Jiménez *et al.* [24]. On the contrary, Figure 3.4(d) shows a wider growing of stretching rate with increasing strain $-Q_S$ up to a certain value. In general, the magnitude of the stretching rate (stretching/compressing) is associated with regions of moderate to high $-Q_S$ [22]. This in fact was also demonstrated before in § 2.2.3, where it was emphasized on the local collaborating role of vortex compression $(R_S - R_G < 0)$ and strain generation $(R_S > 0)$, that always result in a positive contribution to the magnitude of the vortex-stretching vector. Regarding to the S3QR modeling, it gives a refined and smoothed stretching rate alignment, reproducing the consistent DNS large-scale topology (Figures 3.4(c) and 3.4(f)). However, the No-model case produces coarse-grained higher magnitudes for all quantities, as displayed in Figures 3.4(b) and 3.4(e).

3.3 Turbulent Prandtl number Pr_t

Turbulent Prandtl number is defined as the ratio between ν_t and κ_t, $(Pr_t = \nu_t/\kappa_t)$ indicating the balanced link between the subgrid-scale effects of thermals and kinetics in a turbulent system. It forms an extremely difficult quantity to measure in experiments, and intimately depends on the molecular fluid properties and the flow parameters [25]. For example, in the scope of the most used Reynolds analogy in considering a constant value of Pr_t, Kim and Moin [26] gave a range of the turbulent Prandtl number from 0.4 in the center to 1 near the walls of a forced convection heat transfer air channel flow. Pallares and Davidson [27] clarified that just a simple value $Pr_t = 0.4$ agrees well with the DNS and experiments. However these results were restricted to an air flow $(Pr \sim 1)$. In RBC, Eidson [8] also suggested a value of 0.4 in his model that included the SGS buoyant production contribution in evaluating ν_t. In summary, different values can be found in the literature ranging from 0.1 to 1, according to Sagaut [28], in addition to the dynamic procedures (time and space dependent) [29] and temperature dependent [30] Pr_t models. The majority are sharing the behavior of flat profile of Pr_t in the bulk and increased maximum values near the wall in stratified and buoyancy-driven flows. In the present work, the Pr_t has been evaluated *a priori* using our DNS database. To do so, the right-hand-sides of Eqs. 3.3 and 3.4 have been approximated by the leading term of the Taylor series expansion, *i.e.* $\bar{\tau} \approx (\Delta^2/12)\mathsf{G}\mathsf{G}^t$ and $\bar{\boldsymbol{q}} \approx (\Delta^2/12)\mathsf{G}\nabla T$. Then, the values of ν_t and κ_t are obtained

using a least square minimization in Eqs. 3.5 and 3.6, as follows

$$\nu_t \approx -(\Delta^2/12)\frac{\mathsf{G}\mathsf{G}^t : \mathsf{S}}{2\mathsf{S} : \mathsf{S}}, \qquad \kappa_t \approx -(\Delta^2/12)\frac{\mathsf{G}\nabla T \cdot \nabla T}{\nabla T \cdot \nabla T}. \tag{3.11}$$

This can result into a dynamical model of Pr_t, however with ill-conditioning properties. In this case, an ensemble temporal average procedure is necessary since it can produce negative diffusion (or eddy-viscosity), which potentially may lead to a blowup in the simulation [31,32]. Plotting the averaged temporal-(x,z) profiles of these estimations, *i.e.*, $\langle\nu_t\rangle_A$, $\langle\kappa_t\rangle_A$ and $Pr_t = \langle\nu_t\rangle_A/\langle\kappa_t\rangle_A$ in Figure 3.5, various attributes can be observed. Mainly and in consistency with the literature, the turbulent Prandtl number reveals a similar behavior by taking a constant value through the bulk $Pr_t \approx 0.55$ that increases near the walls toward numbers larger than 1. Interestingly the value of Pr_t seems to be independent of Ra, and corresponds fairly well to the most popular literature value ($Pr_t = 0.4$). The profiles of the $\langle\nu_t\rangle_A$ and $\langle\kappa_t\rangle_A$ are positively skewed in average near the walls in agreement with the *a priori* analysis results of Kimmel *et al.* [33] and the dynamic models of Peng and Davidson [9]. Its

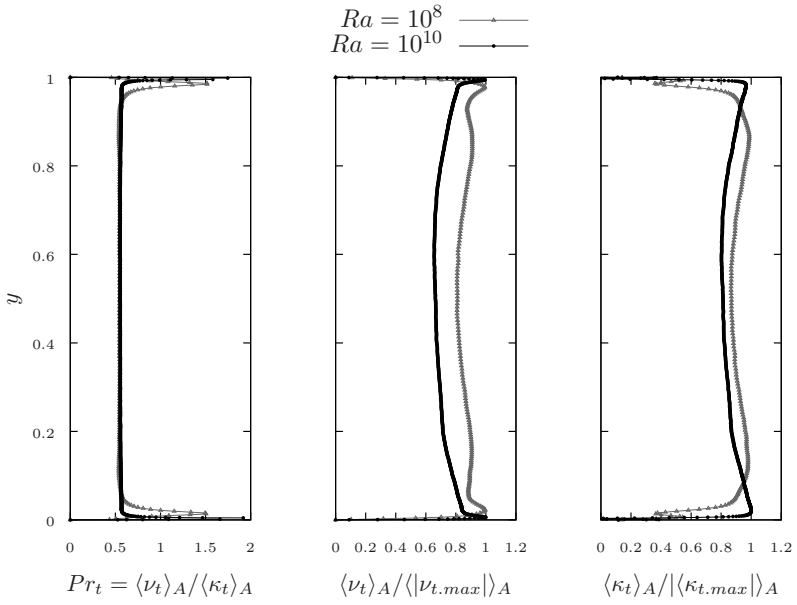

Figure 3.5: Vertical profiles of the averaged time and (x,z) plane of ν_t and κ_t, evaluated from Eq. 3.11 and normalized by its maximals, and the consequent Pr_t.

distribution shape is relatively close to that one found in Peng and Davidson [9],

taking into account the difference of the laterally confined domain and the higher turbulent regime considered here. Indeed, the findings of Burr *et al.* [34] also proposed the average positive prevalence of the turbulent energy production, *i.e.*, positive ν_t. They claimed in consequence, that the mean flow is driven by the mean buoyant forces and not by the Reynolds stresses associated with the turbulent fluctuations (negative turbulent energy production and energy transport from fluctuations to the mean flow) [34].

A clearer picture can be attained from the averaged temporal-x plane of $\langle \nu_t \rangle$ and $\langle \kappa_t \rangle$, shown in Figure 3.6 at $Ra = 10^8$ (the case that is clearer characterized by long-lived evolution of thermal plumes before getting shed in the bulk). Therein, both terms reveal negative values limited in the corners of the lateral adiabatic sidewalls. Note that negative values of $\langle \kappa_t \rangle$ correspond to countergradient heat transport essentially generated by two mechanisms: one is due to the bulk dynamics and the other is due to the competition between the corner-flow rolls and the large-scale circulation [35]. The highest positive values of $\langle \kappa_t \rangle$ correspond to the tilted plumes traveling in groups within the vicinities of the sidewalls where the $\langle \nu_t \rangle$ values are very small (almost zero). While, next to the thermal BLs, $\langle \nu_t \rangle$ presents high positive magnitudes in regions of the impinging bulk dynamics (mixing action or the opposite-side plumes) to concentrate with four peaks of $\langle \nu_t \rangle$ in the four corners (see Figure 3.6, left). Such similar contours are observed in the case of $Ra = 10^{10}$ with much finer

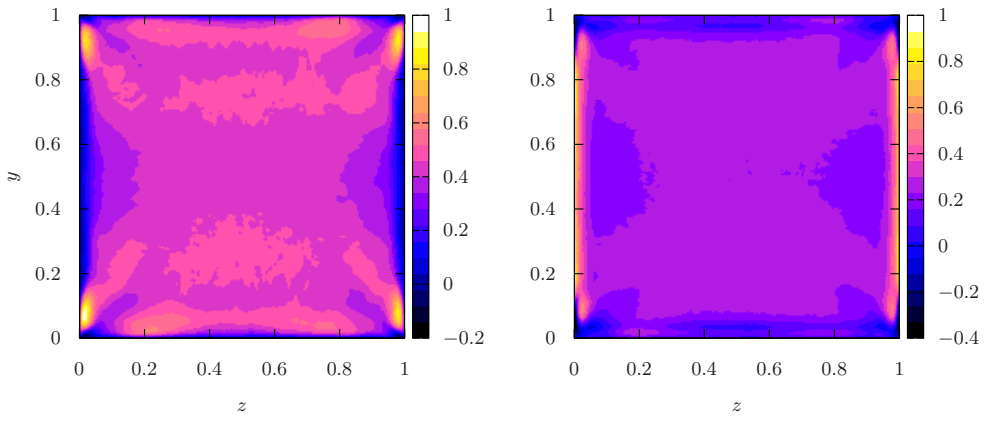

Figure 3.6: Averaged time and homogeneous x-direction planes of ν_t (left) and κ_t (right), evaluated from Eq. 3.11 and normalized by its maximals.

patterns of high negative and positive values in the near-wall vicinities. In conclusion, one can argue that the coherent mean mechanism in the current configurations obeys

a positive SGS eddy-viscosity and a turbulent wind driven by the mean buoyant forces at the sidewalls [34]. The buoyant sidewall-flow is mostly characterized by incorporating groups of swept rising-hot and falling-cold thermal plumes that were claimed to convey Reynolds stresses diverging [36]. These groups are eventually combined and produce buoyancy-driven upward/hot and downward/cold mean streams at one side and its opposite. This mean sidewall circulation becomes reduced significantly in the higher turbulent case at $Ra = 10^{10}$ (see § 2.3.2 and § 1.3.3).

In order to gain a quantitative understanding of the local underlying physics relevant to the SGS turbulence, the dominant flow topology associated with the positive and negative magnitudes of ν_t and κ_t has been investigated. Similarly to many other turbulent flows [22,37,38] the small scale motions in turbulent RBC have manifested the inclined "teardrop" shape of the JPDF of invariants (Q_G, R_G), through the bulk (see § 3.2.1). In condition on that "teardrop" distribution, the mean values of the eddy-viscosity and eddy-diffusivity are plotted in Figures 3.7(a) and 3.7(b), through the bulk at $Ra = 10^8$. In other words, following the most probable JPDF of Q_G and R_G invariants the average magnitudes of ν_t and κ_t, *i.e.*, $\langle \nu_t | (Q_G, R_G) \rangle$ and $\langle \kappa_t | (Q_G, R_G) \rangle$, are represented by a coloring in (Q_G, R_G) space. The plots are obtained on the base of sufficient statistical samples (> 150 per bin) in each pair of (Q_G, R_G) values. Furthermore, the invariants are normalized using $\langle Q_\Omega \rangle$ (following Ooi *et al.* [22]), and the SGS magnitudes are normalized by its maximum values (likewise Figures 3.5 and 3.6). From Figure 3.7(b), it is evident that the highest positive values of κ_t hold unstable sheet-like strain-dominated areas ($Q_G < 0$ and $R_G > 0$). This exactly matches the observation of Chumakov [39], who performed *a priori* study of the SGS flux of a passive scalar in isotropic homogeneous turbulence. He claimed that *the effective turbulent diffusion paradigm is only applicable in the strain-dominated areas*, with more frequency around the right null-discriminant line ($D_G = 27/4R_G^2 + Q_G^3 = 0$). This explains the ability of the countergradient models (such as Eq. 3.6) to provide a feasible, but crude, average approximation to the SGS scalar flux for large LES cell sizes [39] (note the enhanced function of LES models on the coarser grid, *i.e.* Mesh A, in § 3.2.1). The effective turbulent eddy-diffusivity allocate the viscous dissipative structures, which are presumed to be the mean sheet-like parts of the mushroom-like plumes elongated and scattered in the bulk (see Figure 3.7(c)). These sheets wrap around the tube-like vortex-stretching structures (Figure 3.7(c)) where the value of the turbulent diffusion κ_t is decreasing towards very small values in the stretching core (Figure 3.7(b)). Alternatively, the highest positive values of ν_t obey the structures of focal concentrated enstrophy ($Q_G > 0, R_G < 0$) and the concomitant strain-dominated areas ($Q_G < 0, R_G > 0$), as can be seen in Figure 3.7(a). The turbulent viscosity appears to follow the small scale prevalent dynamics with positive value domination, in harmony with the fact that the flow topology is mainly tube-like rotational in the

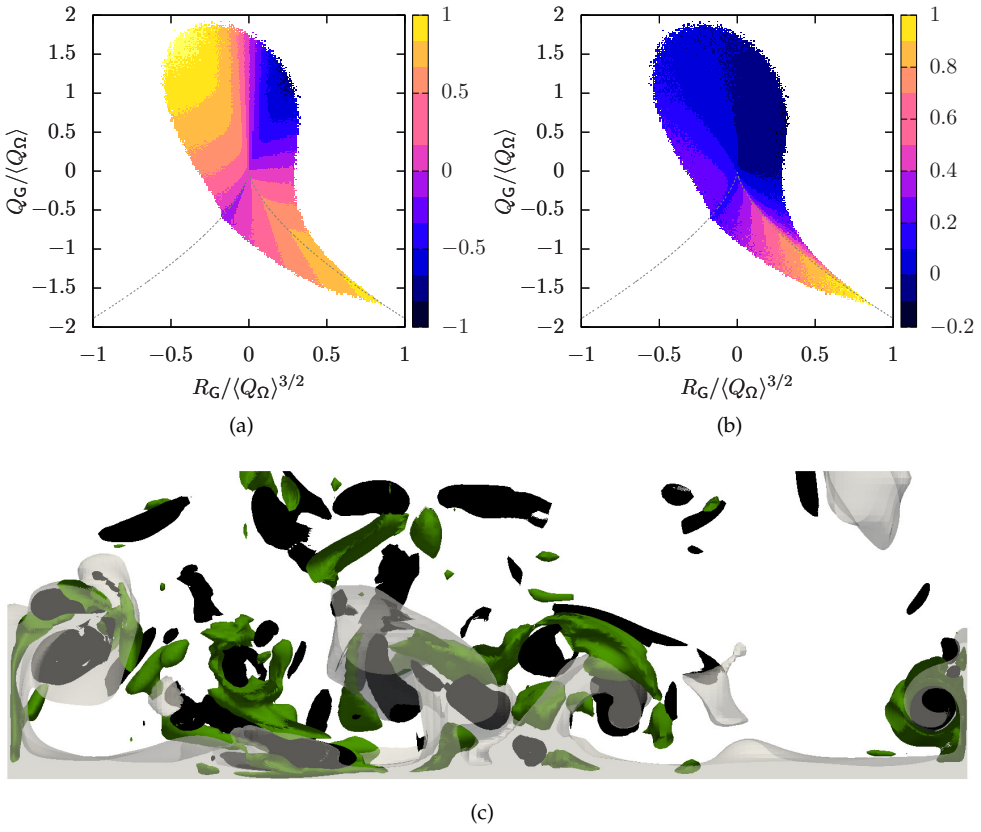

Figure 3.7: $\langle \nu_t \rangle$ (a) and $\langle \kappa_t \rangle$ (b), conditioned on (Q_G, R_G) invariants space and normalized by its maximals. The results are obtained from the case of $Ra = 10^8$ through the bulk (V_{bulk}), and the dashed tent-lines refer to the null-discriminant $D_G = 0$ in (a) and (b). (c) Displays structures of sheet-like straining (green) and tube-like vortex-stretching (black), inside and outside the hot plumes (gray volumes). The section is taken from instantaneous fields at $Ra = 10^8$.

bulk region, as revealed in § 3.2.1. Indeed, the association of negative eddy-viscosity regions with an increased anisotropy in RBC, was outlined before by Liberzon *et al.* [40]. This in turn supports our findings since the turbulence type in the core region of RBC is always comparable, in statistical aspects, with the isotropic nature § **??**. Note that both SGS features maintain negative values in the areas of focal vortex contraction $(Q_G > 0, R_G > 0)$, which play an important role in the turbulence amplification

(non-linear advection) and the kinetic cascade energy mechanism. This proposes the sustainment of the backscatter kinetic energy [41] and the countergradient buoyancy flux in the areas of compressed vortex tubes through the bulk. Finally, both ν_t and κ_t are interestingly positive and hold an identical distribution in the large-scale strain-dominated regions. This may lead us to the theory that the constant turbulent Prandt number hypothesis (linear assumptions) is only applicable in that area.

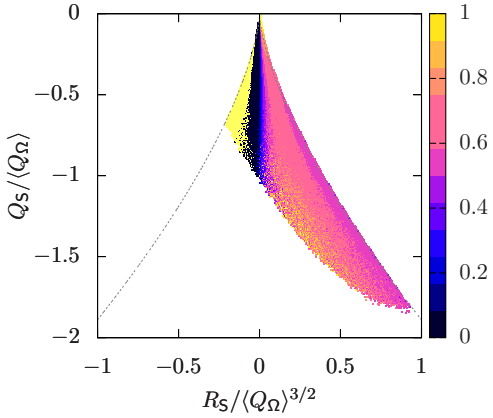

Figure 3.8: $Pr_t = \langle \nu_t \rangle / \langle \kappa_t \rangle$ conditioned on (Q_S, R_S) invariants space. The results are obtained from the case of $Ra = 10^8$ through the bulk (V_{bulk}), and the dashed tent-line refer to the null-discriminant $D_S = 0$.

One can support this from the distribution of the turbulent Prandtl number conditioned on (Q_S, R_S) space, *i.e.*, $Pr_t = \langle \nu_t | (Q_S, R_S) \rangle / \langle \kappa_t | (Q_S, R_S) \rangle$, in Figure 3.8. The allocation of the most bulk-dominated value *i.e.*, $Pr_t = 0.55$, in the strain-dominated areas, can be observed. It concentrates close to the axisymmetric expansion (right tent-line of null-discriminant straining $D_S = 27/4R_S^2 + Q_S^3 = 0$) where the local geometry of dissipation holds the sheet-like structures. Note also that $Pr_t = 0$ when $R_S = 0$, at which the flow is mostly identified as two-dimensional.

3.4 *A priori* study of the SGS heat flux models

Most of the parameterizations used in LES of RBC are based on the assumption that the SGS heat flux is aligned against the spatial gradient of the resolved temperature (Eq. 3.4). Typically these parameterizations are tested by implementing them in model runs, and comparing the outcome of the simulations *a posteriori*, with the available data. The modeled results will be of integrated nature including a limited accuracy

of the temporal and spatial numerical discretisation used. Hence, the assessment of models performance *a posteriori*, sometimes may not provide the needed insight into the physical robustness of the parameterizations. A more direct approach, *a priori* testing, can allow an excellent judgment on the validity of existing models. It can provide valuable data to test the behavior of the models and eventually can help to improve them. Such examples on testing the SGS scalar modelings can be found in studying the alignment trends of the SGS passive scalar in isotropic turbulence [39], and similarly in the atmospheric boundary layer [19]. In this context, we study the geometric alignment trends of the SGS heat flux vector $\bar{\boldsymbol{q}}$ derived from the Taylor series expansion [31] in comparison with $\bar{\boldsymbol{q}}$ parameterizations. This derivation is generic for a wide class of symmetric filters defined in real space such as the Gaussian, the tophat and (almost) all the discrete filters [42]. The spatial derivatives make the SGS flux invariant under the change of sign of large-scale components, and which in turn allows the reversibility dynamics [42]. Generally, using the first two terms of the Taylor series expansion for a Gaussian filter [42], applied to our DNS database, we obtain an accurate prediction of $\bar{\boldsymbol{q}}$, as follows

$$\bar{\boldsymbol{q}} \approx \frac{\Delta^2}{12}\mathsf{G}\nabla T + \frac{\Delta^4}{288}\begin{pmatrix}\mathsf{H}(u)\colon \mathsf{H}(T)\\ \mathsf{H}(v)\colon \mathsf{H}(T)\\ \mathsf{H}(w)\colon \mathsf{H}(T)\end{pmatrix} \qquad (\equiv \boldsymbol{q}), \tag{3.12}$$

where $\mathsf{H}(\phi) = \nabla\nabla\phi$ is the Hessian of a scalar field ϕ. Similarly, on the base of the down temperature gradient closure, the classical parameterizations for $\bar{\boldsymbol{q}}$ in LES, such as the Smagorinsky eddy-diffusivity model [43], can be approximated as

$$\bar{\boldsymbol{q}} \approx -\nu_t Pr_t^{-1}\nabla T = -(C_s\Delta)^2 Pr_t^{-1}|\mathsf{S}|\nabla T \qquad (\equiv \boldsymbol{q}^{eddy}), \tag{3.13}$$

where C_s is the model's constant, and the tensor diffusivity (or nonlinear) model [31], is approached (taking the first term of Eq. 3.12) as

$$\bar{\boldsymbol{q}} \approx \frac{\Delta^2}{12}\mathsf{G}\nabla T \qquad (\equiv \boldsymbol{q}^{nl}). \tag{3.14}$$

Both Eq. 3.13 and 3.14, are combined linearly in the so-called mixed model [19], as

$$\bar{\boldsymbol{q}} \approx \frac{\Delta^2}{12}(\mathsf{G}\nabla T - \Lambda|\mathsf{S}|\nabla T) \qquad (\equiv \boldsymbol{q}^{mix}), \tag{3.15}$$

where Λ is the ratio of corresponding model coefficients.
Similarly to the approach proposed by Higgins *et al.* [19], we construct the same space of the so-called "mixed model span" [19], defined as the plane containing the vectors $(\boldsymbol{q}^{eddy}, \boldsymbol{q}^{nl})$, and the normal to the mixed span $\boldsymbol{q}^{eddy} \times \boldsymbol{q}^{nl}$. A sketch of the geometry and definition of angles used is presented in Figure 3.9(b). In this framework, we

consider $\boldsymbol{q}$ (derived in Eq. 3.12) as the actual SGS heat flux, evaluated from the DNS database, and we study its alignments in that space. To do so, the JPDF of the angles α and β, defined together with γ, as

$$\alpha = \cos^{-1}\left[\frac{(\boldsymbol{q}^{eddy} \times \boldsymbol{q}^{nl}) \cdot \boldsymbol{q}}{|\boldsymbol{q}^{eddy} \times \boldsymbol{q}^{nl}||\boldsymbol{q}|}\right], \quad \beta = \cos^{-1}\left[\frac{\boldsymbol{q}^{eddy} \cdot \boldsymbol{q}^{p}}{|\boldsymbol{q}^{eddy}||\boldsymbol{q}^{p}|}\right], \quad \gamma = \cos^{-1}\left[\frac{\boldsymbol{q}^{eddy} \cdot \boldsymbol{q}^{nl}}{|\boldsymbol{q}^{eddy}||\boldsymbol{q}^{nl}|}\right], \tag{3.16}$$

is plotted on the unit sphere. $\boldsymbol{q}^{p}$ is the projection of the heat flux onto the plane spanned by the mixed model, *i.e.* the portion of heat flux that can be expressed by the mixed model. This JPDF quantifies the relative frequency of orientations of the SGS heat flux vector in respect to the defined coordinates. In addition, a single probability density function (PDF) of γ is shown at the bottom of each plot to characterize the alignment of the tensor diffusivity vector $\boldsymbol{q}^{nl}$ with respect to the eddy-diffusion vector $\boldsymbol{q}^{eddy}$. The lower turbulent regime at $Ra = 10^8$ within the bulk (V_{bulk}) has been considered since no significant changes are observed respect to $Ra = 10^{10}$. We firstly examine the influence of the characteristic length-scale, Δ, and the high-order spatial derivatives, *i.e.* the second term in Eq. 3.12, in Figure 3.9. Two different length-scale *i.e.* $\Delta = 2\eta_{DNS}$ and $8\eta_{DNS}$, are chosen where η_{DNS} is the maximum DNS grid size defined in Table 3.1. One can clearly note the influence of Δ in reducing the effect of the Hessian multiplication (Figures 3.9(a) and 3.9(c)). From Figure 3.9(d), the high-order derivatives tend to diffuse the direction of the SGS heat flux towards the normal to the span mixed model, but with a maintenance of maximal alignment within that span. This coincides to some extent with the findings of Higgins *et al.* [19] that reported the validity of the mixed-model span in describing the most likely orientations of the measured SGS heat flux in the lower atmosphere. Similarly here, the SGS heat flux points its nonlinear approach (Eq. 3.14) with shifted preferential orientations towards the equatorial plane defined as a linear combination of $\boldsymbol{q}^{nl}$ and $\boldsymbol{q}^{eddy}$ (Figure 3.9(c)). Note that the JPDF is symmetric about the equator and just the front part of the unit sphere which contains the peak of the PDF is shown. On the other hand, our results are also in perfect harmony with the alignment outcomes of the SGS passive scalar in isotropic homogeneous turbulence [39]. Therein, the SGS flux is approached following Eq. 3.14 in *a priori* analysis, and found to be misaligned with the vector of the resolved gradient (Eq. 3.13), similarly shown at the bottom of each plot in Figure 3.9. In conclusion, one can corroborate the failure of the isotropic eddy-diffusivity parameterization ($\boldsymbol{q}^{eddy}$) in turbulent RBC. It can be argued that the rotational geometries Q_Ω are prevalent in the bulk over the strain slots and $\Omega = \mathsf{G} - \mathsf{S}$ is an antisymmetric tensor that thus rotates the thermal gradient vector to be almost perpendicular to $\boldsymbol{q}^{nl}$ (note also that κ_t is almost zero in regions of focal concentrated enstrophy as shown in § 3.3). Apart from that, the physical nature of the problem imposes a streamwise component of buoyant production as a SGS heat flux which is separated and should not be vanished by the (mean) large-scale thermal gradient

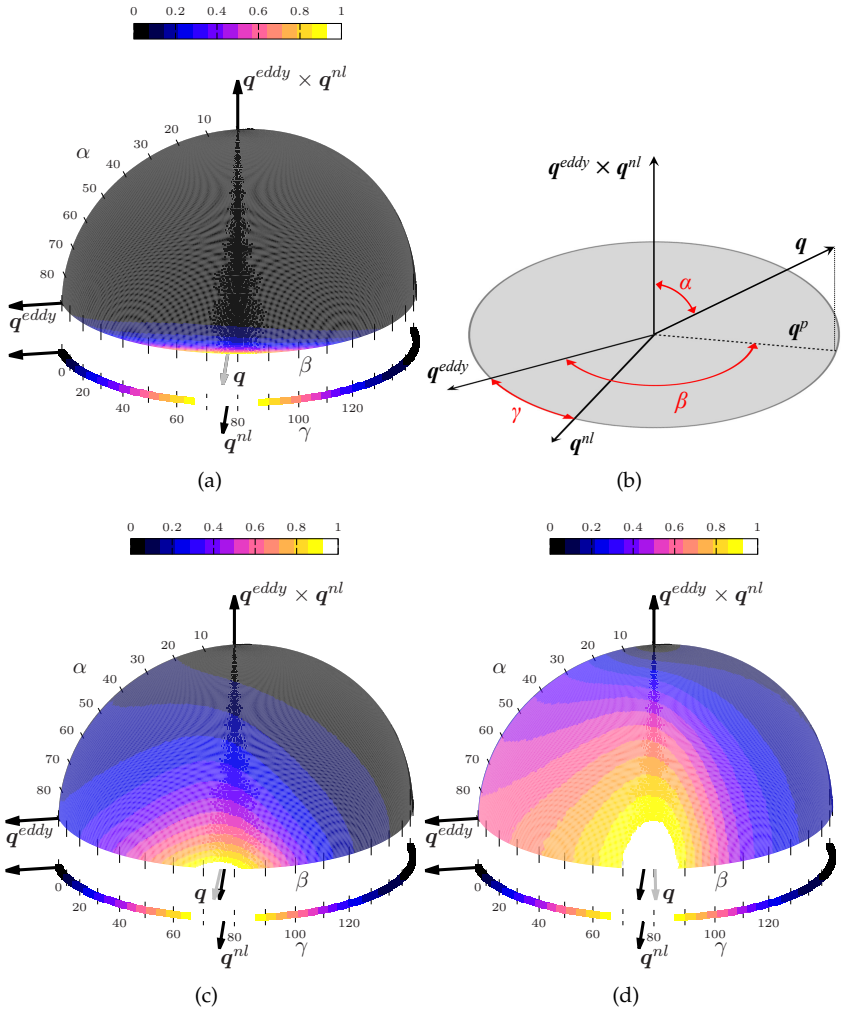

Figure 3.9: JPDF of the angles (α, β) defined in Eqs. 3.16, and plotted on a half of unit sphere to exhibit the orientation trends of $\boldsymbol{q}$ in the space of the mixed model. (a) Shows the alignment trends when the length-scale $\Delta = 2\eta_{DNS}$, (c) represents the case of $\Delta = 8\eta_{DNS}$ and (d) displays the case of $\{\mathsf{H}(u)\colon \mathsf{H}(T), \mathsf{H}(v)\colon \mathsf{H}(T), \mathsf{H}(w)\colon \mathsf{H}(T)\}$. The PDF of γ is shown along the bottom strip of each chart. A sketch of definitions the angles used in the data analysis is presented in (b). For comparative and simplicity reasons the JPDF and PDF magnitude are normalized by its maximals.

components in the bulk [2].

In the same unified framework, we consider the constitutive relation of Daly and Harlow [18] based on the averaged Reynolds stresses in modeling the SGS heat flux within RANS method, and which has been justified as a reasonable assumption for locally-averaged flows in Chumakov [39]. Namely, by employing the same approximation as in § 3.3 for the filtered-scale stress, *i.e.* $\bar{\tau} \approx (\Delta^2/12)\mathsf{G}\mathsf{G}^t$, Daly and Harlow model [18] is approached in *a priori* test, as

$$\bar{\boldsymbol{q}} \approx -\mathcal{T}_{SGS}\bar{\tau}\nabla T = -\frac{\Delta^2}{12}|\mathsf{S}|^{-1}\mathsf{G}\mathsf{G}^t\nabla T \qquad (\equiv \boldsymbol{q}^{DH}), \tag{3.17}$$

where $\mathcal{T}_{SGS} = 1/|\mathsf{S}|$ is an appropriate SGS timescale [39]. Moreover, the model proposed by Peng and Davidson [14] that also invokes a tensorial eddy-diffusivity as in [18]. Instead, $\bar{\tau}$ is estimated by the eddy-viscosity model, *i.e.*, $\bar{\tau} \approx -2\nu_t\mathsf{S}$, and $\mathcal{T}_{SGS} \propto \Delta^2/\nu_t$, yielding to

$$\bar{\boldsymbol{q}} \approx C_t\Delta^2\mathsf{S}\nabla T \qquad (\equiv \boldsymbol{q}^{PD}), \tag{3.18}$$

where C_t is a model coefficient. The ability of the last two parameterizations is investigated in the same mixed model coordinates. Namely, we replace $\boldsymbol{q}$ in Figure 3.9 by its estimated vectors and observe the dominant orientations resulted by the models in relevant to the mixed model space. As shown in Figure 3.10, it seems that both parameterizations are preferentially pointing in the span of the mixed model, similar to the actual SGS heat flux $\boldsymbol{q}$. This confirms the fairly good validity of the mixed model in turbulent RBC. It is interesting to note that the assumption of Daly and Harlow ,$\boldsymbol{q}^{DH}$, gives better prediction and closely approaches the direction of $\boldsymbol{q}^{nl}$. In contrast, the straining diffusivity assumption of Peng and Davidson model, $\boldsymbol{q}^{PD}$, points towards the direction of the linear model, $\boldsymbol{q}^{eddy}$, and thus it can be worse/less applicable in RBC. This is not so strange and supports the collaborating sustain of the streamwise SGS heat flux with the thermal gradient in the presence of dominant shear stress. In order to give a clear explanation, the alignment of the thermal gradient vector is studied in the space of rate-of-strain eigenframe, in Figure 3.11(a). The three orthogonal eigendirections ($\boldsymbol{s}_1$, $\boldsymbol{s}_2$, $\boldsymbol{s}_3$) therein, represent the eigenvectors of S, in correspondence to the three eigenvalues $(\lambda_1^{\mathsf{S}}, \lambda_2^{\mathsf{S}}, \lambda_3^{\mathsf{S}})$. Since the velocity field is divergence-free, $\lambda_1^{\mathsf{S}} + \lambda_2^{\mathsf{S}} + \lambda_3^{\mathsf{S}} = 0$, and the eigensystem can be ordered $\lambda_1^{\mathsf{S}} \geqslant \lambda_2^{\mathsf{S}} \geqslant \lambda_3^{\mathsf{S}}$ with $\lambda_1^{\mathsf{S}} \geqslant 0$ (extensive eigendirection) and $\lambda_3^{\mathsf{S}} \leqslant 0$ (compressive eigendirection), and λ_2^{S} is either positive or negative. It can be seen from Figure 3.11(a), that the ∇T vector aligns very well with the most contracting (negative) eigendirection of the resolved strain, *i.e.* $\boldsymbol{s}_3$, in consistency with the findings in [19, 39]. $\boldsymbol{q}^{DH}$ gives somewhat an "ideal" model [39] that accurately predicts the SGS heat flux direction in turbulent

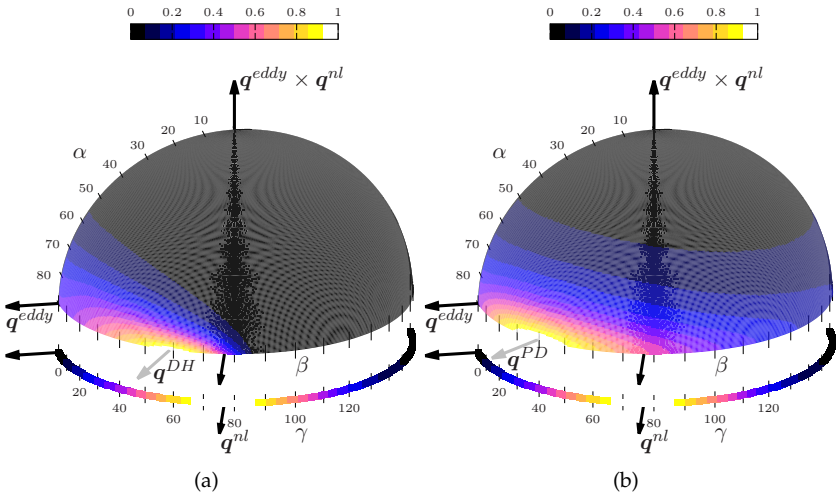

Figure 3.10: The same JPDF charts represented in Figure 3.9, however q is replaced by (a) Daly and Harlow relation [18] (q^{DH}) and (b) Peng and Davidson model [14] (q^{PD}).

RBC (Figure 3.10(a)), similarly shown for passive scalar of isotropic turbulence [39]. *This model gives good prediction in the inertial range of LES filters, both in terms of direction and magnitude of the SGS flux vector. The time scale that adjusts the correct flux magnitude is based on the resolved strain. The model has an advantage of not requiring any additional transport equations or additional filtering, it does not have any user-adjustable constant* [39]. In an identical manner to the passive scalar, Figure 3.11(b) displays the preferential coincidence of q^{nl} direction with the direction of the most extensive eigenvector $\tau_1^{\mathsf{GG}^t}$ of the SGS stress approached as, $\bar{\tau} \approx (\Delta^2/12)\mathsf{GG}^t$ (corresponds to the highest eigenvalue $\lambda_1^{\mathsf{GG}^t}$). This argues the essential connection between the SGS heat flux and $\bar{\tau}$ in RBC, and the very well accurate prediction of $\bar{\tau}$ using the GG^t tensor. Note that the first invariant of GG^t tensor, *i.e.* $P_{\mathsf{GG}^t} = 2(Q_\Omega - Q_\mathsf{S})$, identifies directly the dominant rotational focal enstrophy over the dissipation in the bulk. Moreover, its second invariant $Q_{\mathsf{GG}^t} = \mathsf{V}^2 + Q_\mathsf{G}^2$ also bears the L^2-norm of the vortex-stretching vector and the dominant focal tube-like structures in the bulk, in RBC. In consequence, the assumption of q^{DH} is highly sensitive to the subtle dominant topology, including the rotation by buoyant production, which becomes tightly interacted with the viscous straining. In conclusion, the tensor-diffusivity approach (derived from the tensor-viscosity) is a crucial choice in the parameterization of the SGS heat flux in turbulent RBC, and the quality of modeling the SGS stress $\bar{\tau}$ becomes the primary concern.

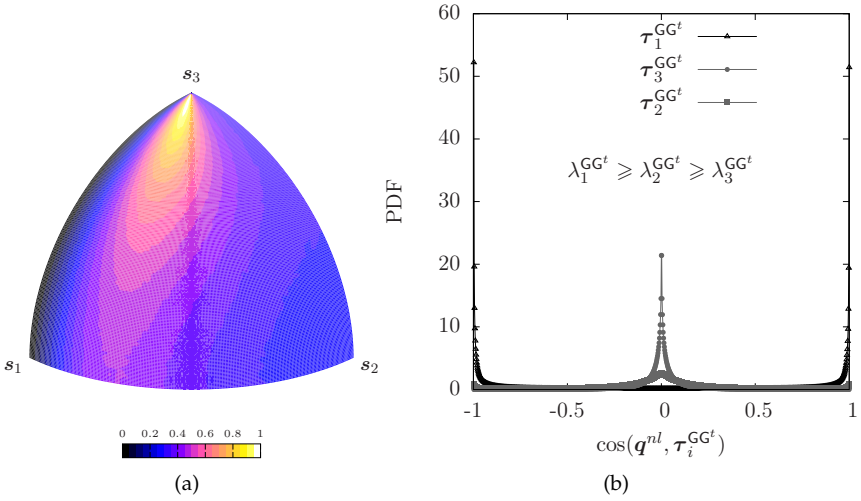

Figure 3.11: (a) Alignment trends of the temperature gradient vector ,∇T, in the rate-of-strain eigenframe. (b) Displays the PDF of the cosine of the angles between the SGS heat flux approached from the nonlinear model $\boldsymbol{q}^{nl}$ and the three eigenvectors $\boldsymbol{\tau}_i^{\mathsf{GG}^t}$ of the SGS stress $\bar{\tau} \approx (\Delta^2/12)\mathsf{GG}^t$.

Another candidate for the SGS heat flux parameterization can be sought in the light of the small-scale dynamics in turbulent RBC, studied in § 2.3. Therein, a novel second-order tensor, $\mathsf{G}_\theta = \nabla(\boldsymbol{u}T)$ defined as the velocity-times-temperature gradient tensor, was proposed. It directly discloses the small-scale kinetic-thermal interactions and buoyant production of thermal plumes. It was also shown the relative ability of $|\mathsf{G}_\theta|$ in identifying the intensive dissipation of heat flux which deeply characterizes the action of thermal plumes. On the base of that outcome, we can consider the second-order tensor $\bar{\mathsf{G}}_\theta\bar{\mathsf{G}}_\theta^t$ (or its invariants and eigenvectors) as a possible candidate in approaching the tensorial turbulent-diffusion in RBC. Firstly, it is useful to derive the formulation of this tensor as a combination of various essential tensors, as

$$\bar{\mathsf{G}}_\theta\bar{\mathsf{G}}_\theta^t = \bar{T}^2\bar{\mathsf{G}}\bar{\mathsf{G}}^t + \bar{\mathsf{G}}\nabla\bar{T}\otimes\bar{\boldsymbol{u}}\bar{T} + \bar{\boldsymbol{u}}\bar{T}\otimes\bar{\mathsf{G}}\nabla\bar{T} + \bar{\boldsymbol{u}}\otimes\bar{\boldsymbol{u}}|\nabla\bar{T}|^2. \tag{3.19}$$

Upon this formulation, one can outline a set of important properties pertaining to $\bar{\mathsf{G}}_\theta\bar{\mathsf{G}}_\theta^t$, as following: [**P1**] It depends on the resolved fields that provide the condition of locality. [**P2**] Its trace contributes directly to the evolution of thermal plumes and buoyant production since $tr(\bar{\mathsf{G}}_\theta\bar{\mathsf{G}}_\theta^t) = \bar{\mathsf{G}}_\theta : \bar{\mathsf{G}}_\theta = |\bar{\mathsf{G}}_\theta|^2$, *i.e.* the L^2-norm of $\bar{\mathsf{G}}_\theta$ § 2.3. [**P3**] It is a symmetric positive-definite second-order tensor with real positive eigenvalues

and invariants. From a numerical point-of-view, this can support to some extent the desirable guarantee of stability. [**P4**] It includes terms of accurate approximations (leading terms of Taylor series expansion) to the filtered-scale stress, $\bar{\mathsf{G}}\bar{\mathsf{G}}^t$, the SGS heat flux ,$\bar{\mathsf{G}}\nabla\bar{T}$, and the SGS temperature variance, $|\nabla\bar{T}|^2$, embedding a combination of chief terms, which compose into the implicit algebraic formulation of the SGS heat flux [14]. This formulation is derived from the transport equation of $\bar{\boldsymbol{q}}$ by considering the production term as an actual representative term to the SGS heat flux dissipation, and thus $\bar{\boldsymbol{q}}$ is assumed to be proportionally invoked to that term. [**P5**] The components of $\bar{\mathsf{G}}_\theta\bar{\mathsf{G}}_\theta^t$ impose paramount interactions between the subgrid and supergrid (large-scale) features, such as the turbulent heat flux ,$\bar{\mathsf{G}}\nabla\bar{T}$, with the local large-scale heat transport ,$\bar{\boldsymbol{u}}\bar{T}$, that in turn are not trivial in RBC. Indeed, many studies such as Togni *et al.* [3], have displayed the inherent multi-scale mechanical energy and temperature variance budgets that occur in RBC. They gave a compound description on the inter-scale energy transfer of production/dissipation, by means of the mechanisms of buoyancy, pressure and inertial transport, between the bulk and the near-wall regions.

In order to test the validity of $\bar{\mathsf{G}}_\theta\bar{\mathsf{G}}_\theta^t$ tensor, let us investigate the alignment trends in relevant to the mixed model coordinates, just identically to the other models. To do so, we propose a possible parameterization of the SGS heat flux, given as follows

$$\bar{\boldsymbol{q}} \approx -\Delta^2|\nabla T|^{-2}|\mathsf{S}|^{-1}\mathsf{G}_\theta\mathsf{G}_\theta^t\nabla T \qquad (\equiv \boldsymbol{q}^{\mathsf{G}_\theta\mathsf{G}_\theta^t}), \tag{3.20}$$

and plot its properties, similarly done in Figures 3.10(a) and 3.11(b). The new parameterization ,$\boldsymbol{q}^{\mathsf{G}_\theta\mathsf{G}_\theta^t}$, seems to roughly follow the behavior of $\boldsymbol{q}^{DH}$ (Figure 3.10(a)). As can be seen in Figure 3.12(b), the model preferentially points towards $\boldsymbol{q}^{nl}$, identically to $\boldsymbol{q}^{DH}$; however, it additionally implicates higher diffusive orientation perpendicular to the span mixed model, just similar to the effect of the higher-order Hessian term in $\boldsymbol{q}$ (Figure 3.9(d)). This may be a result of the misalignment between ∇T and $\mathsf{G}\nabla T$ persistent in RBC, under the interactions between the large and small scales of motions. Meaning that, the multiplications of the two terms, $\mathsf{G}\nabla T \otimes \boldsymbol{u}T$ and $\boldsymbol{u}T \otimes \mathsf{G}\nabla T$ (in $\mathsf{G}_\theta\mathsf{G}_\theta^t$ formulation) by ∇T, as a part of the new model, $\boldsymbol{q}^{\mathsf{G}_\theta\mathsf{G}_\theta^t}$ formulation, can play a major role in diverging the model's orientation from $\mathsf{G}\nabla T$ direction (misaligned with the thermal gradient). Therefore, the tensor $\mathsf{G}_\theta\mathsf{G}_\theta^t$ standalone may give better effectiveness using its invariants and eigenvectors. Figure 3.12(a) shows the very good alignment between $\boldsymbol{q}^{nl}$ and the highest positive (most extensive) eigenvector $\boldsymbol{\tau}_1^{\mathsf{G}_\theta\mathsf{G}_\theta^t}$. This manifests the good prediction of the buoyant production direction using a positive amplification of $|\mathsf{G}_\theta|$, *i.e.*, the highest eigenvalue $\lambda_1^{\mathsf{G}_\theta\mathsf{G}_\theta^t}$. At the end, one can suggest in fairly good argument that the tensor $\bar{\mathsf{G}}_\theta\bar{\mathsf{G}}_\theta^t$, which takes into account various essential terms, including $\bar{\mathsf{G}}\bar{\mathsf{G}}^t$ (contribution to Daly and Harlow assumption), to be the key ingredient of modeling the SGS thermal turbulence in RBC.

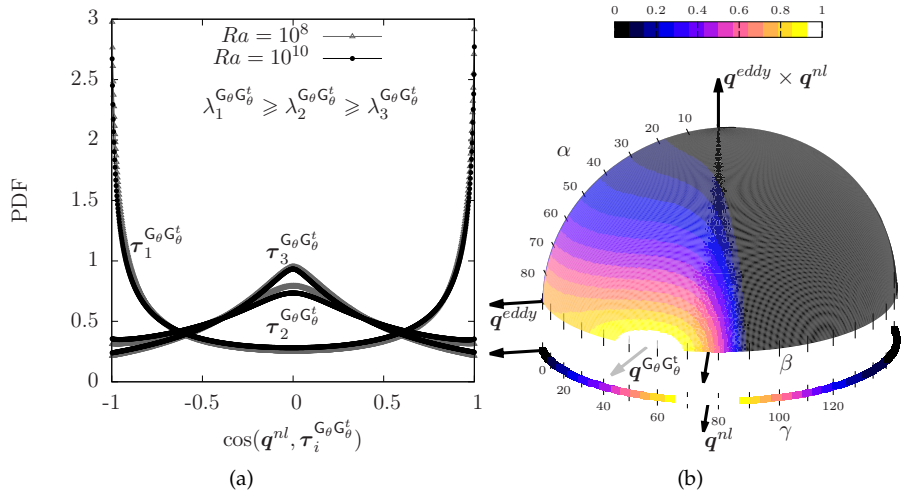

Figure 3.12: (a) Displays the PDF of the cosine of the angles between the SGS heat flux approached from the nonlinear model q^{nl} and the three eigenvectors $\tau_i^{G_\theta G_\theta^t}$ of $G_\theta G_\theta^t$ tensor, and (b) is the JPDF representation identical to Figure 3.10 with the parameterization $q^{G_\theta G_\theta^t}$, instead.

3.5 Conclusions

Using the DNS database in chapter 1, *a priori* study of the underlying topological properties of the SGS features and alignment trends of existing turbulent heat flux parameterizations in LES, have been performed for turbulent Rayleigh-Bénard convection (RBC). Two Rayleigh numbers have been studied, $Ra = \{10^8, 10^{10}\}$, however regarding to the similarity, the low turbulent regime has been the most considered case. Generally, the main conclusions are threefold.

Firstly, a limitation in using LES eddy-viscosity models, such as WALE, QR and the recent S3QR [17] is found in turbulent RBC. It is based on *a posteriori* assessment and topological analysis of the models performance applying the assumption of constant turbulent Prandtl number $Pr_t = 0.4$. The ν_t-models have shown a fairly well prediction of turbulent kinetics on coarse grids. They retrieve the effect of the unfiltered scales to relax the spatial resolution in the dominant structures of vortex-stretching and viscous dissipation. Particularly, they smooth well the coarse-grained viscous dissipation associated with the energy transfer which occurs on the large negative contracting deformation in the inertial subrange. However, these models fail

in capturing the subtle coupling between buoyant production and viscous straining. They restrain the production of further enstrophy pertained to the buoyancy and thermal plumes in the bulk and hence they overestimate the SGS heat flux and the overall Nu. The topological analysis, on the other hand, has corroborated the consistency of the bulk topologies in RBC with an isotropic turbulence [22].

Secondly, *a priori* investigations on the underlying physics of the SGS key ingredients *i.e.* ν_t, κ_t and Pr_t have revealed that the mean values of ν_t and κ_t are intrinsically positive in turbulent RBC at the current configurations. Upon that, it is claimed that the turbulent wind is mostly driven by the mean buoyant forces at the sidewalls (hot ascending and cold descending streams) and not by the turbulent fluctuations (Reynolds stress and negative turbulent energy production). The obtained turbulent Prandtl number, $\langle Pr_t \rangle = \langle \nu_t \rangle / \langle \kappa_t \rangle$ has displayed a nearly constant value of 0.55 across the bulk, independently of the Ra magnitude. The highest positive values of turbulent diffusion are found to hold the sheet-like strain-dominated areas. They contribute to the mean expanded parts of the thermal plumes in the bulk wrapped around the vortex tubes. Instead, the highest positive values of ν_t obey the focal concentrated enstrophy in accompaniment to the strain-dominated regions. They follow in this positiveness the behavior of the small-scale dynamics and the domination of the tube-like rotation in the bulk, similarly to an isotropic turbulence. Both SGS features are found to maintain negative values corresponding to the energy backscatter ($\nu_t < 0$) and countergradient heat transport ($\kappa_t < 0$) in the compressed vortical structures through the bulk. Upon these observations, it has been suggested that the effective turbulent diffusion paradigm and eddy-viscosity approach (linear assumption of constant Pr_t) are only applicable in the strain-dominated areas in turbulent RBC.

Thirdly, *a priori* testing on the validity of existing SGS heat flux models has been performed newly in RBC. The study has involved the investigation on the geometric alignment trends of the most likely relative orientation imposed by the models. Firstly, it is found that the actual SGS heat flux (derived using the first two terms of the Taylor series expansion) points inside the span of the mixed model. That span is defined as the plane containing linear combination of the tensor-diffusivity vector, $\boldsymbol{q}^{nl}$ (Eq. 3.14), and the eddy-diffusion vector, $\boldsymbol{q}^{eddy}$ (Eq. 3.13). This in turn has certified the validity of the mixed model in RBC, similarly as in the atmospheric boundary layer [19]. The nonlinear tensor-diffusivity model, $\boldsymbol{q}^{nl}$, is very likely to be misaligned with the thermal gradient, $\boldsymbol{q}^{eddy}$. It has been argued that the rotational geometries Q_Ω are prevalent in the bulk over the strain slots, and the rate-of-rotation tensor Ω is a skew-symmetric tensor that rotates the thermal gradient vector to be always normal to $\boldsymbol{q}^{nl}$. This has eventually led to that the parameterizations linearly aligned against the spatial thermal gradient, $\boldsymbol{q}^{eddy}$, are invalid in RBC. Instead, the

tensorial eddy-diffusivity approach is a crucial choice in modeling the SGS heat flux. In this framework, the most used models of Daly and Harlow [18] parameterization, $\boldsymbol{q}^{DH}$ (Eq. 3.17), and the straining diffusivity Peng and Davidson [14], $\boldsymbol{q}^{PD}$ (Eq. 3.18), parameterization, have been tested *a priori*. Both models are found to be preferentially pointed in its orientation inside the span mixed model. The thermal gradient vector tends to align fairly well with the contracting eigendirection of the rate-of-strain tensor and hence the parameterization $\boldsymbol{q}^{PD}$ is shown to be less applicable in RBC. In contrast, the $\boldsymbol{q}^{DH}$ closely approaches the direction of $\boldsymbol{q}^{nl}$ in the mixed model coordinates and the SGS heat flux is found to coincide preferentially the direction of the most extensive eigenvector of $\mathsf{G}\mathsf{G}^t$ tensor.

Finally, a new approach of using $\bar{\mathsf{G}}_\theta \bar{\mathsf{G}}_\theta^t$ tensor in modeling the SGS thermal turbulence in RBC, has been suggested. It contains a combination of chief components, including the $\bar{\mathsf{G}}\bar{\mathsf{G}}^t$ tensor, owning properties similar to the implicit algebraic formulation of the SGS heat flux. Following *a priori* examination of one candidate $\bar{\boldsymbol{q}} \approx -\Delta^2 |\nabla T|^{-2} |\mathsf{S}|^{-1} \mathsf{G}_\theta \mathsf{G}_\theta^t \nabla T$, it is found that the new model performs almost similar to $\boldsymbol{q}^{DH}$, that in turn encourages its application.

References

[1] E. D. Sigga. High Rayleigh number convection. *Annual Reviews of Fluid Mechanics*, 26:137, 1994.

[2] K. Hanjalić. One-point closure models for buoyancy-driven turbulent flows. *Annual Reviews of Fluid Mechanics*, 34:321–347, 2002.

[3] R. Togni, A. Cimarelli, and E. D Angelis. Physical and scale-by-scale analysis of Rayleigh-Bénard convection. *Journal of Fluid Mechanics*, 782:380–404, 2015.

[4] F. Chillà and J. Schumacher. New perspectives in turbulent Rayleigh-Bénard convection. *The European Physics Journal E*, 35:58, 2012.

[5] F. Dabbagh, F. X. Trias, A. Gorobets, and A. Oliva. On the evolution of flow topology in turbulent Rayleigh-Bénard convection. *Physics of Fluids*, 28:115105, 2016.

[6] R. J. A. M. Stevens, D. Lohse, and R. Verzicco. Prandtl and Rayleigh number dependence of heat transport in high Rayleigh number thermal convection. *Journal of Fluid Mechanics*, 688:31–43, 2011.

[7] E. P. van der Poel, R. Verzicco, S. Grossmann, and D. Lohse. Plume emission statistics in turbulent rayleigh- bénard convection. *Journal of fluid mechanics*, 772:5–15, 2015.

[8] T. M. Eidson. Numerical simulation of the turbulent Rayleigh-Bénard problem using subgrid modelling. *Journal of Fluid Mechanics*, 158:245–268, 1985.

[9] S. Peng and L. Davidson. Comparison of subgrid-scale models in LES for turbulent convection flow with heat transfer. *In 2nd EF Conference in Turbulent Heat Transfer*, pages 5.24–5.35, 1998.

[10] M. Germano, U. Piomelli, P. Moin, and W. H. Cabot. A dynamic subgrid-scale eddy viscosity model. *Physics of Fluids A*, 3:1760–1765, 1991.

[11] D. K. Lilly. A proposed modification of the Germano subgrid-scale closure method. *Physics of Fluids A*, 4:633–635, 1992.

[12] S. H. Peng, K. Hanjalic, and L. Davidson. Large-eddy simulation and deduced scaling analysis of Rayleigh-Bénard convection up to $Ra = 10^9$. *Journal of Turbulence*, 7:66, 2006.

[13] T. Czarnota, T. Wetzel, and C. Wagner. *Large Eddy Simulation of Turbulent Thermal Convection Using Different Subgrid-Scale Models*, pages 505–514. Springer International Publishing, Cham, 2016.

[14] S. Peng and L. Davidson. On a subgrid-scale heat flux model for large eddy simulation of turbulent thermal flow. *International Journal of Heat and Mass Transfer*, 45:1393–1405, 2002.

[15] N. Foroozani, J. J. Niemela, V. Armenio, and K. R. Sreenivasan. Influence of container shape on scaling of turbulent fluctuations in convection. *Physical Review E*, 90:063003, 2014.

[16] C. Meneveau, T. S. Lund, and W. H. Cabot. Lagrangian dyanmic subgrid-scale model of turbulence. *Journal of Fluid Mechanics*, 319:353–385, 1996.

[17] F. X. Trias, D. Folch, A. Gorobets, and A. Oliva. Building proper invariants for eddy-viscosity subgrid-scale models. *Physics of Fluids*, 27:065103, 2015.

[18] B. J. Daly and f. H. Harlow. Transport equations in turbulence. *Physics of Fluids*, 13:2634, 1970.

[19] C. W. Higgins, M. B. Parlange, and C. Meneveau. The heat flux and the temperature gradient in the lower atmosphere. *Geophysical Research Letter*, 31:L22105, 2004.

[20] F.Nicoud and F. Ducros. Subgrid-scale stress modelling based on the square of the velocity gradient tensor. *Flow, Turbulence and Combustion*, 62:183–200, 1999.

[21] R. Verstappen. When does eddy viscosity damp subfilter scales sufficiently? *Journal of Scientific Computing*, 49:94–110, 2011.

[22] A. Ooi, J. Martin, J. Soria, and M. S. Chong. A study of the evolution and characteristics of the invariants of the velocity-gradient tensor in isotropic turbulence. *Journal of Fluid Mechanics*, 381:141, 1999.

[23] M. Chertkov, A. Pumir, and B. I. Shraiman. Lagrangian tetrad dynamics and the phenomenology of turbulence. *Physics of Fluids*, 11(8):2394–2410, 1999.

[24] J. Jiménez, A. A. Wray, P. G. Saffman, and R. S. Rogallo. The structure of intense vorticity in isotropic turbulence. *Journal of Fluid Mechanics*, 255:65–90, 1993.

[25] S. W. Churchill. A Reinterpretation of the Turbulent Prandtl Number. *Industrial & Engineering Chemistry Research*, 41:6393–6401, 2002.

[26] J. Kim and P. Moin. Transport of passive scalars in a turbulent channel flow. *In Turbulent Shear Flows 6*, pages 85–96, 1987.

[27] J. Pallares and L. Davidson. Large-eddy simulations of turbulent heat transfer in stationary and rotating square ducts. *Physics of Fluids*, 14:2804, 2002.

[28] P. Sagaut. *Large Eddy Simulation for Incompressible Flows: An Introduction*. Springer, 2006.

[29] P. Moin, K. Squires, W. Cabot, and S. Lee. A dynamic subgridscale model for compressible turbulence and scalar transport. *Physics of Fluids A: Fluid Dynamics*, 3:2746–2757, 1991.

[30] I. Otic. One equation subgrid model for liquid metal forced convection. *The 8th International Topical Meeting on Nuclear Reactor Thermal Hydraulics, Operation and Safety (NUTHOS-8)*, October 2010.

[31] A. Leonard. Large-eddy simulation of chaotic convection and beyond. *35th Aerospace Sciences Meeting and Exhibit, AIAA paper*, 1997:0204, 1997.

[32] G. L. Eyink. Multi-scale gradient expansion of the turbulent stress tensor. *Journal of Fluid Mechanics*, 549:159, 2006.

[33] S. J. Kimmel and J. A. Domaradzki. Large eddy simulations of Rayleigh-Bénard convection using subgrid scale estimation model. *Physics of Fluids*, 12:169–184, 2000.

[34] U. Burr, W. Kinzelbach, and A. Tsinober. Is the turbulent wind in convective flows driven by fluctuations? *Physics of Fluids*, 15:2313, 2003.

[35] Y. Huang and Q. Zhou. Counter-gradient heat transport in two-dimensional turbulent Rayleigh-Bénard convection. *Journal of Fluid Mechanics*, 737, 2013.

[36] R. Krishnamurti and L. N. Howard. Large-scale flow generation in turbulent convection. *Proceedings of the National Academy of Sciences of the USA*, 78:1981–1985, 1981.

[37] C. B. da Silva and J. C. F. Pereira. Invariants of the velocity-gradient, rate-of-strain, and rate-of-rotation tensors across the turbulent/nonturbulent interface in jets. *Physics of Fluids*, 20(5):055101, 2008.

[38] H. M. Blackburn, N. N. Mansour, and B. J. Cantwell. Topology of fine-scale motions in turbulent channel flow. *Journal of Fluid Mechanics*, 310:269–292, 1996.

[39] S. G. Chumakov. A *priori* study of subgrid-scale flux of a passive scalar in isotropic homogeneous turbulence. *Physical Review E*, 78:036313, 2008.

[40] A. Liberzon, B. Lüthi, M. Guala, W. Kinzelbach, and A. Tsinober. *On Anisotropy of Turbulent Flows in Regions of "Negative Eddy Viscosity"*, pages 85–88. Springer Berlin Heidelberg, Berlin, Heidelberg, 2007.

[41] K. Horiuti. Coherent Structure and Subgrid-Scale Energy Transfer in Turbulence. In *IUTAM Symposium on Geometry and Statistics of Turbulence*, pages 249–254. Springer, 2001.

[42] D. Carati, G. S. Winckelmans, and H. Jeanmart. On the modelling of the subgrid-scale and filtered-scale stress tensors in large-eddy simulation. *Journal of Fluid Mechanics*, 441:119–138, 2001.

[43] J. Smagorinsky. General circulation experiments with primitive equations. *Monthly Weather Review*, 91:99–164, 1963.

4

Concluding remarks and future research

Abstract. As this thesis is composed of papers, conclusions and perspectives were given at the end of each chapter. This chapter focuses on general results, conclusions and future research.

4.1 Summary and concluding remarks

The direct numerical simulation (DNS) is the most reliable tool that allows a fully controlled picture to unravel in detail the dynamical and statistical aspects of turbulence. It can resolve many queries of turbulence physics by studying its characteristic structures, and provide indispensable data for the future progress and validation of turbulence modeling. In the light of that significance, a complete DNS study of turbulent Rayleigh-Bénard convection (RBC) in a rectangular air-filled cavity of aspect ratio $\Gamma = 1$ and π spanwise open-ended distance, was performed at $Ra = \{10^8, 10^{10}\}$. Numerically, the trustworthy DNS grids were constructed in an appropriate way, where refinements of analytical relations pertaining to the mean dissipative scales [1,2] were adopted, in correspondence to the lowest computational amount, without losing accuracy. Numerically, a conservation of the global kinetic energy was inherited within the spatial discretization using a 4^{th}-order symmetry-preserving scheme [3], and an explicit time integration scheme which guarantees linear stability, was used. The DNS dataset was processed by a statistical analysis to the underlying physics properties of turbulence, employing the tools of probability density function (PDF) and joint PDF (JPDF), in RBC. As a conclusions it was outlined,

4.1.1 Viscous and thermal dissipation rates

Thermal and kinetic energy dissipation rates expose the underlying small-scale intermittency of flow both in the bulk and the thermal BLs. They tightly couple/correlate in the vicinities next to the heating and cooling isothermal plates following the amplified thermal/kinetic turbulent fluctuations coupling at the formation patterns of sheet-like thermal plumes (Figure 1.7). In the bulk, where the mushroom-like plumes expand and dissipate transforming its portable energy into kinetic one, the two dissipations start to decorrelate to be only interacted at the plumes chunks, with the rare largest magnitudes of dissipations beyond the means (Figure 1.11).

4.1.2 The coherent large-scale circulation or the wind

The wind at the current setting is constituted into two helical rolls along the homogeneous x-direction, enfolded by the solid walls. It carries a cold falling fluid of negative heat flux at the middle of domain and rises two hot fluid of positive heat flux at the adjoining open-ended sides. The turbulent wind holds its maximum at the contracting areas near the solid walls (Figure 1.12). It is mostly driven by the mean buoyant forces at the sidewalls where groups of plumes are incorporated and combined to organize buoyancy-driven upward/hot and downward/cold mean streams, of maximum buoyant production $\langle w'T' \rangle$, at one lateral side and its opposite (Figures 1.13(a) and 3.6). By increasing the Ra, the plumes do not contribute to these

mean turbulent heat flux streams where the sidewalls-flow becomes significantly reduced (§ 2.3.2).

4.1.3 Kinetic flow topology and small-scale dynamics

Topological structures in the bulk region share several universal aspects of 3D turbulence similarly observed in a wide variety of turbulent flows. For instance, the inclined "teardrop" shape of the joint PDF statistics of invariants $(Q_{\mathsf{G}}, R_{\mathsf{G}})$ (Figure 2.2), the preferential alignment between $\boldsymbol{\omega}$ and $\boldsymbol{\lambda}_2$ the intermediate eigenstrain vector (Figure 2.5(a)), and the asymmetric $\boldsymbol{\omega}$ alignment with the vortex-stretching vector (Figure 2.5(b)). Hence, the small-scale topology in the bulk obeys stable tube-like focus/stretching and unstable sheet-like node/saddle/saddle structures, in prevalence, and the net enstrophy production is always positive. Physically, the long-lived solid-body rotation structures (vortex tubes Q_{Ω}) are dominated over the viscous dissipation $-Q_{\mathsf{S}}$, and the bulk flow is statistically compared to an isotropic turbulence [4]. The topology surrounding a fluid particle is varying upon a decaying cyclical spiralling behaviour of $(\langle DQ_{\mathsf{G}}/Dt\rangle, \langle DR_{\mathsf{G}}/Dt\rangle)$ in $(Q_{\mathsf{G}}, R_{\mathsf{G}})$ space, from unstable focus, unstable node, stable node to stable focus structures, in both turbulent cases studied (Figure 2.6). A local self-amplification of velocity derivatives (viscous straining $-Q_{\mathsf{S}}$ in the turbulent background) at $Ra = 10^{10}$, aids in contracting the vorticity worms further which assists the decaying events (interplay of the non-local pressure Hessian with the viscous diffusion and energy-injecting terms), and bends the trajectories of $(\langle DQ_{\mathsf{G}}/Dt\rangle, \langle DR_{\mathsf{G}}/Dt\rangle)$ further inwards above the null-discriminant curve $D_{\mathsf{G}} = 0$. The plumes elongate significantly before scattering in the bulk at $Ra = 10^{8}$, and participate in the large-scale kinetic energy containing eddies and turbulent wind created in the bulk. However, at $Ra = 10^{10}$, the role of the self-amplified $-Q_{\mathsf{S}}$ in creating the large-scale eddies in the bulk is enlarged. The local self-amplification of velocity derivatives $(-Q_{\mathsf{S}}/Q_{\Omega})$ at $Ra = 10^{10}$ enhances the local effects associated with (self) interactions of vorticity/strain in the strain dominated regions and thus, improve slightly the linear contributions of the vortex stretching mechanism (§ 2.2.3).

4.1.4 Thermal flow topology and small-scale dynamics

Invariants of the traceless part of velocity-times-temperature gradient tensor $(Q_{\tilde{\mathsf{G}}_\theta}, R_{\tilde{\mathsf{G}}_\theta})$ demonstrate a direct picture on the small-scale kinetic and thermal interaction dynamics and express a correct following to the evolution of thermal plumes (Figures 2.9 and 2.11). The Thermal topology is varying upon a spiralling behaviour of $(\langle DQ_{\tilde{\mathsf{G}}_\theta}/Dt\rangle, \langle DR_{\tilde{\mathsf{G}}_\theta}/Dt\rangle)$ in $(Q_{\tilde{\mathsf{G}}_\theta}, R_{\tilde{\mathsf{G}}_\theta})$ space, to a downwards trajectories $(Q_{\tilde{\mathsf{G}}_\theta} < 0)$ of sheet-like plumes evolution and an upwards spiralling of mushroom-like plumes evolution (Figure 2.12). At $Ra = 10^{8}$ the hot and cold plumes are importantly con-

tributing to the coherent large scales of heat flux, in average, which roll near the lateral sidewalls, and the trajectories spiral upwards before converging towards two skew-symmetric origins (Figure 2.12(a)). However, at $Ra = 10^{10}$, the lifetime of mushroom-like plumes is reduced under the amplified turbulent background mixing events to make the trajectories shorter-tracking converging towards a zero-valued origin (Figure 2.12(b)). Hence, the thermal plumes at this high Ra number do not contribute to the mean large scales of heat flux and just give them a life. Due to the effective mixing activities in the bulk, the heat flux is constant spatially and temporally in mean and the plumes are completely destroyed with decaying upwarded trajectories towards zero-valued origins (Figure 2.14), in both turbulent cases, and $\langle Q_{\tilde{\mathsf{G}}_\theta} \rangle = 0$, $\langle R_{\tilde{\mathsf{G}}_\theta} \rangle = 0$.

4.1.5 Limitation of use LES eddy-viscosity models

Upon *a posteriori* assessment and topological analysis of well-known LES ν_t-models such as, QR, WALE and the recent S3QR [5], with the assumption of turbulent Prandtl number $Pr_t = 0.4$, the models predict fairly well the turbulent kinetics on coarse grids. They smooth well the coarse-grained viscous dissipation occurs on the large negative contracting deformation (Figure 3.3(f)). However, they fail in capturing the subtle coupling between buoyant production and viscous straining, where they restrain the production of further enstrophy pertained to the buoyancy and thermal plumes in the bulk (Figure 3.3(i)).

4.1.6 Eddy-viscosity ν_t, eddy-diffusivity κ_t, and turbulent Prandtl number Pr_t

Eddy-viscosity ν_t and eddy-diffusivity κ_t, are intrinsically positive for the two turbulent cases and the turbulent wind is not driven by the turbulent fluctuations (Reynolds stress and negative turbulent energy production), at the current setting (see profiles in Figure 3.5). The turbulent Prandtl number, $\langle Pr_t \rangle = \langle \nu_t \rangle / \langle \kappa_t \rangle$, is nearly constant of value 0.55 across the bulk, independently of Ra. The largest positive value of κ_t hold the sheet-like strain-dominated areas in correspondence to the mean expanded parts of the thermal plumes in the bulk wrapped around the vortex tubes. Instead, the highest positive values of ν_t obey the focal concentrated enstrophy and the strain-dominated regions. Both SGS features maintain negative values corresponding to the energy backscatter ($\nu_t < 0$) and countergradient heat transport ($\kappa_t < 0$) in the compressed vortical structures through the bulk (Figure 3.7). Upon that, the effective turbulent diffusion paradigm and ν_t approach (linear assumption of constant Pr_t) is only applicable in the strain-dominated areas in turbulent RBC.

4.1.7 Validity of existing SGS heat flux parameterizations

Upon *a priori* investigation on the geometric alignment trends of the most likely relative orientation imposed by the models, the actual SGS heat flux (derived using the first two terms of the Taylor series expansion) points inside the span of the mixed model $\boldsymbol{q}^{mix}$; and the mixed model is fairly well valid in RBC (Figure 3.9). The nonlinear tensor-diffusivity model, $\boldsymbol{q}^{nl}$, is very likely to be misaligned with the thermal gradient, ∇T, because of the domination of the rotational geometries Q_Ω, in the bulk over the strain slots. Since the rate-of-rotation tensor Ω is a skew-symmetric tensor hence it rotates the thermal gradient vector to be always normal to $\boldsymbol{q}^{nl}$, and the parameterizations linearly aligned against the spatial thermal gradient, $\boldsymbol{q}^{eddy}$, are invalid in RBC. Instead, the tensorial eddy-diffusivity approach is a crucial choice in modeling the SGS heat flux. Namely, the stress diffusivity, *i.e.*, Daly and Harlow [6] model, $\boldsymbol{q}^{DH}$, and the straining diffusivity, *i.e.*, Peng and Davidson [7] parameterization, $\boldsymbol{q}^{PD}$, are preferentially pointing in its orientation inside the span mixed model (Figure 3.10). However, the thermal gradient vector tends to align fairly well with the contracting eigendirection of the rate-of-strain tensor (Figure 3.11(a)), and the parameterization $\boldsymbol{q}^{PD}$ is less applicable in RBC. In contrast, the $\boldsymbol{q}^{DH}$ closely approaches the direction of $\boldsymbol{q}^{nl}$ and the turbulent heat flux coincides preferentially the direction of the most extensive eigenvector of the subgrid-stress, $\mathsf{G}\mathsf{G}^t$ tensor (Figure 3.11(b)).

4.1.8 New tensorial approach of modeling the SGS thermal turbulence

Using $\bar{\mathsf{G}}_\theta \bar{\mathsf{G}}_\theta^t$ tensor (Eq. 3.19), a new approach of modeling the SGS heat flux in RBC, is suggested. The tensor contains a combination of chief components, including the $\bar{\mathsf{G}}\bar{\mathsf{G}}^t$ tensor and owning properties similar to the implicit algebraic formulation of the SGS heat flux (Eq. 3.19). A one candidate can be, $\bar{\boldsymbol{q}} \approx -\Delta^2 |\nabla T|^{-2} |\mathsf{S}|^{-1} \mathsf{G}_\theta \mathsf{G}_\theta^t \nabla T$, that is found to perform almost similar to $\boldsymbol{q}^{DH}$, and encourages its application.

4.2 Future research

Future works can be sought in the light of

4.2.1 *A posteriori* investigation on an appropriate use of $\bar{\mathsf{G}}_\theta \bar{\mathsf{G}}_\theta^t$ in modeling the SGS heat flux

A throughout assessment of using $\boldsymbol{q}^{\mathsf{G}_\theta \mathsf{G}_\theta^t}$, as a SGS heat flux parameterization in turbulent RBC will be of significant importance. Thereby, it can be justified to be

the key ingredient of modeling the SGS thermal turbulence widely occurred in the environment and technology. On the other hand, an optimization to the performance of $\boldsymbol{q}^{\mathsf{G}_\theta \mathsf{G}_\theta^t}$ by reducing its slight divergence orientation from $\mathsf{G}\nabla T$ direction, is of great interest in the upcoming concerns. Moreover, an alternative option of employing the $\mathsf{G}_\theta \mathsf{G}_\theta^t$ tensor standalone or its invariants and eigenvectors, in the SGS heat flux modeling for turbulent RBC, can give better candidate and open an important research trend in the future.

4.2.2 Exploring new frontiers in RBC

Many circulations in nature and industry such as, convection in the external layer of the Sun, the coherent structures in the earth 's atmosphere and oceans, mantle convection in the earth 's core, and circulations in nuclear reactors and solar thermal power plants, are ruled by very hard turbulent regime of RBC. The dynamics therein is still complex and far from reaching our knowledge in thermal turbulence. To our best knowledge, important issues of the problem have been explored by DNS in regimes $Ra > 10^{10}$. For instance, the stability of the boundary layers obeying the Prandtl-Blasius scaling at $Ra = 2 \times 10^{12}$ [8] and a recent study of the thermal plumes statistics at $Ra = 10^{12}$ [9]. However, many questions regarding the coherent dynamics therein are still open. For example, studying the flow topology and the small-scale dynamics which are crucial in constructing the turbulent wind and energy budgets, are still unsatisfied. Following the findings (§ 4.1.3), a local self-amplified straining in the bulk turbulence is developing with increasing the Ra number $(Ra = 10^{10})$. It enhances the local interactions $\boldsymbol{\omega}/\mathsf{S}$ and supports the linear vortex-stretching contributions. In this regard, the following queries can be sought: *How will the nonlinearities as the production terms of enstrophy and the strain/dissipation behave in harder turbulent regime at* $Ra = 10^{11}$*? How will the flow topology/small-scale structures change at that Ra?* Furthermore, *how will the small-scale dynamics deeply associated with the evolution of thermal plumes behave at* $Ra = 10^{11}$*, as it is differently changing with increasing the Ra (§ 4.1.4)?* All these questions are essential to disclose the small scale motions which are the key feature of turbulence physics.

To do so, we propose to extend our range of Ra of turbulent RBC by performing a fully-resolved DNS study at $Ra = 10^{11}$ and $Pr = 0.7$, in the same configurations. The mesh estimation is similarly decided as the DNS of $Ra = 10^{10}$, carried out on *MareNostrum3 supercomputing* using a mesh with $604M$ grid points. Based on this experience, the estimated grid size for $Ra = 10^{11}$ is about $5600M$ grid points $(1997 \times 1677 \times 1677)$, initialized by mesh-interpolated instantaneous fields from the DNS at $Ra = 10^{10}$, and run a period of $300[TU]$ on 8192 $CPUs$.

Apart from providing new insights of the small-scale physics, the planned DNS will be the first ever performed so far in such configurations that reduce to some extent, the impact of the confined nature in [8,9] in turbulent RBC. Moreover, it will render an indispensable data for the improvement/validation of the LES thermal turbulence modeling proposed, at $Ra = 10^{11}$. Altogether, this potential improvement in the modelization of the SGS should be a key element to explore new frontiers (in the ultimate regime) in RBC where DNSs are not possible yet.

References

[1] G. Grötzbach. Spatial resolution requirements for direct numerical simulation of the Rayleigh-Bénard convection. *Journal of Computational Physics*, 49:241–264, 1983.

[2] O. Shishkina, R. J. A. M. Stevens, S. Grossmann, and D. Lohse. Boundary layer structure in structure in turbulent thermal convection and consequences for the required numerical resolution. *New Journal of Physics*, 12:075022, 2010.

[3] R. W. C. P. Verstappen and A. E. P. Veldman. Symmetry-preserving discretization of turbulent flow. *Journal of Computational Physics*, 187:343–368, 2003.

[4] A. Ooi, J. Martin, J. Soria, and M. S. Chong. A study of the evolution and characteristics of the invariants of the velocity-gradient tensor in isotropic turbulence. *Journal of Fluid Mechanics*, 381:141, 1999.

[5] F. X. Trias, D. Folch, A. Gorobets, and A. Oliva. Building proper invariants for eddy-viscosity subgrid-scale models. *Physics of Fluids*, 27:065103, 2015.

[6] B. J. Daly and f. H. Harlow. Transport equations in turbulence. *Physics of Fluids*, 13:2634, 1970.

[7] S. Peng and L. Davidson. On a subgrid-scale heat flux model for large eddy simulation of turbulent thermal flow. *International Journal of Heat and Mass Transfer*, 45:1393–1405, 2002.

[8] R. J. A. M. Stevens, D. Lohse, and R. Verzicco. Prandtl and Rayleigh number dependence of heat transport in high Rayleigh number thermal convection. *Journal of Fluid Mechanics*, 688:31–43, 2011.

[9] E. P. van der Poel, R. Verzicco, S. Grossmann, and D. Lohse. Plume emission statistics in turbulent rayleigh- bénard convection. *Journal of fluid mechanics*, 772:5–15, 2015.

Appendix A

List of Publications

Journal Papers:

- F. Dabbagh, F. X. Trias A. Gorobets and A. Oliva, *A priori* study of subgrid-scale features in turbulent Rayleigh-Bénard convection , *Physics of Fluids*, 2017 (submitted).
- F. Dabbagh, F. X. Trias A. Gorobets and A. Oliva, On the evolution of flow topology in turbulent Rayleigh-Bénard convection , *Physics of Fluids*, **28**, 115105, 2016.

International Conference Papers:

- F. Dabbagh, F. X. Trias A. Gorobets and A. Oliva, New subgrid-scale models for large-eddy simulation of Rayleigh-Bénard convection, *Journal of Physics: Conference Series*, **745**, 032041, 2016.
- F. Dabbagh, F. X. Trias A. Gorobets and A. Oliva, Fine-scale dynamics in turbulent Rayleigh-Bénard convection, *THMT-15. Proceedings of the* 8^{th} *International Symposium On Turbulence, Heat and Mass Transfer*, September, 2015.
- F. Dabbagh, F. X. Trias A. Gorobets and A. Oliva, Spectrally-consistent regularization of turbulent Rayleigh-Bénard convection, 6^{th} *European Conference on Computational Fluid Dynamics*, 7144-7155, 2014.